

MEDAL: Manifold Embedding Distillation via Autoencoder Learning

Irene Chang¹, Tarek M. Zikry², and Genevera I. Allen^{1,3,4,†}

¹Department of Statistics, Columbia University, New York, NY 10027

²School of Data and Information Sciences, University of North Carolina at Chapel Hill, Chapel Hill, NC 27599

³Irving Institute for Cancer Dynamics, Columbia University, New York, NY 10027

⁴Center for Theoretical Neuroscience, Zuckerman Mind Brain Behavior Institute, Columbia University, New York, NY 10027

Abstract

Low-dimensional embeddings are widely used as visual summaries of high-dimensional data and to enable downstream scientific discoveries. Yet, popular nonlinear dimension reduction methods, such as t-SNE and UMAP, are often selected based on visual appeal alone and without rigorous quantitative validation. A major reason is that manifold embeddings typically do not provide an out-of-sample map nor an inverse back to the original feature space; this makes held-out validation, the gold standard in supervised learning, all but impossible. To address these challenges, we develop a novel framework, MEDAL (Manifold Embedding Distillation via Autoencoder Learning), which distills a fitted manifold embedding into a reusable encoder-decoder model. MEDAL trains a constrained autoencoder whose bottleneck exactly matches any teacher embedding while the decoder reconstructs the original input; this yields an explicit map for new samples, an approximate inverse, and a pointwise reconstruction-based measure of distortion in the manifold space. This converts static manifold embeddings into models that can be evaluated on held-out data, enabling quantitative validation including comparing different dimension reduction methods as well as hyperparameter tuning. Across multiple benchmark and scientific case studies, we show that MEDAL enables held-out validation to determine optimal manifold embeddings and hyperparameters, reveals biologically coherent regions that are difficult to preserve in two dimensional embeddings, and detects distribution shift when new samples are mapped into a fixed reference manifold. MEDAL provides a general validation wrapper to any existing dimension reduction technique that will improve the rigor and reliability of dimension reduction in scientific workflows.

1 Introduction

Data arising in modern scientific applications are often very high-dimensional. This growth in data dimensionality has made dimension reduction (DR) a central tool for modern scientific analysis. Broadly, DR seeks to map observations from \mathbb{R}^p into a much lower-dimensional space \mathbb{R}^d , where $d \ll p$, while preserving structure relevant to exploration, interpretation, and downstream analysis. A

[†]Corresponding author: genevera.allen@columbia.edu

large methodological toolbox has been developed for this purpose. Linear methods such as Principal Component Analysis (PCA) [48] are well-understood, but limited in their ability to represent nonlinear structure that are present in complex, modern datasets. Neighborhood- and graph-based nonlinear methods were introduced to overcome this limitation, beginning with classical approaches such as Isomap [92] and Locally Linear Embedding [85], and extending to modern methods such as t-SNE [98], UMAP [71], PHATE [76], and PaCMAP [102]. These methods are no longer used only as exploratory visualization tools. Across biomedicine and other data-intensive sciences, low-dimensional embeddings are fundamental for discovery, used to guide decisions about cluster structure, class separation, trajectory inference, and disease-related heterogeneity, including in settings such as cancer characterization via single-cell transcriptomics, biomedical imaging, and electrophysiological measurements of neural activity [12, 18, 23, 25, 29, 34, 56, 70, 75, 80, 108, 110]. As a result, an embedding is not merely a picture; it is often treated as a scientifically meaningful representation of the data, and its reliability can directly affect critical downstream conclusions.

Despite this importance, the way embeddings are often used in practice remains surprisingly qualitative. Researchers frequently choose a DR method and its hyperparameters based on defaults or visual appeal, and then proceed as if the resulting geometry were a faithful representation of the underlying data. This workflow is fragile. Small changes in initialization, preprocessing, feature selection, or hyperparameter choice can materially alter the geometry of an embedding [35, 57, 94, 102], and recent critiques have highlighted how easily visually compelling maps can be over-interpreted as scientific evidence [22, 49, 50]. This has also contributed to the greater crisis in rigor and reproducibility in modern science [79], as these sensitive embeddings are used in consequential and critical scientific workflows. This fragility calls for more principled ideas from model validation and reliability assessment.

A growing literature has begun to address the problem of validation in dimension reduction [1], particularly through work on hyperparameter tuning and embedding reliability. Existing approaches include post-hoc selection criteria tailored to particular applications or notions of embedding quality [17, 37, 52, 63, 109], optimization-based formulations of hyperparameter search [62, 78, 101], and tools for scaling visual or interactive exploration of embedding behavior [3, 89]. Most closely related are methods that score local embedding reliability, including empirical-null or resampling-based approaches such as EMBEDR and scDEED [51, 89, 103], and geometric approaches based on map continuity or discontinuity such as neMDBD [64]. These methods address important aspects of the problem, but they remain task-specific or method-specific and do not provide the kind of principled held-out validation routine in supervised learning.

A central reason this gap persists is that principled validation is much easier for some DR methods than for others. For linear methods such as PCA, there exists both a forward map (projecting new data) and an inverse map (reconstruction from low-dimensional coordinates), providing a natural notion of reconstruction error. Therefore, a model trained on one subset of data can be tested by measuring information loss on held-out observations. This split-based approach mirrors the standard model selection procedure under supervised regime. By contrast, many widely used neighborhood-based nonlinear methods provide embeddings primarily for the training data and do not furnish a general, reliable way to embed new points or invert the map. As a result, nonlinear embeddings remain difficult to evaluate, compare, and reuse, despite already being deeply integrated in scientific workflows [20].

Previous work has incorporated neural networks directly into manifold learning to address the absence of an explicit out-of-sample map. Parametric t-SNE and Parametric UMAP [86, 97], for example, train a neural encoder from high-dimensional observations to low-dimensional coordinates,

as well as autoencoder-based approaches that learn latent representations through reconstruction objectives [96]. However, despite the appeal of these methods, many applied analyses still use standard t-SNE and UMAP embeddings as fixed objects of interpretation [50]. What is missing is therefore not yet another embedding method to replace the existing ones, but rather, a *general wrapper* that makes these nonparametric DR methods more reusable, comparable, and amenable to rigorous quantitative evaluation.

In this work, we propose **MEDAL**, a distillation framework that can be used to bridge the evaluation gap in DR by converting a fitted teacher embedding into a reusable model. MEDAL is inspired by knowledge distillation [43], in which a *student* model is trained to reproduce the behavior of a *teacher* model more efficiently. Unlike classic distillation, our ‘teacher’ is a pre-computed embedding. Given a teacher embedding from UMAP, t-SNE, Isomap, PCA or any other DR method, MEDAL trains a constrained autoencoder with two coupled objectives: (1) a distillation loss aligning the encoder with the teacher coordinates, and (2) a reconstruction loss that preserves input-space information. (Figure 1A). Once distilled, the embedding is no longer merely a static visualization; it becomes a model with an explicit forward map, an approximate inverse, and a pointwise reconstruction-based measure of information loss.

By equipping otherwise nonparametric embeddings with a shared learned mapping, MEDAL enables several capabilities that are typically unavailable within a single DR workflow (Figure 1B). First, it makes held-out validation possible: new observations can be mapped into a fixed reference manifold and reconstructed back to the original space, hence embeddings can be assessed by how much information they preserve out of sample rather than by visual appeal alone. Second, this provides a principled basis for hyperparameter selection, since candidate teacher embeddings can be compared by held-out reconstruction error under a common protocol. More broadly, MEDAL creates a common evaluation scale for comparing different DR methods, a task that is otherwise difficult because PCA, UMAP, t-SNE, and related approaches provide different objects, diagnostics, and notions, or lack of notions, of goodness-of-fit. By scoring all teachers through the same learned reconstruction map, MEDAL allows method comparisons to be based on preserved input-space information rather than on method-specific heuristics or visual inspection. Finally, because reconstruction error is defined pointwise, MEDAL enables localized distortion analysis, identifying where the manifold is least faithfully represented. In this way, MEDAL does not replace existing DR methods, rather, it augments them with the tools needed for rigorous validation and interpretation.

2 Methods

2.1 Overview: MEDAL as the validation protocol

Linear methods like PCA allow for held-out validation because they provide both forward and inverse maps, making reconstruction error a natural measure of information loss. By contrast, widely-used nonlinear methods such as t-SNE, UMAP, and Isomap do not furnish general forward and inverse maps, making them difficult to evaluate on held-out data. MEDAL restores this validation structure by distilling an embedding generated from *any* DR method of choice—the teacher—into an autoencoder. Autoencoders are encoder–decoder neural network models that learn low-dimensional representations by reconstructing the input from a compressed latent space [44]. In MEDAL, the compressed latent coordinates are not learned freely; instead, the encoder

bottleneck is constrained to match a prescribed teacher embedding, while the decoder reconstructs the original high-dimensional input.

The MEDAL workflow is as follows: We first split the data into a training set X_{tr} and a held-out validation set X_{val} . A teacher dimension reduction method is fitted only on X_{tr} , producing training coordinates Z_{tr} . We then train a student autoencoder on X_{tr} until the encoder matches the teacher embedding, Z_{tr} , to a predefined, very small alignment threshold. The resulting encoder provides an out-of-sample map into the fitted teacher manifold, while the decoder turns reconstruction error into a quantitative measure of information preserved by that manifold. The held-out X_{val} is then passed through the learned encoder–decoder pair to obtain reconstruction errors for each validation observation. These errors provide a common basis for the four applications developed below, namely hyperparameter selection within a DR method, pointwise distortion analysis, out-of-sample embedding, and comparison across DR methods.

The remainder of this section describes details on student training for rigorous interpretation, and then outlines the downstream validation tasks enabled by the resulting encoder–decoder pair.

2.2 The MEDAL training objective

Let

$$X_{\text{tr}} = \{x_i\}_{i=1}^{n_{\text{tr}}} \subset \mathbb{R}^p$$

denote the training observations in the original feature space. The teacher T can be any dimension-reduction method fitted to X_{tr} , producing low-dimensional coordinates

$$Z_{\text{tr}} = \{z_i\}_{i=1}^{n_{\text{tr}}} \subset \mathbb{R}^r, \quad r < p.$$

Here z_i denotes the fitted teacher coordinate assigned to x_i .

MEDAL trains an encoder–decoder pair

$$e_{\theta} : \mathbb{R}^p \rightarrow \mathbb{R}^r, \quad d_{\phi} : \mathbb{R}^r \rightarrow \mathbb{R}^p,$$

where the encoder bottleneck is constrained to reproduce the teacher coordinates and the decoder reconstructs the original input. The reconstruction loss on the training split is

$$\mathcal{L}_{\text{rec}}(X_{\text{tr}}; \theta, \phi) = \frac{1}{n_{\text{tr}}} \sum_{i=1}^{n_{\text{tr}}} \|x_i - d_{\phi}(e_{\theta}(x_i))\|^2,$$

and the distillation loss is

$$\mathcal{L}_{\text{dist}}(X_{\text{tr}}, Z_{\text{tr}}; \theta) = \frac{1}{n_{\text{tr}}} \sum_{i=1}^{n_{\text{tr}}} \|e_{\theta}(x_i) - z_i\|^2.$$

Conceptually, MEDAL seeks to minimize reconstruction while enforcing close agreement between the student bottleneck layer and the teacher embedding:

$$\min_{\theta, \phi} \mathcal{L}_{\text{rec}}(X_{\text{tr}}; \theta, \phi) \quad \text{s.t.} \quad \mathcal{L}_{\text{dist}}(X_{\text{tr}}, Z_{\text{tr}}; \theta) \leq \varepsilon, \quad (1)$$

for a small alignment tolerance $\varepsilon \geq 0$. Operationally, we solve a Lagrangian relaxation of this problem, with a penalty λ_d on the distillation loss

$$\min_{\theta, \phi} \mathcal{L}(\theta, \phi) = \lambda_d \mathcal{L}_d(X, Z; \theta) + \mathcal{L}_r(X; \theta, \phi), \quad \lambda_d \geq 0. \quad (2)$$

After training, let $(\hat{\theta}, \hat{\phi})$ denote the fitted student parameters. For a held-out observation $x \in X_{\text{val}}$, MEDAL produces the out-of-sample coordinate

$$\hat{z} = e_{\hat{\theta}}(x),$$

and the corresponding reconstruction

$$\hat{x} = d_{\hat{\phi}}(\hat{z}) = d_{\hat{\phi}}(e_{\hat{\theta}}(x)).$$

The held-out reconstruction error is then

$$\ell_{\text{val}}(x) = \left\| x - d_{\hat{\phi}}(e_{\hat{\theta}}(x)) \right\|^2.$$

2.3 The design of MEDAL

MEDAL departs from a conventional autoencoder in one critical respect. Its bottleneck is not freely learned but constrained to follow a prescribed teacher embedding (t-SNE, UMAP, or any other DR method), and reconstruction error is interpretable as a property of that embedding only when this constraint is enforced tightly. If the bottleneck deviates from the teacher coordinates, the resulting error conflates two distinct sources of loss—information discarded by the teacher and fitting error introduced by the student—with no way to separate them. We therefore require distillation to reach a predefined near-zero alignment threshold before any reconstruction-based comparison is made, and we treat this requirement as a prerequisite that drives the rest of the design.

That this prerequisite can be met at all rests on a known property of expressive neural networks. Given sufficient capacity, they can interpolate arbitrary targets on a finite training set [106]. In our setting, the teacher coordinates z_i play the role of finite-sample targets for the encoder. In practice, we find that two to five hidden layers with a symmetric decoder suffices; very deep or very wide networks bring no benefit and only complicate optimization. The right depth and width are dataset-dependent, and we set them through architecture-capacity experiments, favoring the smallest configuration that achieves near-zero distillation reliably. Under a fixed parameter budget, high-dimensional inputs typically prefer narrower hidden layers, since the input-to-hidden and hidden-to-output maps already absorb much of the budget.

Nonlinear activations are what give the encoder enough expressiveness to reach near-zero distillation, but they are placed selectively rather than throughout. Hidden layers use ReLU [77] or SELU [54] activations, but the bottleneck mapping and the final reconstruction layer are linear. The linear bottleneck matters because teacher coordinates may be signed or scaled differently across DR methods, hence passing them through a nonlinearity would impose artificial range restrictions inconsistent with the teacher we seek to reproduce. The linear output layer matters because the reconstruction targets live in the full input space without bounded constraints.

Even with the right architecture, the distillation loss does not vanish on its own—it must be driven there by the penalty λ_d in Equation 2. Too small a value leaves the bottleneck free to drift from the teacher, silently invalidating the scores. We sweep λ_d on a logarithmic grid per dataset and adopt the value at which the alignment criterion is reliably met. The trade-off this incurs is mild. As Supplementary Figure S1 shows, tightening λ_d improves teacher matching by orders of magnitude while raising reconstruction error only marginally. Runs that fail the alignment criterion are discarded from downstream comparisons.

For comparisons across teacher methods or teacher hyperparameters, the student itself must also be held fixed. We use the same architecture and training protocol within each dataset so that differences in reconstruction error should reflect differences in the teacher manifold, not differences in student capacity. Some teacher embeddings are more difficult to distill than others, so we train with a generous maximum optimization budget but terminate early once the distillation loss reaches the predefined threshold. Embeddings that are easier to distill therefore terminate training early, while harder ones are given the full budget to reach the same threshold. Under this protocol, the final student bottleneck is essentially indistinguishable from the teacher embedding, exemplified in (Figure 1C) where we place different teachers on a common basis for reconstruction-based comparison.

A final question is whether reconstruction remains meaningful when the bottleneck is constrained to follow a prescribed manifold embedding. We address this directly by using PCA as the teacher on MNIST and comparing reconstruction curves across bottleneck ranks for four models: PCA itself, a vanilla autoencoder trained only for reconstruction, linear MEDAL, and nonlinear MEDAL. Here, linear MEDAL denotes a distilled model with linear activations throughout the encoder and decoder, whereas nonlinear MEDAL uses nonlinear hidden layers with linear maps into the bottleneck and out to the output. Both MEDAL variants are distilled from the same PCA teacher. In Figure 2D, linear MEDAL exactly matches the PCA reconstruction curve across bottleneck ranks, as expected [5, 13, 82]. This confirms that the distillation constraint itself does not introduce additional reconstruction artifacts. With nonlinear students, MEDAL distilled from the same PCA teacher remains competitive with an unconstrained autoencoder and can outperform PCA at moderate to large bottleneck ranks. Together, these results show that enforcing teacher alignment need not degrade reconstruction quality, supporting reconstruction error as a meaningful quantitative signal after successful distillation. Additional architecture experiments, optimization details, and stopping criteria are provided in Supplementary Section S2 and Supplementary Section S2.3.

2.4 Downstream validation tasks enabled by MEDAL

After a teacher embedding has been distilled into an encoder–decoder pair, MEDAL can be used as a validation layer for several dimension-reduction workflows.

Task 1: Hyperparameter selection within a dimension reduction method. In practice, hyperparameters for methods such as t-SNE and UMAP are often chosen by visually inspecting the resulting two-dimensional embeddings. MEDAL turns hyperparameter selection for a fixed dimension reduction method into a held-out validation problem, the gold-standard type of validation in supervised learning. For any DR method, each candidate hyperparameter setting is used to fit a teacher embedding on X_{tr} . The resulting embedding is then distilled into a student autoencoder and evaluated on X_{val} by held-out reconstruction error. Since student training may vary across random initializations, we repeat distillation multiple times for each teacher embedding and retain only runs that reach the predefined near-zero alignment threshold. Validation reconstruction error is then summarized across successful runs, yielding a validation curve over the candidate hyperparameter values. We select hyperparameters from this curve, for example using the minimum or one-standard-error rule [16]. As all candidates use the same method family and are distilled to the same alignment threshold under a shared student architecture, differences in validation reconstruction error can be attributed to the hyperparameter choice alone, providing a principled criterion for selection.

Task 2: Pointwise distortion analysis. Low-dimensional manifold embeddings are known to introduce distortion, because compressing high-dimensional structure into two or three dimensions can alter neighborhoods, distances, densities, and global organization, thereby affecting apparent clusters and downstream scientific conclusions [73]. Since reconstruction error is defined for each observation, MEDAL supports pointwise distortion analysis. Observations with large reconstruction error identify regions where the fitted low-dimensional geometry least faithfully preserves the original high-dimensional structure. These pointwise errors can be summarized by class, cell type, batch, domain, or other metadata to identify systematic regions of embedding infidelity.

Task 3: Detection of distribution shift. MEDAL can also be used to detect when new observations are poorly represented by a reference manifold. A teacher embedding is fitted and distilled on a reference training distribution, and the learned encoder–decoder pair is then applied to new observations, batches, or domains. If these observations have systematically larger reconstruction errors than held-out reference observations, this indicates that they are not well captured by the fitted low-dimensional geometry. Thus, MEDAL provides a reconstruction-based diagnostic for distribution shift relative to a reference embedding.

Task 4: Comparison across dimension reduction methods. Prior to this work, comparisons across dimension reduction methods lacked a shared validation principle, leaving method choice largely dependent on qualitative visual judgment. MEDAL provides a common reconstruction-based criterion for comparing fitted embeddings across different dimension reduction methods. Within a dataset, each candidate method (e.g., t-SNE, UMAP, Isomap, PCA, and etc.) is fitted to X_{tr} using a fixed or optimized (from Task 1) hyperparameter configuration. Following the same distillation and validation protocol as Task 1, each embedding is evaluated by its validation reconstruction error. The method that achieves the lowest validation reconstruction error is preferred, as this indicates its geometry best preserves information on new observations. Because all methods are evaluated under the same student architecture, training procedure, and validation split, differences in reconstruction error reflect differences in the methods’ underlying geometry rather than asymmetries in the evaluation protocol.

3 Results

We evaluate MEDAL as a validation framework through four case studies that progress from a controlled benchmark to biological applications. On the MNIST benchmark [59], we demonstrate Tasks 1, 2, and 4 in a setting with known class structure. We then apply the same workflow to two single-cell RNA-seq datasets, on whole-animal Hydra from [87] and on mouse neocortex from [91], showing that these tasks extend to single-cell genomics datasets where reconstruction error highlights biologically interpretable distortion. We further compare MEDAL with existing embedding-diagnostic methods for Tasks 1 and 4. Finally, using a single-cell RNA-seq macaque retina dataset with multiple experimental subjects from [81], we demonstrate Task 3: reference-based detection and localization of distribution shift.

3.1 Case study: MNIST benchmark

We begin with the MNIST handwritten dataset [59] as a controlled proof of principle, using its known digit labels and well-understood visual structure to assess whether MEDAL produces quantitative signals that agree with intuitive embedding quality. In this benchmark setting, we use MEDAL to demonstrate held-out hyperparameter selection, comparison across dimension-reduction methods, and pointwise distortion analysis.

Task 1: Tuning `n_neighbors` on UMAP On MNIST visualizations, suboptimal hyperparameters do not necessarily produce embeddings that are visibly poor. Many training-set embeddings appear plausible by visual inspection, even when they differ in how well they preserve structure for held-out observations. We therefore ask whether MEDAL can distinguish embeddings that look similarly acceptable in sample but differ in out-of-sample information preservation.

Consistent with this validation curve (Figure 2A), the MEDAL-selected embedding (`n_neighbors` = 35) balanced class separation with global coherence (Figure 2A). In contrast, a large-neighborhood embedding (`n_neighbors` = 186) compressed several digit classes into nearby regions of the manifold, producing a visually plausible but less discriminative embedding. A small-neighborhood embedding (`n_neighbors` = 6) produced sharper apparent separation on the training set, but fragmented the manifold and placed some held-out observations far from their corresponding class regions (Figure 2B). This behavior is consistent with overfitting to training structure, where normally the training reconstruction loss is low, but validation and test reconstruction loss increase sharply. By contrast, the selected embedding avoided both extremes. When held-out digits are embedded onto the manifold of the training data, they remained close to the appropriate class structure without excessive compression across classes, or excessive fragmentation within classes. Thus, even in a simple dataset such as MNIST, the most visually appealing training embedding is not necessarily the one that best preserves structure out of sample.

Task 2: Distortion investigation Next in Figure 2A, the scattered or unstable points are precisely those estimated with high reconstruction error, indicating where the low-dimensional manifold is most poorly represented. Importantly, these high-error points are not arbitrary. As shown in Figure 2E, nearby points on the same manifold can differ markedly in reconstruction quality. Low-error digits are typically reconstructed faithfully, whereas high-error digits tend to be more ambiguous, atypical, or poorly written, and their reconstructions are visibly blurrier and less accurate. Reconstruction error therefore carries semantic information about sample difficulty. It identifies which observations are naturally accommodated by the learned geometry and which are being forced into it with greater distortion.

Task 4: Comparing DR methods On MNIST, we compare t-SNE, UMAP, spectral embedding, PHATE, and PCA, using each method at its selected hyperparameter where applicable (Figure 2D; Supplementary Figure S7). UMAP at its selected hyperparameter achieved strong held-out reconstruction performance and produced a coherent manifold under this criterion. In contrast, methods such as PCA and spectral embedding retained less information in this setting.

3.2 Case study: Hydra single-cell RNA-seq dataset

We next evaluated MEDAL on a whole-animal *Hydra* single-cell RNA-seq dataset, comprising approximately 25,000 cells spanning the major Hydra lineages [87]. Hydra is a stringent testbed because it is both biologically well-characterized and developmentally dynamic; cells are continuously renewed, and the interstitial lineage in particular contains rich transitional structure [103]. This makes Hydra well-suited for determining whether a quantitatively selected two-dimensional embedding truly recovers known biology rather than merely producing an appealing visualization.

Task 1: Perplexity tuning on t-SNE The MEDAL-selected perplexity (499) recovered the major Hydra lineages—endoderm, ectoderm, and interstitial—and projected validation and test cells into the same lineage-specific regions of the training manifold (Figure 3A,C). In comparison, a smaller perplexity (5) produced a sharper, more fragmented embedding, with finer local separation on the training set but a more diffuse and less stable organization for held-out cells (Figure 3B). At the opposite extreme, a much larger perplexity (4999) over-smoothed the manifold, compressing biologically distinct populations into a more globally constrained layout and reducing separation across lineages. The selected perplexity avoided both extremes: it preserved broad lineage structure without excessive fragmentation at low perplexity or excessive compression at high perplexity. Thus, the embedding that appears most granular or most globally smooth on the training set is not necessarily the one that best preserves biological structure out of sample.

Task 2: Distortion analysis In Hydra, high-error regions are repeatedly concentrated in the same biologically distinct cell populations, including interstitial nematocytes, basal disk epithelial cells, and male germline cells (Figure 3E). We interpret this pattern cautiously, but its consistency is notable. These are not arbitrary outliers; rather, they correspond to cell populations that are either developmentally active or highly specialized, suggesting that two-dimensional compression struggles to represent their complex transcriptomic variability [28, 45, 87].

Importantly, the same cell types remained highlighted across embeddings with different perplexities (Supplementary Figure S9), suggesting that MEDAL is detecting a stable biological signature of distortion rather than an artifact of a single visualization.

3.2.1 Comparison with existing embedding diagnostics

We next ask whether the distortion signal identified by MEDAL on Hydra was also recovered by existing embedding validation methods. We compared MEDAL with EMBEDR [51], scDEED [103], and neMDBD [64], three methods that assign pointwise measures of embedding reliability or distortion and can be used to guide hyperparameter selection. These competing diagnostics score an embedding generated from a single fit on the training data. MEDAL instead provides an out-of-sample criterion for hyperparameter selection, asking whether the selected embedding remains stable for held-out observations. On Hydra, this criterion selected an intermediate embedding that balanced local cell-state neighborhoods with global lineage organization while preserving consistent held-out placement. Competing methods often selected hyperparameters at the edge of the search grid (Figure 4A), where very small perplexities can fragment the manifold and very large perplexities can compress distinct biological populations into a smoother but less discriminative layout. Although MEDAL’s assessment is mediated by its learned encoder–decoder map, that mapping is precisely what enables the held-out test that the competing in-sample diagnostics lack.

MEDAL also produced a more interpretable pointwise distortion signal. High reconstruction error localized to biologically identifiable populations (Figure 3E). On the other hand, competing pointwise signals were more diffuse and less directly interpretable (Figure 4B). Thus, MEDAL reconstruction error served not only as a tuning criterion, but also as a biological diagnostic for cell populations whose transcriptomic structure was difficult to preserve in two dimensions.

To connect these qualitative patterns with external structure-preservation criteria, we evaluated each selected embedding using the Local Continuity Meta-Criterion (LCMC) for local neighborhood preservation and random triplet accuracy for broader distance-order preservation [2]. These metrics are not intended to define a single ground truth for embedding quality, but they show that MEDAL selects embeddings that preserve recoverable high-dimensional signal while remaining competitive with standard local and global structure-preservation summaries (Supplementary Table S2). At the same time, MEDAL provides a clear computational advantage. On the Hydra data set with t-SNE, MEDAL completed a full hyperparameter sweep substantially faster than EMBEDR and scDEED, and neMDBD (Table 1). Supplementary runtime comparisons show that this advantage persists across datasets and teacher families Supplementary Figures S16–S20. This per-seed efficiency makes repeated distillations and averaged validation curves feasible at the scale of large biological datasets, whereas repeatedly rerunning null-, permutation-, or geometry-based diagnostics across seeds and hyperparameter grids is considerably more costly.

Method	Computation Time (min)
MEDAL	43.08 ± 4.81
neMDBD [64]	63.39 ± 0.39
EMBEDR [51]	109.51 ± 16.79
scDEED* [103]	351.02 ± 1.54

Table 1: Computation time on the Hydra dataset using t-SNE as the teacher embedding. Times are reported in minutes as mean ± SE across 3 seeds. scDEED (*) was run after PCA preprocessing, following its recommended workflow.

3.3 Case study: mouse neocortex single-cell RNA-seq dataset

We next applied MEDAL to mouse neocortical single-cell RNA-seq data first reported by Tasic et al. [91]. This dataset contains 23,822 cells collected from two distant cortical areas, primary visual cortex (VISp) and anterior lateral motor cortex (ALM). The original study resolved 133 transcriptomic cell types and showed that most GABAergic types are shared across areas, whereas many glutamatergic types are area-specific. The rich structures and extensive annotations, containing both major neuronal classes and a smaller set of non-neuronal populations, make the Tasic et al. [91] dataset a strong biological test case for manifold learning.

Task 1: Perplexity tuning on t-SNE. MEDAL selected a perplexity of 53, which preserved major cell-class organization and placed validation and test cells into the corresponding regions of the training manifold (Figure 5A). The non-selected perplexities illustrate the same two failure modes observed in the previous case studies: overfitting to local substructure at very small perplexity (5), and over-compression at a large perplexity (1241) (Figure 5B). This low-perplexity behavior is relevant to the original Tasic atlas setting, where the analysis emphasized fine transcriptomic

subtype structure across many annotated cortical cell types [91]. Our perplexity-5 embedding represents an intentionally more local version of this regime, illustrating how visually sharp subtype separation on the training set can come at the cost of poorer organization for held-out cells.

Task 2: Distortion analysis. In the selected t-SNE embedding, as in the Hydra dataset, high-error regions were not randomly distributed across the manifold. Instead, they concentrated in specific broad cell classes, especially non-neuronal and endothelial populations, whereas the major neuronal classes—GABAergic and glutamatergic neurons—were reconstructed more faithfully (Figure 5D). This pattern is biologically plausible given the dominant geometry of the atlas is largely organized by neuronal heterogeneity, with many resolved GABAergic and glutamatergic subclasses, while non-neuronal populations form smaller and transcriptionally distinct groups. In a global two-dimensional embedding of this taxonomy, smaller or more specialized populations may be harder to represent without loss if their variation is not aligned with the dominant structure of the embedding. This distortion signal was also consistent beyond the selected t-SNE embedding. In Supplementary Figure S11, the same broad pattern appeared for a small-perplexity t-SNE teacher and for a UMAP teacher—higher reconstruction error again localized disproportionately to non-neuronal and endothelial regions.

Task 4: Comparison across dimension-reduction methods We observe consistent results as in the MNIST benchmark previously. t-SNE at its selected perplexity achieved the lowest held-out reconstruction loss among the methods considered, followed by UMAP, while spectral embedding and PCA retained substantially less information (Figure 5C).

3.4 Case study: evaluate macaque retina single-cell RNA-seq data on Task 3

Finally, we used the macaque retina dataset [81] to illustrate Task 3: detecting distribution shift relative to a fixed reference manifold. Once a teacher manifold has been distilled, new observations can be mapped into a fixed reference space and evaluated by reconstruction error. This allows MEDAL to ask whether incoming observations are supported by the geometry of the reference distribution, rather than simply forcing them into an existing low-dimensional visualization.

We applied this idea to a single-cell RNA-seq dataset of macaque retinal cells collected across multiple subjects, denoted macaque 1 (M1), macaque 2 (M2), and macaque 3 (M3). This dataset provides a useful test case because retinal cell identity is strongly structured, but inter-subject and batch variation can substantially affect joint single-cell embeddings. Multi-sample single-cell analyses often require explicit batch correction or data integration to avoid confounding biological cell-type structure with technical or donor-specific effects [39, 58, 65, 88, 95]. Here, we do not attempt to pre-assess or correct these effects; instead, we use subject-level variation to test whether MEDAL reconstruction error can detect when new cells are poorly supported by a fitted reference manifold.

In the full macaque retina dataset, a joint t-SNE embedding appears coherent when colored by cell type, but coloring the same embedding by subject reveals strong subject-level structure across the manifold (Figure 6A). This motivates a reference-mapping question: if a manifold embedding is learned from one subject, can we detect new cells belonging to another subject that no longer conform to the reference geometry?

To test this, we trained MEDAL on M1 training cells and used the learned encoder to project two

held-out datasets onto the M1 reference manifold, an in-distribution batch of M1 test cells and a mixed batch containing M1 test cells together with M2 cells. MEDAL did not use subject labels when embedding or scoring these cells. For the in-distribution M1 test batch, cells were placed neatly into the existing M1 geometry, and reconstruction error remained low and spatially diffuse across the manifold. In contrast, in the mixed batch, the M1 test cells remained aligned with the reference structure, whereas M2 cells occupied a displaced region of the embedding and showed a spatially coherent increase in reconstruction error (Figure 6B). Thus, MEDAL detects out-of-distribution structure by displacing OOD cells relative to the reference manifold and assigning them higher reconstruction errors, while stably embedding in-distribution cells into the expected geometry.

We then asked which cell types contributed most strongly to this shift. Comparing cell-type-specific reconstruction errors between M1 test cells and M2 cells on the M1 reference manifold showed that the increase was not uniform across the atlas (Figure 6C). Although M2 cells generally had higher reconstruction error than the M1 baseline, the largest shifts occurred in microglia, endothelial cells, and pericytes. These non-neuronal populations are biologically plausible sources of subject-level mismatch because they often show stronger inter-individual, immune, vascular, or environmental variation than major neuronal cell classes. MEDAL therefore not only detects the presence of a distribution shift, but also localizes the mismatch to specific regions of the manifold and specific cell populations.

Additional analyses in the Supplementary Materials show that this signal is not specific to the M1-versus-M2 comparison. When M3 cells are projected onto the M1 reference manifold, reconstruction error again increases relative to the M1 baseline and remains concentrated in specific cell populations (Supplementary Figure S13). Reversing the reference subject by training MEDAL on M2 cells yields a similar pattern for M1 cells projected onto the M2 reference manifold (Supplementary Figure S14). MEDAL therefore augments out-of-sample embedding with a quantitative reliability signal for detecting and localizing distribution shift.

4 Discussion

Low-dimensional embeddings are now used as scientific summaries of complex high-dimensional data, yet the dominant workflow for nonlinear dimension reduction remains difficult to validate quantitatively. In this work, we introduced MEDAL as a model-agnostic framework for turning a fitted embedding into a reusable statistical object. Given a teacher embedding from any DR technique, MEDAL trains a constrained autoencoder whose encoder matches the teacher embedding and whose decoder reconstructs the original input. This distillation step converts an otherwise static manifold embedding into a model with an out-of-sample map, an approximate inverse, and a pointwise reconstruction-based measure of information loss.

Across benchmark and scientific datasets, this framework enabled several forms of validation that are typically unavailable in standard unsupervised workflows. MEDAL makes it possible to evaluate candidate embeddings on held-out observations, select hyperparameters using reconstruction error rather than visual inspection alone, compare different dimension reduction methods on a shared input-space scale, and localize regions of the embedding where low-dimensional compression is least faithful. In the biological case studies, the resulting pointwise distortion scores highlighted coherent cell populations and distribution-shifted samples, suggesting that MEDAL can be used not only to choose an embedding, but also to audit the resulting scientific conclusions.

Practically, MEDAL is designed to fit into the workflow that many scientists already use [20], while making the interpretation of that workflow more rigorous. A typical analysis fits a familiar method such as t-SNE or UMAP, where design decisions are determined by visual inspection of the resulting embedding, and uses that embedding as the basis for downstream claims. MEDAL inserts a validation step before the embedding is used for downstream analyses such as clustering, cell-type annotation, trajectory inference, differential expression, batch-effect assessment, or rare-population detection. With this increased confidence in embeddings, and hence, downstream scientific discovery, MEDAL is a significant contribution towards helping resolve the crisis in scientific reproducibility and replicability [79].

MEDAL’s role here, however, should be understood as validation of a *chosen teacher embedding*; it does not give an absolute guarantee that an embedding is scientifically correct. In fact, MEDAL inherits the assumptions and failures of the teacher. If the teacher removes biologically meaningful variation or emphasizes spurious structure, MEDAL will faithfully distill that geometry. Likewise, reconstruction error measures information loss relative to the given teacher manifold and student architecture. For this reason, MEDAL is best viewed as one quantitative validation criterion within a broader scientific workflow, to be considered alongside domain knowledge and complementary metrics of local or global structure preservation.

Several directions for future work follow naturally from this framework. First, MEDAL raises theoretical questions about when reconstruction error provides a reliable proxy for information loss, and how this criterion relates to teacher geometry, student capacity, neighborhood preservation, stability, and generalization in unsupervised learning [8, 10, 14, 60, 100]. Second, although MEDAL currently uses an MLP encoder–decoder as the student model, the same distillation principle could be paired with attention-based or transformer architectures that better capture structured dependencies among genes, features, or modalities [24, 93, 99, 104]. Third, MEDAL could be extended from single-modality embeddings to multimodal, multi-sample, and spatial datasets, where validation must account for multiple molecular measurements, experimental conditions, tissue sections, or spatial neighborhoods rather than a single feature matrix [4, 11, 15, 30, 36, 55]. Finally, connecting MEDAL to reference-atlas mapping and downstream analyses would place reconstruction-based validation directly within the scientific workflows that rely on low-dimensional representations for clustering, trajectory inference, annotation transfer, perturbation analysis, and disease-state discovery [41, 53, 66–68, 74].

MEDAL reframes dimension reduction from a purely *visual* endpoint into a quantitatively testable *modeling* step, and in doing so suggests a broader way to practice unsupervised learning. By distilling fitted embeddings into reusable encoder–decoder models, MEDAL brings the rigor and reproducibility of model selection and validation into a setting where such tools are often limited, treating latent representations not only as illustrations of structure but also as *hypotheses about it*. For statisticians and domain scientists alike, MEDAL points toward a broader research direction in which ideas from statistical inference, including generalization, stability, and structured model comparison, can be brought to bear on representation learning as an inferential activity. This perspective narrows the long-standing asymmetry between supervised and unsupervised methodology by making learned representations—even without labels—testable claims about structure rather than qualitative visual summaries.

Acknowledgments

The authors acknowledge funding from NSF DMS-2516872 and also thank Matthew Shen for developing an early prototype of the idea.

Data and Code Availability

All datasets analyzed in this study are publicly available. The mouse neocortex single-cell RNA-seq data [91] are available through the [Allen Institute Cell Types Database RNA-seq data portal](#) and at Gene Expression Omnibus (GEO) accession [GSE115746](#). The Hydra single-cell RNA-seq data [87] are available under GEO accession [GSE121617](#). The macaque retina single-cell RNA-seq data [81] are available from GEO under accession [GSE118546](#). For the APOGEE experiments, we used the processed globular cluster data and train–test splits released from Chang et al. [20], available from [90]. Additional documentation for the APOGEE preprocessing workflow is available at <https://dataslingers.github.io/unsupervised-workflow-astro/>.

Code implementing MEDAL and scripts for reproducing the main analyses are available at <https://github.com/DataSlingers/MEDAL> via [21]. Pre-processing scripts will be provided from the publicly available source data.

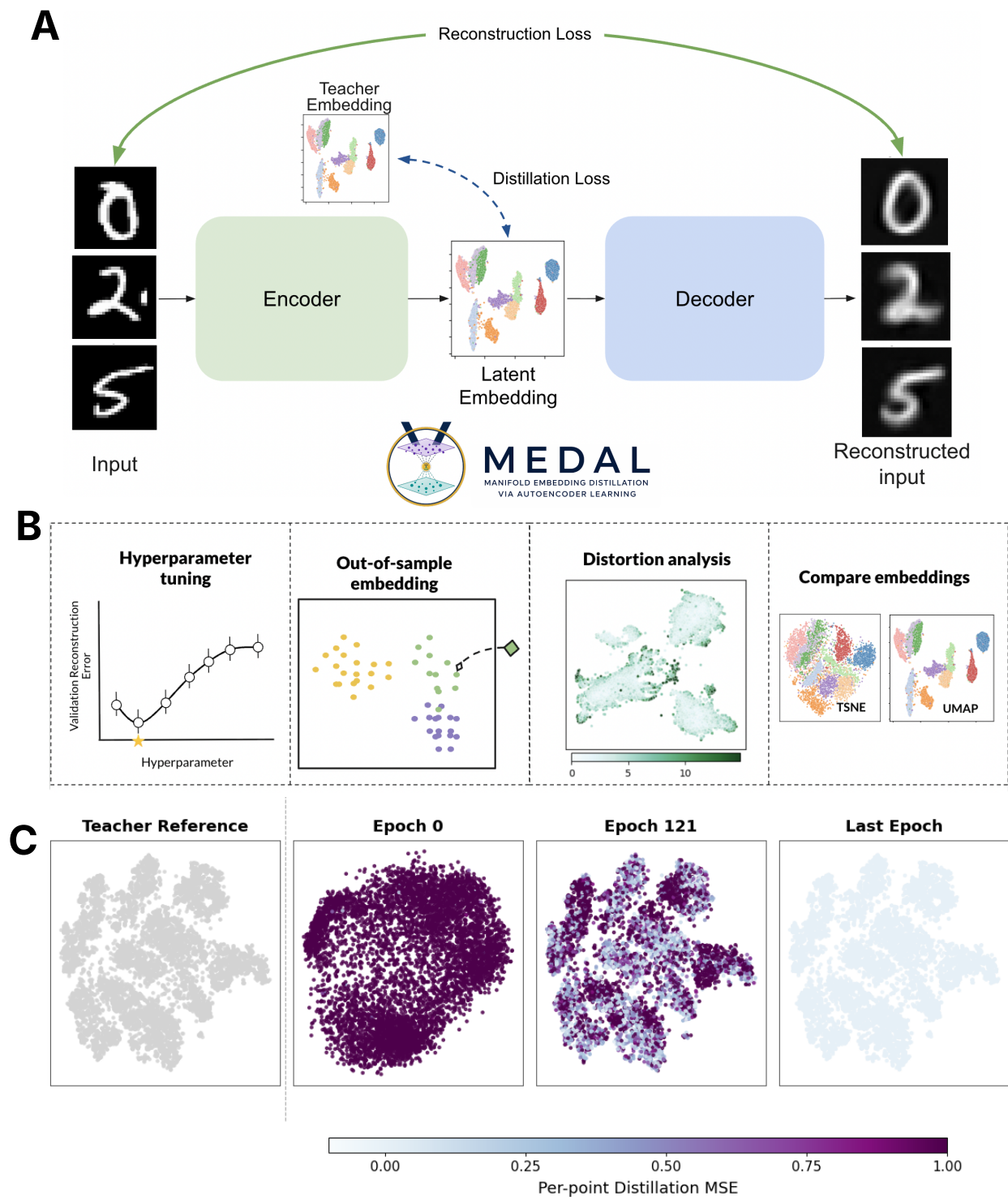


Figure 1

Figure 1: **MEDAL inputs a fitted manifold embedding and distills this into a reusable model that permits quantitative validation of the embedding.** **A**, MEDAL distills a teacher embedding into a constrained autoencoder by jointly optimizing a distillation loss that aligns the bottleneck with the teacher manifold and a reconstruction loss that preserves input-space information. **B**, Once distilled, the learned encoder–decoder supports held-out evaluation, hyperparameter selection, out-of-sample embedding, pointwise distortion analysis, and comparison across multiple manifold embeddings under a shared protocol. **C**, Distillation progression on MNIST data toward a t-SNE teacher embedding, showing convergence from random initialization to near-exact teacher matching.

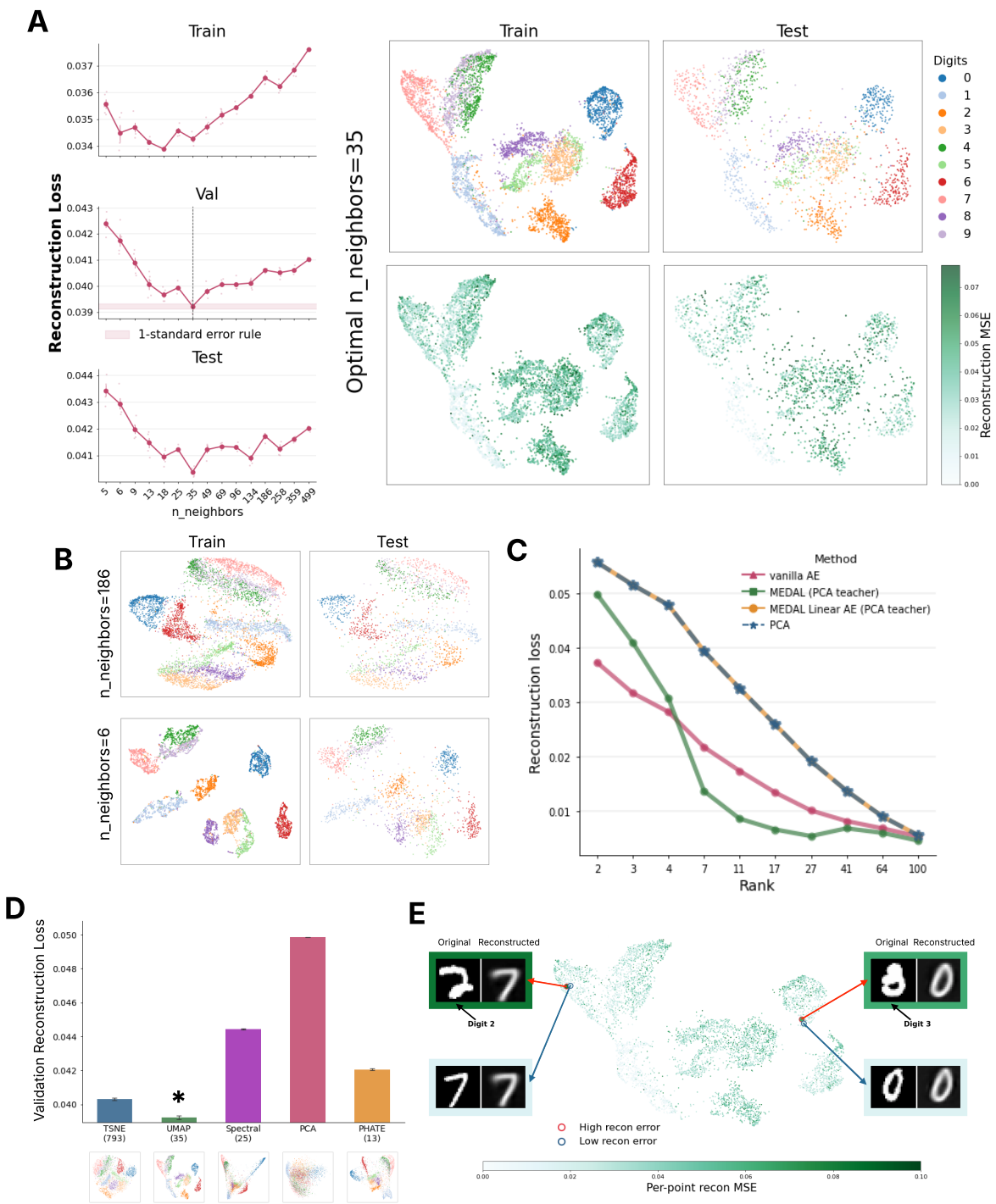


Figure 2

Figure 2: **MEDAL enables quantitative validation, comparison, and distortion analysis on MNIST data.** **A**, UMAP hyperparameter selection using held-out reconstruction error. For each value of `n_neighbors`, a fitted UMAP teacher embedding was distilled into a MEDAL student, and reconstruction loss was evaluated on train, validation, and test splits. The selected model (`n_neighbors=35`; dashed line) balances class separation with global coherence. The corresponding train and test embeddings are shown colored by digit label and by pointwise reconstruction error. **B**, Representative non-selected UMAP embeddings. A large-neighborhood embedding (`n_neighbors=186`) compresses digit classes into nearby regions, whereas a small-neighborhood embedding (`n_neighbors=6`) fragments the manifold and places some held-out observations far from their corresponding class regions. **C**, Reconstruction loss as a function of bottleneck rank for PCA, vanilla autoencoders, and MEDAL distilled from a PCA teacher. Linear MEDAL recovers the PCA reconstruction curve, as predicted by classical results linking linear autoencoders to principal subspaces [5, 13, 82], showing that MEDAL does not introduce artifacts through the distillation constraint. Nonlinear MEDAL remains competitive with an unconstrained autoencoder at larger ranks, further supporting reconstruction loss as a valid information preservation criterion under teacher-matching constraints. **D**, Held-out reconstruction loss provides a shared criterion for comparing dimension-reduction methods. Each nonlinear teacher is evaluated at its selected hyperparameter, with example embeddings shown below each bar. **E**, Pointwise reconstruction error localizes distortion within the selected UMAP manifold. Low-error observations are reconstructed faithfully, whereas high-error observations often correspond to ambiguous or atypical digit images whose reconstructions are visibly degraded.

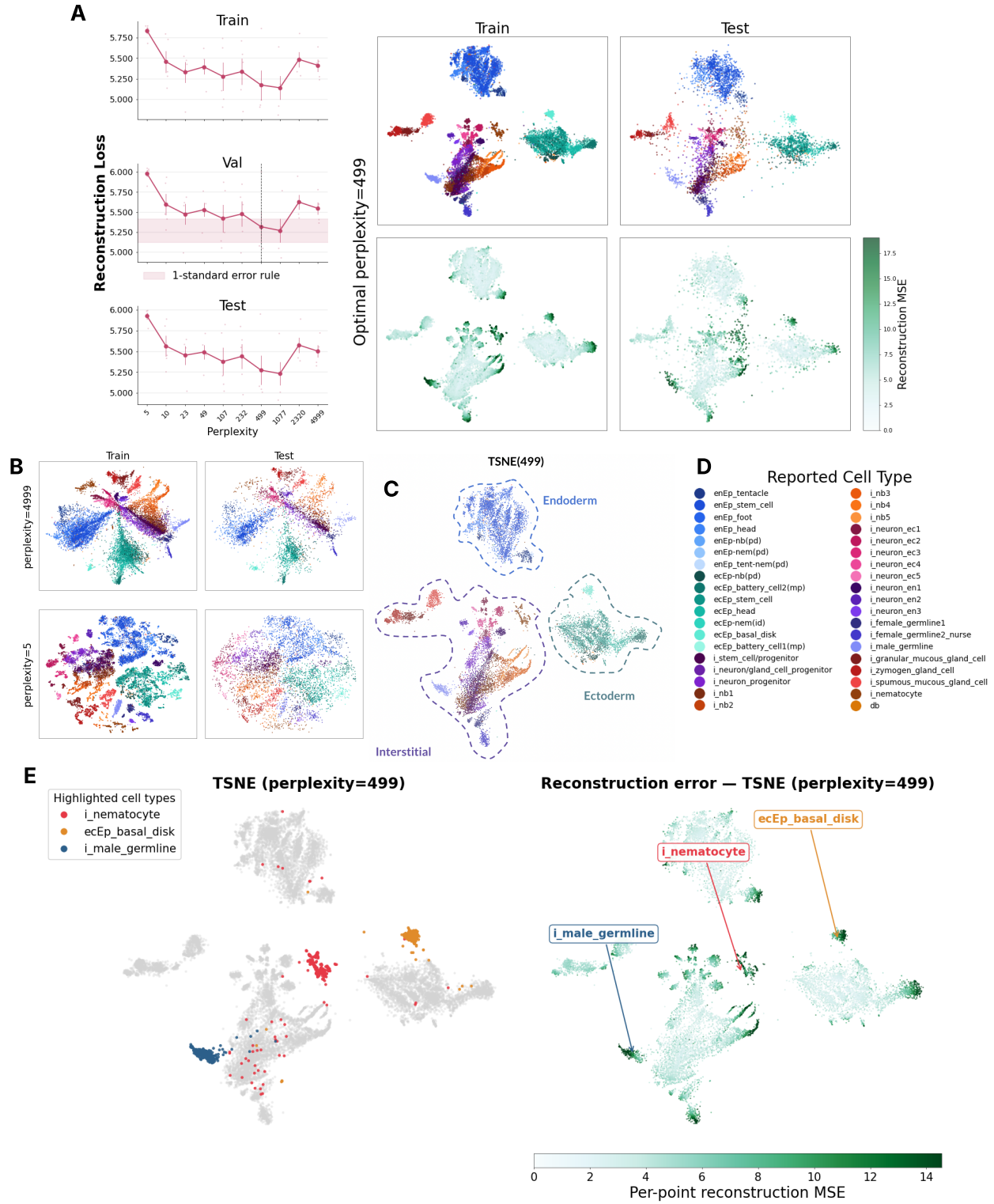


Figure 3

Figure 3: **MEDAL selects a biologically coherent embedding of the whole-animal Hydra single-cell RNA-seq dataset [87] and localizes cell-type-specific distortion.** **A**, MEDAL hyperparameter tuning for t-SNE teachers on the Hydra single-cell atlas. Reconstruction loss was evaluated across t-SNE perplexities on train, validation, and test splits. The selected perplexity, chosen by the validation curve using the one-standard-error rule, was 499. The corresponding training and test embeddings preserve the major Hydra lineages, and per-point reconstruction error highlights localized regions of high distortion. **B**, Comparison with unselected t-SNE perplexities. A very large perplexity (4999) produces a more globally compressed embedding in which distinct populations are drawn closer together, whereas a very small perplexity (5) fragments the manifold and generalizes poorly to held-out cells. **C**, The MEDAL-selected embedding recovers the three major Hydra lineages: endoderm, ectoderm, and interstitial cells. **D**, Reported cell-type annotations used to color the embeddings. **E**, Pointwise reconstruction error reveals biologically structured manifold embedding distortion. High-error regions are enriched in specific cell populations, including interstitial nematocytes, ectodermal basal disk epithelial cells, and male germline cells, suggesting that these dynamic or specialized populations are less faithfully represented by the two-dimensional manifold.

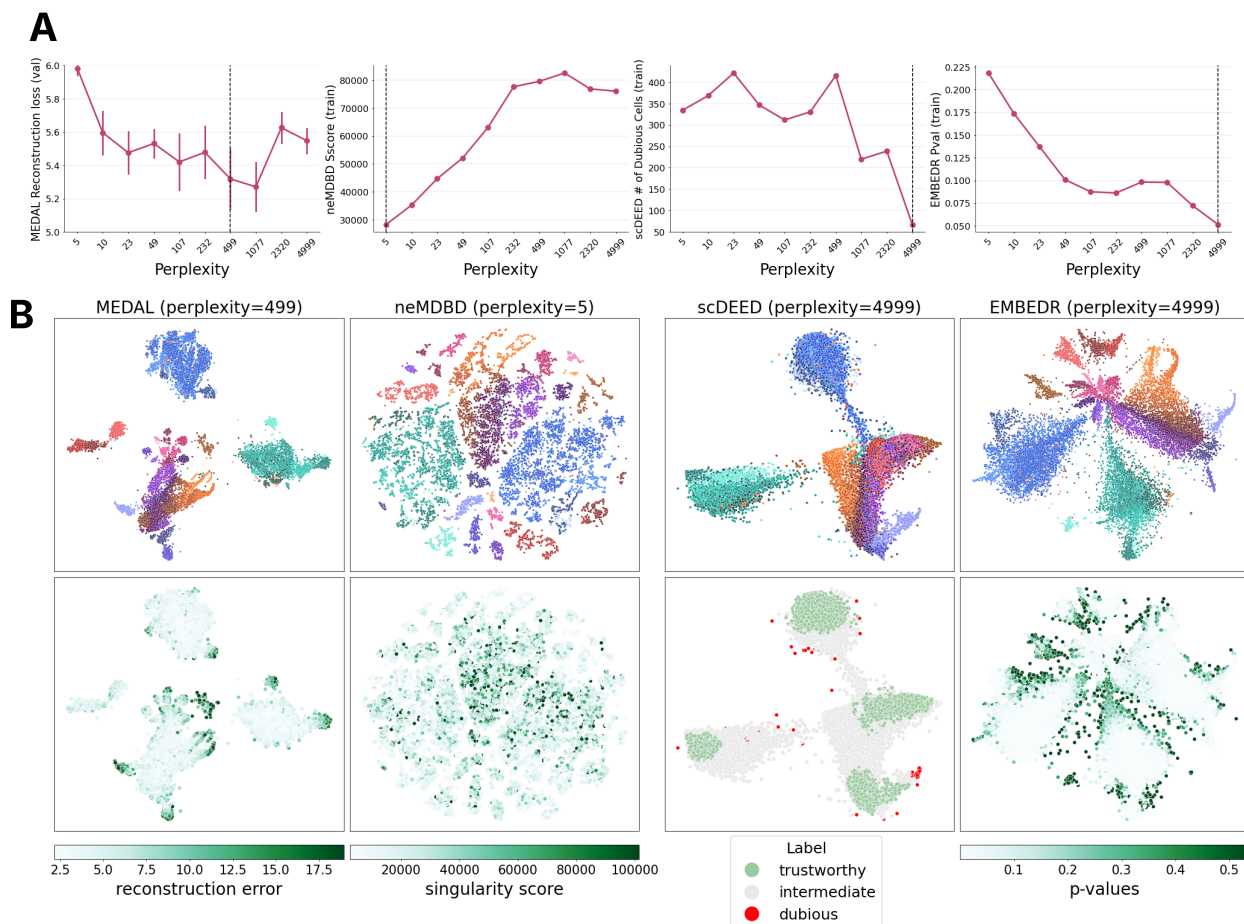


Figure 4: **Comparison of MEDAL with existing embedding diagnostics on a t-SNE embedding on Hydra ([87]) single-cell RNA-seq dataset.** **A**, Hyperparameter-selection curves across t-SNE perplexities for MEDAL, neMDBD ([64]), scDEED ([103]), and EMBEDR ([51]). Dashed vertical lines indicate the selected perplexity for each method. MEDAL selects perplexity 499 by held-out reconstruction loss, whereas neMDBD selects perplexity 5 and scDEED and EMBEDR select perplexity 4999. **B**, Hydra single-cell RNA-seq embeddings at each method’s selected perplexity. Top row: embeddings colored by reported cell type. Bottom row: pointwise diagnostic signals produced by each method: MEDAL reconstruction error, neMDBD singularity score, scDEED trustworthy/intermediate/dubious labels, and EMBEDR p-values. Because these methods are evaluated as deployed, this is a whole-system comparison: each method uses its own embedding implementation and optimization pipeline, so embeddings may differ even when the same perplexity is selected. MEDAL selects a more balanced embedding, retaining coherent lineage structure without favoring the extreme local or global regimes selected by competing diagnostics. Moreover, MEDAL’s pointwise reconstruction error has a direct interpretation as local information loss in the original feature space, making the resulting distortion map easier to interpret than method-specific singularity scores, reliability labels, or p-values.

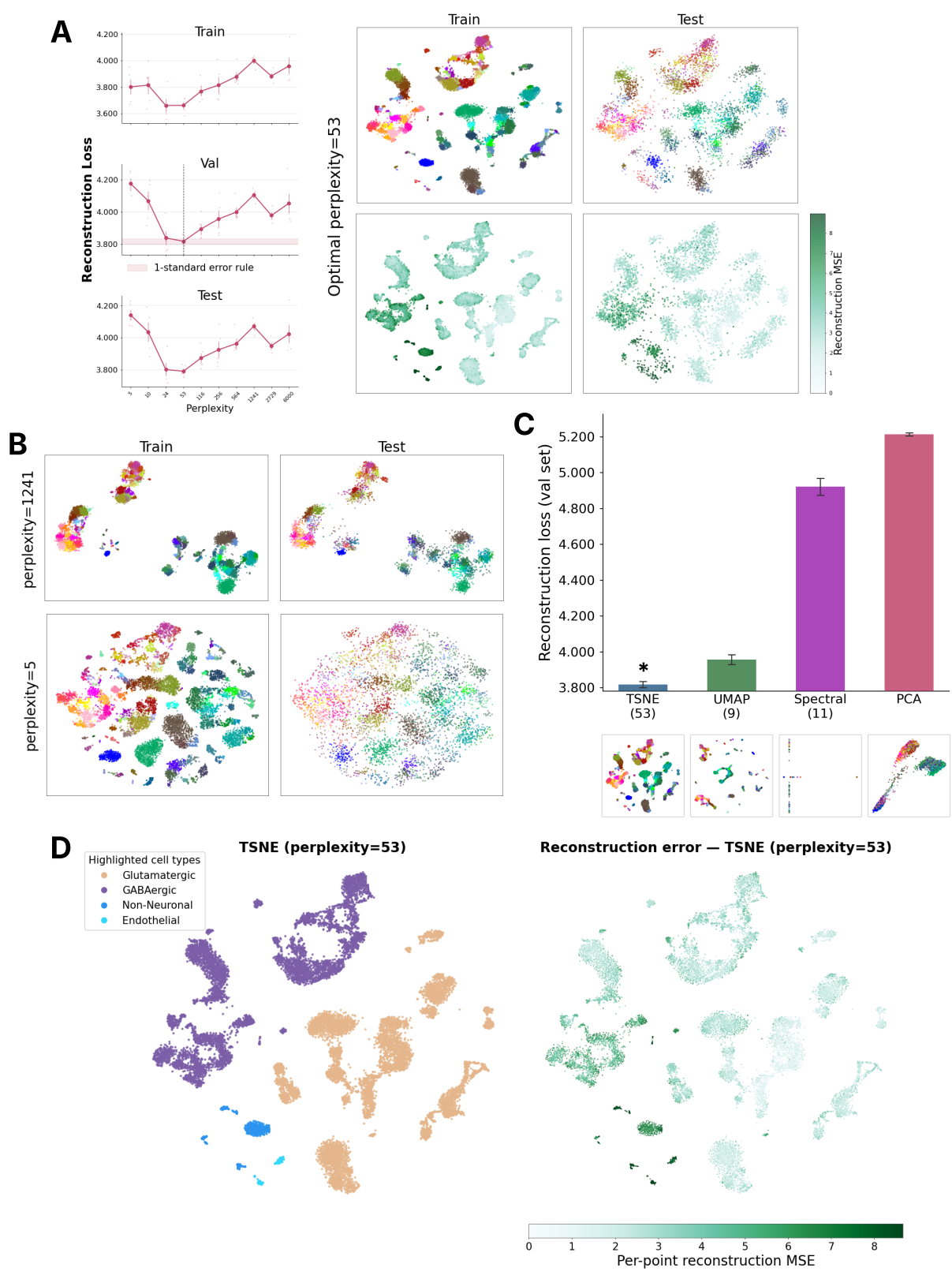


Figure 5

Figure 5: **MEDAL selects a manifold embedding for mouse neocortex single-cell RNA-seq ([91]) and reveals cell types poorly represented on the manifold.** **A**, MEDAL hyperparameter tuning for t-SNE teachers on the neocortex atlas. Reconstruction loss was evaluated across t-SNE perplexities on train, validation, and test splits. The selected perplexity was 53. The corresponding training and test embeddings preserve major transcriptomic structure, and the per-point reconstruction-error maps highlight localized regions of higher distortion. **B**, Comparison with unselected t-SNE perplexities. A large perplexity (1241) produces a more globally smoothed embedding, whereas a small perplexity (5) produces sharper local subclusters on the training set but a more diffuse organization for held-out cells. These examples illustrate that visually detailed training embeddings do not necessarily preserve structure out of sample. **C**, Comparison across dimension-reduction teachers under the MEDAL validation protocol. Each method is shown at its selected hyperparameter, with validation reconstruction loss summarized across repeated distillations. t-SNE at perplexity 53 achieved the lowest held-out reconstruction loss among the methods considered, followed by UMAP, whereas spectral embedding and PCA retained less information in this setting. **D**, Pointwise distortion analysis for the selected t-SNE embedding. The left panel highlights broad annotated cell classes, including glutamatergic neurons, GABAergic neurons, non-neuronal cells, and endothelial cells. The right panel shows MEDAL per-point reconstruction mean squared error on the same embedding. High reconstruction error is concentrated disproportionately in non-neuronal and endothelial populations, suggesting that these smaller and transcriptionally distinct populations are less faithfully represented by the two-dimensional manifold.

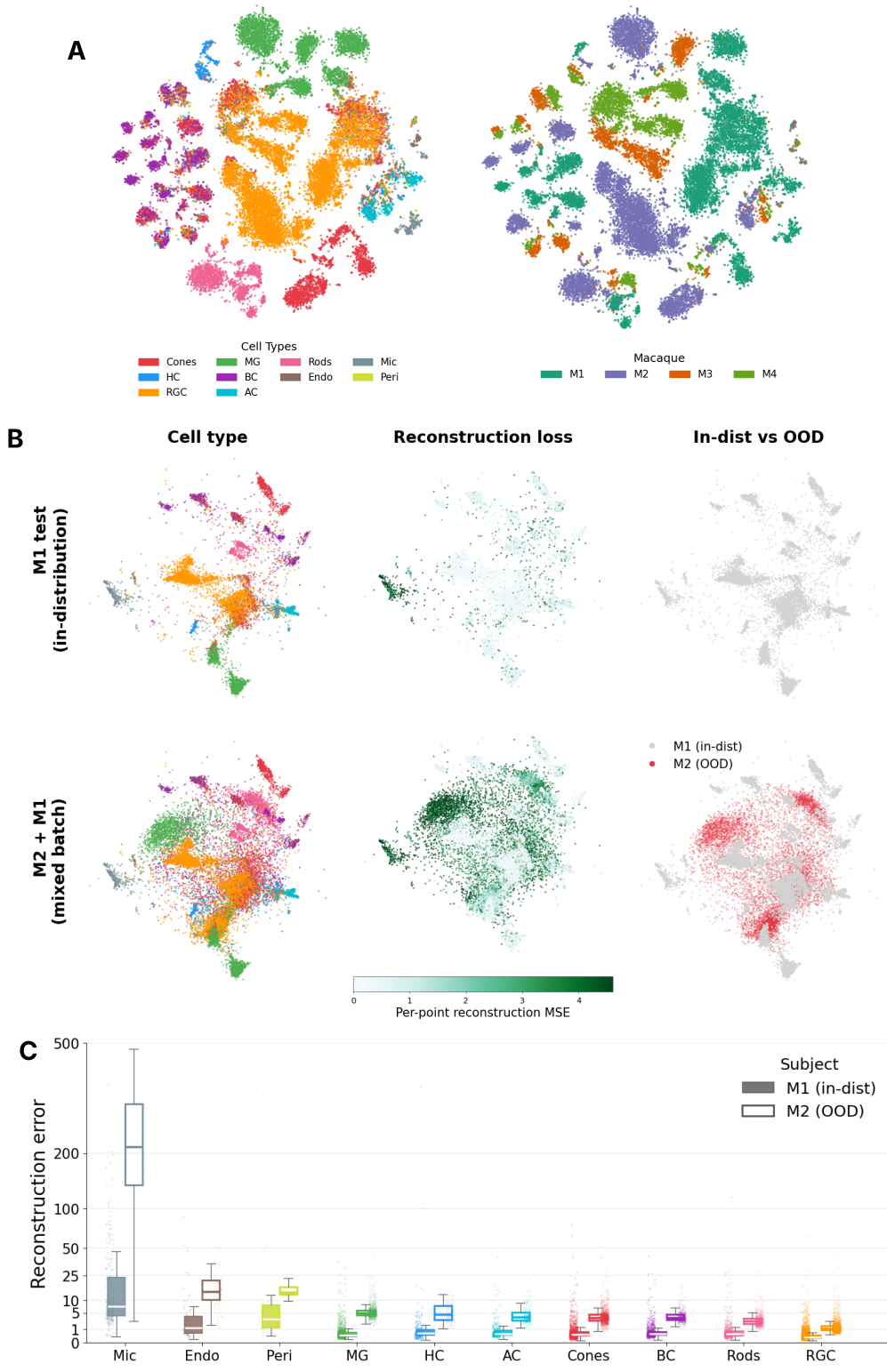


Figure 6

Figure 6: **MEDAL detects subject-level distribution shift in macaque retina single-cell RNA-seq ([81]) by embedding new cells into a fixed reference manifold.** **A**, Joint t-SNE embedding of macaque retinal cells from multiple subjects. The embedding appears organized by cell type when colored by annotated retinal cell class, but coloring the same embedding by subject reveals substantial subject-level structure, indicating that biological cell identity and inter-subject variation are entangled in the joint visualization. **B**, MEDAL reference mapping using M1 as the training distribution. MEDAL was trained on M1 training cells and used to embed either held-out M1 test cells or a mixed batch containing M1 test cells and M2 cells into the same M1 reference manifold. For the in-distribution M1 test batch, cells are placed coherently within the reference geometry and show low reconstruction error. In the mixed batch, M1 test cells remain aligned with the reference structure, whereas M2 cells occupy a displaced region of the embedding and exhibit elevated, spatially coherent reconstruction error. MEDAL therefore identifies out-of-distribution cells without using subject labels during embedding or scoring. **C**, Cell-type-specific reconstruction error for M1 test cells and M2 cells projected onto the M1 reference manifold. Reconstruction error is higher for M2 cells across multiple cell types, with the strongest shifts in microglia, endothelial cells, and pericytes. This indicates that the subject-level mismatch detected by MEDAL is not only global, but is concentrated in specific retinal cell populations.

References

- [1] Genevera I. Allen, Luqin Gan, and Lili Zheng. Interpretable machine learning for discovery: Statistical challenges and opportunities. *Annual Review of Statistics and Its Application*, 11 (Volume 11, 2024):97–121, 2024.
- [2] Bingxue An and Tiffany M. Tang. Consensus dimension reduction via multi-view learning, 2025. URL <https://arxiv.org/abs/2512.15802>.
- [3] Gabriel Appleby, Mateus Espadoto, Rui Chen, Samuel Goree, Alexandru Telea, Erik W Anderson, and Remco Chang. Hypernp: Interactive visual exploration of multidimensional projection hyperparameters, 2021. URL <https://arxiv.org/abs/2106.13777>.
- [4] Tal Ashuach, Danny A. Reidenbach, Adam Gayoso, and Nir Yosef. Multivi: Deep generative model for the integration of multimodal data. *Nature Methods*, 20:1222–1231, 2023. doi: 10.1038/s41592-023-01909-9.
- [5] Pierre Baldi and Kurt Hornik. Neural networks and principal component analysis: Learning from examples without local minima. *Neural Networks*, 2(1):53–58, 1989. ISSN 0893-6080. doi: [https://doi.org/10.1016/0893-6080\(89\)90014-2](https://doi.org/10.1016/0893-6080(89)90014-2). URL <https://www.sciencedirect.com/science/article/pii/0893608089900142>.
- [6] Andrew R. Barron. Universal approximation bounds for superpositions of a sigmoidal function. *IEEE Trans. Inf. Theory*, 39:930–945, 1993. URL <https://api.semanticscholar.org/CorpusID:15383918>.
- [7] Etienne Becht, Leland McInnes, John Healy, Charles-Antoine Dutertre, Immanuel W H Kwok, Lai Guan Ng, Florent Ginhoux, and Evan W Newell. Dimensionality reduction for visualizing single-cell data using umap. *Nature Biotechnology*, 37(1):38–44, 2019.
- [8] Mikhail Belkin and Partha Niyogi. Laplacian eigenmaps for dimensionality reduction and data representation. *Neural Computation*, 15(6):1373–1396, 2003. doi: 10.1162/089976603321780317.
- [9] Yoshua Bengio, Jean-françois Paiement, Pascal Vincent, Olivier Delalleau, Nicolas Roux, and Marie Ouimet. Out-of-sample extensions for lle, isomap, mds, eigenmaps, and spectral clustering. *Advances in neural information processing systems*, 16, 2003.
- [10] Yoshua Bengio, Aaron Courville, and Pascal Vincent. Representation learning: A review and new perspectives. *IEEE Transactions on Pattern Analysis and Machine Intelligence*, 35(8): 1798–1828, 2013. doi: 10.1109/TPAMI.2013.50.
- [11] Tommaso Biancalani, Gabriele Scalia, Lorenzo Buffoni, Rahul Avasthi, Ziqing Lu, Aviv Sanger, Nazli Tokcan, Charles R. Vanderburg, Åsa Segerstolpe, Meng Zhang, Inbal Avraham-Davidi, and Aviv Regev. Deep learning and alignment of spatially resolved single-cell transcriptomes with tangram. *Nature Methods*, 18(11):1352–1362, 2021. doi: 10.1038/s41592-021-01264-7.
- [12] Javier Blanco-Portals, Francesca Peiró, and Sònia Estradé. Strategies for eels data analysis. introducing umap and hdbscan for dimensionality reduction and clustering. *Microscopy and Microanalysis*, 28(1):109–122, 2022.

- [13] H. Bourlard and Y. Kamp. Auto-association by multilayer perceptrons and singular value decomposition. *Biological Cybernetics*, 59(4):291–294, 1988. doi: 10.1007/BF00332918. URL <https://doi.org/10.1007/BF00332918>.
- [14] Olivier Bousquet and André Elisseeff. Stability and generalization. *Journal of Machine Learning Research*, 2:499–526, 2002. doi: 10.1162/153244302760200704.
- [15] Pierre Boyeau, Jeremy Hong, Adam Gayoso, Michelle Kim, José L. McFaline-Figueroa, Michael I. Jordan, Elham Azizi, Can Ergen, and Nir Yosef. Deep generative modeling of sample-level heterogeneity in single-cell genomics. *Nature Methods*, 2025. doi: 10.1038/s41592-025-02808-x.
- [16] Leo Breiman, Jerome H. Friedman, Richard A. Olshen, and Charles J. Stone. *Classification and Regression Trees*. Wadsworth, Belmont, CA, 1984.
- [17] Yanshuai Cao and Luyu Wang. Automatic selection of t-sne perplexity, 2017. URL <https://arxiv.org/abs/1708.03229>.
- [18] Dylan Cashman, Mark Keller, Hyeon Jeon, Bum Chul Kwon, and Qianwen Wang. A critical analysis of the usage of dimensionality reduction in four domains. *IEEE Transactions on Visualization and Computer Graphics*, 31(10):9405–9423, October 2025. ISSN 2160-9306. doi: 10.1109/tvcg.2025.3567989. URL <http://dx.doi.org/10.1109/TVCG.2025.3567989>.
- [19] Raymond B. Cattell. The scree test for the number of factors. *Multivariate Behavioral Research*, 1(2):245–276, 1966. doi: 10.1207/s15327906mbr0102_10.
- [20] Andersen Chang, Tiffany M. Tang, Tarek M. Zikry, and Genevera I. Allen. Unsupervised machine learning for scientific discovery: Workflow and best practices, 2025. URL <https://arxiv.org/abs/2506.04553>.
- [21] Irene Chang, tzUNC, and Matthew Shen. Dataslingers/medal: v0.1.0, May 2026. URL <https://doi.org/10.5281/zenodo.20347573>.
- [22] Tara Chari and Lior Pachter. The specious art of single-cell genomics. *PLOS Computational Biology*, 19(8):1–20, 08 2023. doi: 10.1371/journal.pcbi.1011288. URL <https://doi.org/10.1371/journal.pcbi.1011288>.
- [23] Mark M Churchland, John P Cunningham, Matthew T Kaufman, Justin D Foster, Paul Nuyujukian, Stephen I Ryu, and Krishna V Shenoy. Neural population dynamics during reaching. *Nature*, 487(7405):51–56, 2012.
- [24] Haotian Cui, Chen Wang, Hassaan Maan, Kuan Pang, Feng Luo, and Bo Wang. scgpt: Toward building a foundation model for single-cell multi-omics using generative ai. *Nature Methods*, 21:1470–1480, 2024. doi: 10.1038/s41592-024-02201-0.
- [25] John P Cunningham and Byron M Yu. Dimensionality reduction for large-scale neural recordings. *Nature neuroscience*, 17(11):1500–1509, 2014.
- [26] George V. Cybenko. Approximation by superpositions of a sigmoidal function. *Mathematics of Control, Signals and Systems*, 2:303–314, 1989. URL <https://api.semanticscholar.org/CorpusID:3958369>.

- [27] Spyros Darmanis, Steven A. Sloan, Derek Croote, Marco Mignardi, Sophia Chernikova, Peyman Samghababi, Ye Zhang, Norma Neff, Mark Kowarsky, Christine Caneda, Gordon Li, Steven D. Chang, Ian David Connolly, Yingmei Li, Ben A. Barres, Melanie Hayden Gephart, and Stephen R. Quake. Single-cell rna-seq analysis of infiltrating neoplastic cells at the migrating front of human glioblastoma. *Cell Reports*, 21(5):1399–1410, 2017.
- [28] Lowell E. Davis. Histological and ultrastructural studies of the basal disk of hydra. iii. the gastrodermis and the mesoglea. *Cell and Tissue Research*, 162:107–118, 1975. doi: 10.1007/BF00223266.
- [29] Cyril de Bodt, Alex Diaz-Papkovich, Michael Bleher, Kerstin Bunte, Corinna Coupette, Sebastian Damrich, Enrique Fita Sanmartin, Fred A. Hamprecht, Emőke Ágnes Horvát, Dhruv Kohli, Smita Krishnaswamy, John A. Lee, Boudewijn P. F. Lelieveldt, Leland McInnes, Ian T. Nabney, Maximilian Noichl, Pavlin G. Poličar, Bastian Rieck, Guy Wolf, Gal Mishne, and Dmitry Kobak. Low-dimensional embeddings of high-dimensional data, 2025. URL <https://arxiv.org/abs/2508.15929>.
- [30] Kangning Dong and Shihua Zhang. Deciphering spatial domains from spatially resolved transcriptomics with an adaptive graph attention auto-encoder. *Nature Communications*, 13(1):1739, 2022. doi: 10.1038/s41467-022-29439-6.
- [31] Michael W. Dorrity, Lauren M. Saunders, Christine Queitsch, Stanley Fields, and Cole Trapnell. Dimensionality reduction by umap to visualize physical and genetic interactions. *Nature Communications*, 11(1):1537, 2020. doi: 10.1038/s41467-020-15351-4. URL <https://doi.org/10.1038/s41467-020-15351-4>.
- [32] Andres F. Duque, Sacha Morin, Guy Wolf, and Kevin Moon. Extendable and invertible manifold learning with geometry regularized autoencoders. In *2020 IEEE International Conference on Big Data (Big Data)*, page 5027–5036. IEEE, December 2020. doi: 10.1109/bigdata50022.2020.9378049. URL <http://dx.doi.org/10.1109/BigData50022.2020.9378049>.
- [33] Samuele Fiorini. gene expression cancer RNA-Seq. UCI Machine Learning Repository, 2016. DOI: <https://doi.org/10.24432/C5R88H>.
- [34] Sotiria Fotopoulou. A review of unsupervised learning in astronomy. *Astronomy and Computing*, 48:100851, 2024.
- [35] Luqin Gan, Tarek M Zikry, and Genevera I Allen. Are machine learning interpretations reliable? a stability study on global interpretations. *arXiv preprint arXiv:2505.15728*, 2025.
- [36] Adam Gayoso, Zoë Steier, Romain Lopez, Jeffrey Regier, Kristopher L. Nazor, Aaron Streets, and Nir Yosef. Joint probabilistic modeling of single-cell multi-omic data with totalvi. *Nature Methods*, 18(3):272–282, 2021. doi: 10.1038/s41592-020-01050-x.
- [37] Rufus Gikera, Elizaphan Maina, Shadrack Maina Mambo, and Jonathan Mwaura. K-hyperparameter tuning in high-dimensional genomics using joint optimization of deep differential evolutionary algorithm and unsupervised transfer learning from intelligent genoumap embeddings. *International Journal of Information Technology*, 17(3):1679–1701, 2025.
- [38] Ingo Gühring, Mones Raslan, and Gitta Kutyniok. Expressivity of deep neural networks, 2020. URL <https://arxiv.org/abs/2007.04759>.

- [39] Laleh Haghverdi, Aaron T. L. Lun, Michael D. Morgan, and John C. Marioni. Batch effects in single-cell rna-sequencing data are corrected by matching mutual nearest neighbors. *Nature Biotechnology*, 36:421–427, 2018. doi: 10.1038/nbt.4091.
- [40] Boris Hanin and Mark Sellke. Approximating continuous functions by relu nets of minimal width, 2018. URL <https://arxiv.org/abs/1710.11278>.
- [41] Yuhan Hao, Stephanie Hao, Erica Andersen-Nissen, William M. Mauck III, Shiwei Zheng, Andrew Butler, Maddie J. Lee, Aaron J. Wilk, Charlotte Darby, Michael Zager, et al. Integrated analysis of multimodal single-cell data. *Cell*, 184(13):3573–3587.e29, 2021. doi: 10.1016/j.cell.2021.04.048.
- [42] Euxhen Hasanaaj, Jingtao Wang, Arjun Sarathi, Jun Ding, and Ziv Bar-Joseph. Interactive single-cell data analysis using cellar. *Nature Communications*, 13(1):1998, 2022.
- [43] Geoffrey Hinton, Oriol Vinyals, and Jeff Dean. Distilling the knowledge in a neural network, 2015. URL <https://arxiv.org/abs/1503.02531>.
- [44] Geoffrey E. Hinton and Richard S. Zemel. Autoencoders, minimum description length and helmholtz free energy. In Jack D. Cowan, Gerald Tesauro, and Joshua Alspector, editors, *Advances in Neural Information Processing Systems 6*, pages 3–10. Morgan Kaufmann, 1994.
- [45] Thomas W. Holstein. The hydra stem cell system – revisited. *Cells & Development*, 174: 203846, 2023. doi: 10.1016/j.cdev.2023.203846.
- [46] Kurt Hornik. Approximation capabilities of multilayer feedforward networks. *Neural Networks*, 4(2):251–257, 1991.
- [47] Kurt Hornik, Maxwell Stinchcombe, and Halbert White. Multilayer feedforward networks are universal approximators. *Neural Networks*, 2(5):359–366, 1989.
- [48] Harold Hotelling. Analysis of a complex of statistical variables into principal components. *Journal of educational psychology*, 24(6):417, 1933.
- [49] Haiyang Huang, Yingfan Wang, Cynthia Rudin, and Edward P. Browne. Towards a comprehensive evaluation of dimension reduction methods for transcriptomic data visualization. *Communications Biology*, 5(1):719, 2022. doi: 10.1038/s42003-022-03628-x. URL <https://doi.org/10.1038/s42003-022-03628-x>.
- [50] Hyeon Jeon, Jeongin Park, Sungbok Shin, and Jinwook Seo. Stop misusing t-sne and umap for visual analytics, 2025. URL <https://arxiv.org/abs/2506.08725>.
- [51] Eric M Johnson, William Kath, and Madhav Mani. Embedr: distinguishing signal from noise in single-cell omics data. *Patterns*, 3(3), 2022.
- [52] Abderrahmane Jouilili, Hajar Hantouti, and Rajae E L Ouazzani. Optimizing dimensionality reduction in sdn: A metaheuristic approach of umap parameter tuning. In *2024 5th International Conference on Communications, Information, Electronic and Energy Systems (CIEES)*, pages 1–6, 2024. doi: 10.1109/CIEES62939.2024.10811181.
- [53] Joyce B. Kang, Aparna Nathan, Kathryn Weinand, Fan Zhang, Nghia Millard, Laurie Rumker, D. Branch Moody, Ilya Korsunsky, and Soumya Raychaudhuri. Efficient and precise single-cell reference atlas mapping with symphony. *Nature Communications*, 12(1):5890, 2021. doi: 10.1038/s41467-021-25957-x.

- [54] Günter Klambauer, Thomas Unterthiner, Andreas Mayr, and Sepp Hochreiter. Self-normalizing neural networks, 2017. URL <https://arxiv.org/abs/1706.02515>.
- [55] Vitalii Kleshchevnikov, Artem Shmatko, Emma Dann, Alexander Aivazidis, Hamish W. King, Tong Li, Rasa Elmentaite, Artem Lomakin, Veronika Kedlian, Adam Gayoso, Mika Sarkin Jain, Jun Sung Park, Lauma Ramona, Elizabeth Tuck, Anna Arutyunyan, Roser Vento-Tormo, Moritz Gerstung, Louisa James, Oliver Stegle, and Omer Ali Bayraktar. Cell2location maps fine-grained cell types in spatial transcriptomics. *Nature Biotechnology*, 40:661–671, 2022. doi: 10.1038/s41587-021-01139-4.
- [56] Dmitry Kobak and Philipp Berens. The art of using t-sne for single-cell transcriptomics. *Nature communications*, 10(1):5416, 2019.
- [57] Dmitry Kobak and George C. Linderman. Initialization is critical for preserving global data structure in both t-sne and umap. *Nature Biotechnology*, 39(2):156–157, 2021. doi: 10.1038/s41587-020-00809-z.
- [58] Ilya Korsunsky, Nghia Millard, Jean Fan, Kamil Slowikowski, Fan Zhang, Kevin Wei, Yuriy Baglaenko, Michael Brenner, Po-Ru Loh, and Soumya Raychaudhuri. Fast, sensitive and accurate integration of single-cell data with harmony. *Nature Methods*, 16(12):1289–1296, 2019. doi: 10.1038/s41592-019-0619-0.
- [59] Yann LeCun, Léon Bottou, Yoshua Bengio, and Patrick Haffner. Gradient-based learning applied to document recognition. *Proceedings of the IEEE*, 86(11):2278–2324, 1998. doi: 10.1109/5.726791.
- [60] John A. Lee and Michel Verleysen. Quality assessment of dimensionality reduction: Rank-based criteria. *Neurocomputing*, 72(7–9):1431–1443, 2009. doi: 10.1016/j.neucom.2008.12.017.
- [61] Moshe Leshno, Vladimir Ya. Lin, Allan Pinkus, and Shimon Schocken. Multilayer feedforward networks with a nonpolynomial activation function can approximate any function. *Neural Networks*, 6(6):861–867, 1993.
- [62] Yin-Ting Liao, Hengrui Luo, and Anna Ma. Efficient and robust bayesian selection of hyperparameters in dimension reduction for visualization, 2023. URL <https://arxiv.org/abs/2306.00357>.
- [63] Justin Lin and Julia Fukuyama. Calibrating dimension reduction hyperparameters in the presence of noise. *PLOS Computational Biology*, 20(9):e1012427, September 2024. ISSN 1553-7358. doi: 10.1371/journal.pcbi.1012427. URL <http://dx.doi.org/10.1371/journal.pcbi.1012427>.
- [64] Zhexuan Liu, Rong Ma, and Yiqiao Zhong. Assessing and improving reliability of neighbor embedding methods: a map-continuity perspective, 2025. URL <https://arxiv.org/abs/2410.16608>.
- [65] Romain Lopez, Jeffrey Regier, Michael B. Cole, Michael I. Jordan, and Nir Yosef. Deep generative modeling for single-cell transcriptomics. *Nature Methods*, 15(12):1053–1058, 2018. doi: 10.1038/s41592-018-0229-2.
- [66] Mohammad Lotfollahi, F. Alexander Wolf, and Fabian J. Theis. scgen predicts single-cell perturbation responses. *Nature Methods*, 16:715–721, 2019. doi: 10.1038/s41592-019-0494-8.

- [67] Mohammad Lotfollahi, Mohsen Naghipourfar, Malte D. Luecken, Matin Khajavi, Maren Büttner, Marco Wagenstetter, Žiga Avsec, Adam Gayoso, Nir Yosef, Marta Interlandi, Sergei Rybakov, Alexander V. Misharin, and Fabian J. Theis. Mapping single-cell data to reference atlases by transfer learning. *Nature Biotechnology*, 40(1):121–130, 2022. doi: 10.1038/s41587-021-01001-7.
- [68] Mohammad Lotfollahi, Anna Klimovskaia Susmelj, Carlo De Donno, Yuge Ji, Ignacio L. Ibarra, Sanjay R. Srivatsan, Mohsen Naghipourfar, Riza M. Daza, Beth Martin, F. Alexander Wolf, Nailya Yakubova, Jay Shendure Lee, José L. McFaline-Figueroa, and Fabian J. Theis. Predicting cellular responses to complex perturbations in high-throughput screens. *Molecular Systems Biology*, 19(6):e11517, 2023. doi: 10.15252/msb.202211517.
- [69] Zhou Lu, Hongming Pu, Feicheng Wang, Zhiqiang Hu, and Liwei Wang. The expressive power of neural networks: A view from the width, 2017. URL <https://arxiv.org/abs/1709.02540>.
- [70] Dalton Lunga, Saurabh Prasad, Melba M Crawford, and Okan Ersoy. Manifold-learning-based feature extraction for classification of hyperspectral data: A review of advances in manifold learning. *IEEE Signal Processing Magazine*, 31(1):55–66, 2013.
- [71] Leland McInnes, John Healy, Nathaniel Saul, and Lukas Grossberger. Umap: Uniform manifold approximation and projection. *Journal of Open Source Software*, 3(29):861, 2018. doi: 10.21105/joss.00861. URL <https://doi.org/10.21105/joss.00861>.
- [72] Leland McInnes, John Healy, and James Melville. Umap: Uniform manifold approximation and projection for dimension reduction, 2020. URL <https://arxiv.org/abs/1802.03426>.
- [73] Marina Meilä and Hanyu Zhang. Manifold learning: What, how, and why. *Annual Review of Statistics and Its Application*, 11:27–57, 2024. doi: 10.1146/annurev-statistics-112723-034552. URL <https://arxiv.org/abs/2311.03757>.
- [74] Lieke Michielsen, Mohammad Lotfollahi, Daniela C. Strobl, Lisa Sikkema, Marcel J. T. Reinders, Fabian J. Theis, and Ahmed Mahfouz. Single-cell reference mapping to construct and extend cell-type hierarchies. *NAR Genomics and Bioinformatics*, 5(3):lqad070, 2023. doi: 10.1093/nargab/lqad070.
- [75] Kevin R. Moon, Jay S. Stanley, Daniel Burkhardt, David van Dijk, Guy Wolf, and Smita Krishnaswamy. Manifold learning-based methods for analyzing single-cell rna-sequencing data. *Current Opinion in Systems Biology*, 7:36–46, 2018. ISSN 2452-3100. doi: <https://doi.org/10.1016/j.coisb.2017.12.008>. URL <https://www.sciencedirect.com/science/article/pii/S2452310017301877>. * Future of systems biology* Genomics and epigenomics.
- [76] Kevin R Moon, David Van Dijk, Zheng Wang, Scott Gigante, Daniel B Burkhardt, William S Chen, Kristina Yim, Antonia van den Elzen, Matthew J Hirn, Ronald R Coifman, et al. Visualizing structure and transitions in high-dimensional biological data. *Nature biotechnology*, 37(12):1482–1492, 2019.
- [77] Vinod Nair and Geoffrey E. Hinton. Rectified linear units improve restricted boltzmann machines. In *Proceedings of the 27th International Conference on Machine Learning*, pages 807–814, 2010.

- [78] Imran Nasim and Melanie Weber. Automated manifold learning for reduced order modeling, 2025. URL <https://arxiv.org/abs/2506.01741>.
- [79] National Academies of Sciences, Medicine, Policy, Global Affairs, Board on Research Data, Information, Division on Engineering, Physical Sciences, Committee on Applied, Theoretical Statistics, et al. *Reproducibility and replicability in science*. National Academies Press, 2019.
- [80] Alexey A Orlov, Tagir N Akhmetshin, Dragos Horvath, Gilles Marcou, and Alexandre Varnek. From high dimensions to human insight: exploring dimensionality reduction for chemical space visualization. *Molecular Informatics*, 44(1):e202400265, 2025.
- [81] Yi-Rong Peng, Karthik Shekhar, Wenjun Yan, Dustin Herrmann, Anna Sappington, Gregory S. Bryman, Tavé van Zyl, Michael Tri. H. Do, Aviv Regev, and Joshua R. Sanes. Molecular classification and comparative taxonomics of foveal and peripheral cells in primate retina. *Cell*, 176(5):1222–1237.e22, 2019.
- [82] Elad Plaut. From principal subspaces to principal components with linear autoencoders, 2018. URL <https://arxiv.org/abs/1804.10253>.
- [83] C. Allende Prieto, S.R. Majewski, R. Schiavon, K. Cunha, P. Frinchaboy, J. Holtzman, K. Johnston, M. Shetrone, M. Skrutskie, V. Smith, and J. Wilson. Apogee: The apache point observatory galactic evolution experiment. *Astronomische Nachrichten*, 329(9-10):1018–1021, 2008. doi: <https://doi.org/10.1002/asna.200811080>. URL <https://onlinelibrary.wiley.com/doi/abs/10.1002/asna.200811080>.
- [84] M. S. Rosito, L. A. Bignone, P. B. Tissera, and S. E. Pedrosa. Application of dimensionality reduction and clustering algorithms for the classification of kinematic morphologies of galaxies. *Astronomy & Astrophysics*, 671:A19, 2023. doi: 10.1051/0004-6361/202244707. URL <https://doi.org/10.1051/0004-6361/202244707>.
- [85] Sam T Roweis and Lawrence K Saul. Nonlinear dimensionality reduction by locally linear embedding. *science*, 290(5500):2323–2326, 2000.
- [86] Tim Sainburg, Leland McInnes, and Timothy Q Gentner. Parametric umap embeddings for representation and semisupervised learning. *Neural Computation*, 33(11):2881–2907, 2021.
- [87] Stefan Siebert, Jeffrey A. Farrell, Jack F. Cazes, Yashodara Abeykoon, Abby S. Primack, Christine E. Schnitzler, and Celina E. Juliano. Stem cell differentiation trajectories in *iijhydra*/*ij* resolved at single-cell resolution. *Science*, 365(6451):eaav9314, 2019.
- [88] Tim Stuart, Andrew Butler, Paul Hoffman, Christoph Hafemeister, Efthymia Papalexi, William M. Mauck, Yuhan Hao, Marlon Stoeckius, Peter Smibert, and Rahul Satija. Comprehensive integration of single-cell data. *Cell*, 177(7):1888–1902.e21, 2019. doi: 10.1016/j.cell.2019.05.031.
- [89] Eric D. Sun, Rong Ma, and James Zou. Dynamic visualization of high-dimensional data. *Nature Computational Science*, 3(1):86–100, 2023. doi: 10.1038/s43588-022-00380-4. URL <https://doi.org/10.1038/s43588-022-00380-4>.
- [90] Tiffany Tang. Dataslingers/unsupervised-workflow-astro: v1.0 code for unsupervised machine learning for scientific discovery: Workflow and best practices, March 2026. URL <https://doi.org/10.5281/zenodo.19194851>.

- [91] Bosiljka Tasic, Zizhen Yao, Lucas T Graybuck, Kimberly A Smith, Thuc Nghi Nguyen, Darren Bertagnolli, Jeff Goldy, Emma Garren, Michael N Economo, Sarada Viswanathan, et al. Shared and distinct transcriptomic cell types across neocortical areas. *Nature*, 563(7729):72–78, 2018.
- [92] Joshua B Tenenbaum, Vin de Silva, and John C Langford. A global geometric framework for nonlinear dimensionality reduction. *Ann. NY Acad. Sci*, 911:418, 2000.
- [93] Christina V. Theodoris, Ling Xiao, Adit Chopra, Mark D. Chaffin, Zeina R. Al Sayed, Matthew C. Hill, Hannah Mantineo, Euan M. Brydon, Zhijian Zeng, X. Shirley Liu, and Patrick T. Ellinor. Transfer learning enables predictions in network biology. *Nature*, 618:616–624, 2023. doi: 10.1038/s41586-023-06139-9.
- [94] F. William Townes, Stephanie C. Hicks, Martin J. Aryee, and Rafael A. Irizarry. Feature selection and dimension reduction for single-cell rna-seq based on a multinomial model. *Genome Biology*, 20(1):295, 2019. doi: 10.1186/s13059-019-1861-6.
- [95] Hoa Thi Nhu Tran, Kok Siong Ang, Marion Chevrier, Xiaomeng Zhang, Nicole Yee Shin Lee, Michelle Goh, and Jinmiao Chen. A benchmark of batch-effect correction methods for single-cell rna sequencing data. *Genome Biology*, 21(1):12, 2020. doi: 10.1186/s13059-019-1850-9.
- [96] Michael Tschannen, Olivier Bachem, and Mario Lucic. Recent advances in autoencoder-based representation learning. *arXiv preprint arXiv:1812.05069*, 2018.
- [97] Laurens Van Der Maaten. Learning a parametric embedding by preserving local structure. In *Artificial intelligence and statistics*, pages 384–391. PMLR, 2009.
- [98] Laurens Van der Maaten and Geoffrey Hinton. Visualizing data using t-sne. *Journal of machine learning research*, 9(11), 2008.
- [99] Ashish Vaswani, Noam Shazeer, Niki Parmar, Jakob Uszkoreit, Llion Jones, Aidan N. Gomez, Lukasz Kaiser, and Illia Polosukhin. Attention is all you need. In *Advances in Neural Information Processing Systems*, volume 30, pages 5998–6008, 2017.
- [100] Jarkko Venna and Samuel Kaski. Local multidimensional scaling. *Neural Networks*, 19(6–7):889–899, 2006. doi: 10.1016/j.neunet.2006.05.014.
- [101] Viet Minh Vu, Adrien Bibal, and Benoît Frénay. Constraint preserving score for automatic hyperparameter tuning of dimensionality reduction methods for visualization. *IEEE Transactions on Artificial Intelligence*, 2(3):269–282, 2021. doi: 10.1109/TAI.2021.3094774.
- [102] Yingfan Wang, Haiyang Huang, Cynthia Rudin, and Yaron Shaposhnik. Understanding how dimension reduction tools work: An empirical approach to deciphering t-sne, umap, trimap, and pacmap for data visualization, 2021. URL <https://arxiv.org/abs/2012.04456>.
- [103] Lucy Xia, Christy Lee, and Jingyi Jessica Li. Statistical method scdeed for detecting dubious 2d single-cell embeddings and optimizing t-sne and umap hyperparameters. *Nature Communications*, 15(1):1753, 2024.
- [104] Fan Yang, Wenchuan Wang, Fang Wang, Yuan Fang, Duyu Tang, Junzhou Huang, Hui Lu, and Jianhua Yao. scbert as a large-scale pretrained deep language model for cell type annotation of single-cell rna-seq data. *Nature Machine Intelligence*, 4(10):852–866, 2022. doi: 10.1038/s42256-022-00534-z.

- [105] Dmitry Yarotsky. Error bounds for approximations with deep relu networks. *Neural Networks*, 94:103–114, 2017.
- [106] Chulhee Yun, Suvrit Sra, and Ali Jadbabaie. Small relu networks are powerful memorizers: a tight analysis of memorization capacity, 2019. URL <https://arxiv.org/abs/1810.07770>.
- [107] Chiyuan Zhang, Samy Bengio, Moritz Hardt, Benjamin Recht, and Oriol Vinyals. Understanding deep learning requires rethinking generalization, 2017. URL <https://arxiv.org/abs/1611.03530>.
- [108] Guiyong Zhang, Zihao Wang, Rongbing Mei, Tiezhi Sun, Huakun Huang, Zhe Sun, and Zhifan Zhang. A comprehensive evaluation of dimensionality reduction techniques in fluid dynamics. *Physics of Fluids*, 37(11), 2025.
- [109] Tarek M Zikry and Genevera I Allen. Limeade: Local interpretable manifold explanations for dimension evaluations. In *ICLR 2025 Workshop on Machine Learning for Genomics Explorations*, 2025.
- [110] Tarek M Zikry, Samuel C Wolff, Jolene S Ranek, Harris M Davis, Ander Naugle, Namit Luthra, Austin A Whitman, Katarzyna M Kedziora, Wayne Stallaert, Michael R Kosorok, et al. Cell cycle plasticity underlies fractional resistance to palbociclib in er+/her2- breast tumor cells. *Proceedings of the National Academy of Sciences*, 121(7):e2309261121, 2024.

S1 Datasets

MNIST The MNIST dataset consists of grayscale images of handwritten digits (0–9). For this study, we use a subset of 10,000 images, each with spatial resolution 28×28 . Images are flattened into 784-dimensional feature vectors, and pixel intensities are normalized to lie in $[0, 1]$. MNIST serves as a low-dimensional, low-noise benchmark for evaluating representation learning methods under controlled conditions.

Hydra The Hydra single-cell RNA-seq dataset represents the first comprehensive cell atlas of the adult Hydra polyp [87, 103]. The dataset contains transcriptomes from $n = 25,052$ cells profiled using Drop-seq, with expression measurements for 33,391 genes. Data are processed, normalized, and scaled using the Seurat pipeline, and curated cluster annotations are provided. To reduce computational burden and facilitate overparameterized representation learning and distillation, we project the data onto the top 500 principal components (PCs), which capture the dominant biological variation while substantially reducing dimensionality.

Neocortex This dataset comprises single-cell transcriptomic profiles of the adult mouse neocortex, as described by [91]. It includes approximately 23,822 cells sampled from the primary visual cortex (VISp) and anterior lateral motor cortex (ALM). Expression data are processed and scaled using Seurat, with cell-type annotations provided. The dataset captures a rich diversity of neuronal and non-neuronal populations, including glutamatergic neurons, GABAergic neurons, and multiple glial cell types. To manage computational complexity and enable overparameterized modeling, we retain the top 1,000 principal components (PCs), preserving major transcriptional structure while reducing dimensionality.

Macaque The Macaque dataset is a single-cell transcriptomic atlas of the primate retina, profiling both foveal and peripheral regions of *Macaca mulatta*, as described by [81]. The dataset comprises approximately 48,000 cells collected across a total of three individual macaques, providing a molecular characterization of all major retinal cell classes, including photoreceptors (rods and cones), bipolar cells (BC), horizontal cells (HC), amacrine cells (AC), retinal ganglion cells (RGC), and Müller glia (MG). The presence of multiple biological donors introduces natural inter-individual variability, enabling evaluation of our framework’s ability to capture and generalize across domain shifts arising from subject-specific transcriptional differences.

Darmanis The Darmanis dataset is a single-cell RNA-seq dataset profiling the adult human brain, as described by [27]. It comprises transcriptomic measurements from thousands of individual cells sampled across multiple brain regions, including the cerebral cortex, hippocampus, and other areas. The dataset captures a diverse range of major neural and non-neural cell types, including neurons, astrocytes, oligodendrocytes, microglia, and endothelial cells, with expression profiles reflecting both cell-type identity and regional heterogeneity. As a high-dimensional, noise-rich biological dataset with complex cellular composition, the Darmanis dataset provides a challenging benchmark for representation learning and manifold-based methods, particularly for evaluating robustness to biological variability and subtle cell-type-specific transcriptional programs.

PANCAN [33] The PANCAN dataset used in this study is a bulk RNA-sequencing dataset derived from The Cancer Genome Atlas (TCGA) pan-cancer project, which profiled trans-criptome-wide gene expression across multiple tumor types as part of a large effort to characterize molecular aberrations across cancers. The subset accessed via the UCI Machine Learning Repository consists of 801 tumor samples spanning multiple cancer types—including breast invasive carcinoma (BRCA), kidney renal cell carcinoma (KIRC), colon adenocarcinoma (COAD), lung adenocarcinoma (LUAD), and prostate adenocarcinoma (PRAD)**—with no missing values. Each sample is represented by 20,531 gene expression features measured on the Illumina HiSeq platform, corresponding to real-valued normalized RNA-Seq counts for individual genes. This results in a wide data matrix (many more features than samples) typical of transcriptomic datasets, with high dimensionality and biological heterogeneity that pose substantial challenges for representation learning, overfitting control, and generalization in downstream modeling. Because of these characteristics, PANCAN serves as a demanding benchmark for evaluating dimensionality reduction and autoencoder architectures in the presence of complex, noise-rich biological signals.

APOGEE This astronomical dataset consists of approximately 8,000 stellar spectra, each represented by flux measurements across 19 wavelength bands [83]. The data and preprocessing pipeline follow the methodology described in [20]. This dataset provides a structured, low-dimensional scientific benchmark with continuous-valued features, enabling evaluation of representation learning methods in a physical sciences context.

General preprocessing pipeline Each dataset in use is partitioned into a training set (80%) and a test set (20%) to evaluate the model’s ability to generalize to unseen data point.

S2 Methods

This supplement provides additional methodological details for MEDAL. The main text introduces MEDAL as a constrained autoencoder framework that distills a fitted teacher embedding into a reusable parametric model. Here we expand on four points that are central to the method: (i) the practical operating regime in which near-zero empirical distillation is achieved, (ii) why such alignment is feasible in principle, (iii) why reconstruction remains meaningful after enforcing distillation, and (iv) the held-out evaluation protocol used for hyperparameter selection and method comparison.

S2.1 Practical operating regime for near-zero distillation

A central practical question for MEDAL is how to train the student so that empirical distillation loss is driven to near zero while reconstruction remains useful. In our experiments, this operating regime is determined primarily by the distillation weight λ_d , the student architecture, the encoder activation design, and an adaptive optimization schedule.

λ_d analysis. The distillation weight in Equation 2 is the primary control governing the near-zero-distillation regime. Empirically, increasing λ_d reduces the final distillation loss by orders of magnitude, while reconstruction error increases comparatively modestly (Supplementary Figure S1).

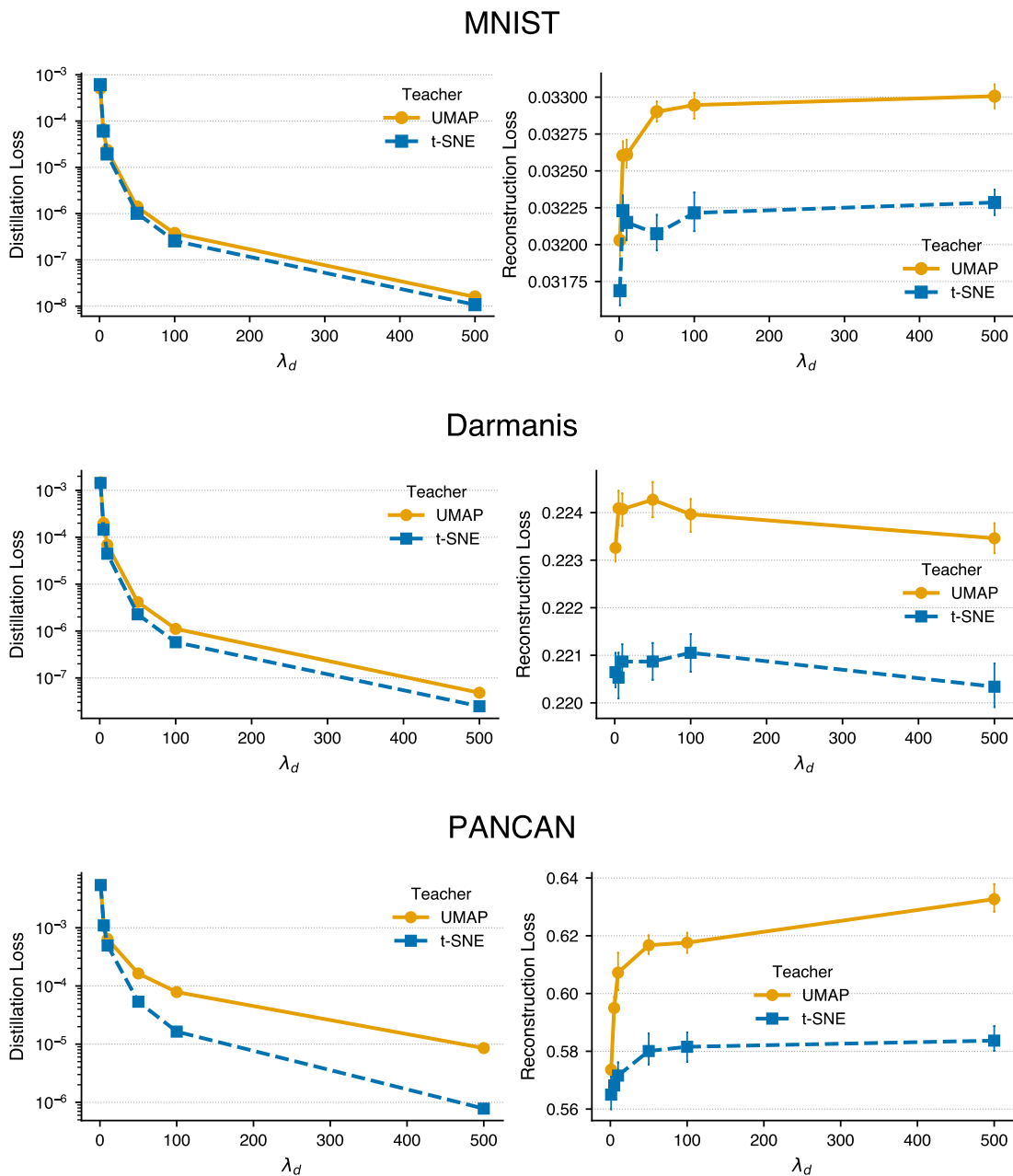


Figure S1: **Effect of the distillation weight λ_d on teacher matching and reconstruction.** Final distillation loss and reconstruction loss are shown across increasing values of λ_d for MNIST, Darmanis, and PANCAN. Larger values of λ_d place greater weight on matching the teacher embedding in Equation 2. Across datasets, increasing λ_d drives the distillation loss down by orders of magnitude, often into the near-zero regime, while reconstruction loss increases only modestly. This tradeoff motivates the operating principle used throughout MEDAL: choose λ_d large enough to achieve faithful teacher recovery, then compare teacher settings using reconstruction loss only among successfully distilled runs.

Operationally, this makes the choice straightforward: we prioritize faithful teacher matching and accept a small reconstruction penalty in exchange.

Architecture capacity: depth and width. In practice, MEDAL does not require extremely deep or extremely wide networks. Across datasets with very different sample sizes and input dimensions, moderate multilayer perceptron encoder–decoder architectures were sufficient to achieve near-zero empirical distillation. To give practical guidance on architecture selection, we study how depth and width affect both distillation and reconstruction.

For a symmetric autoencoder with L hidden layers per side, constant width w , input dimension D , and latent dimension z , the total parameter count (ignoring biases) is

$$P(L, w) = 2(L - 1)w^2 + 2(D + z)w. \tag{3}$$

For the depth analysis, we fix a reference parameter budget $P^* = P(L_{\text{ref}}, w_{\text{ref}})$ with $L_{\text{ref}} = 3$ and $w_{\text{ref}} = 256$, and solve for the width that preserves this budget at each target depth:

$$w(L) = \frac{-(D + z) + \sqrt{(D + z)^2 + 2(L - 1)P^*}}{2(L - 1)}.$$

All other training choices are held fixed across depths. The resulting width–depth pairs are listed in [Supplementary Table S1](#), and the empirical results are shown in [Supplementary Figure S2](#).

Dataset	D	$w(L=2)$	$w(L=3)$	$w(L=4)$	$w(L=6)$	$w(L=8)$
MNIST	784	305	256	227	191	169
PANCAN	20531	260	256	253	247	242
Darmanis	500	317	256	222	183	160

Table S1: Parameter-matched width–depth pairs. Reference architecture: $L_{\text{ref}} = 3$, $w_{\text{ref}} = 256$, $z = 2$.

The central finding is that near-zero distillation does *not* require deep networks. Across datasets and teacher types, distillation loss is already at or near machine precision with relatively shallow architectures, and increasing depth beyond this point provides little systematic benefit. Under a fixed parameter budget, deeper models also reduce per-layer width, which can make optimization less efficient and increase training time without improving final alignment. Reconstruction shows a somewhat more nuanced dependence on depth, but the main practical conclusion is that moderate depth is sufficient for MEDAL’s distillation objective.

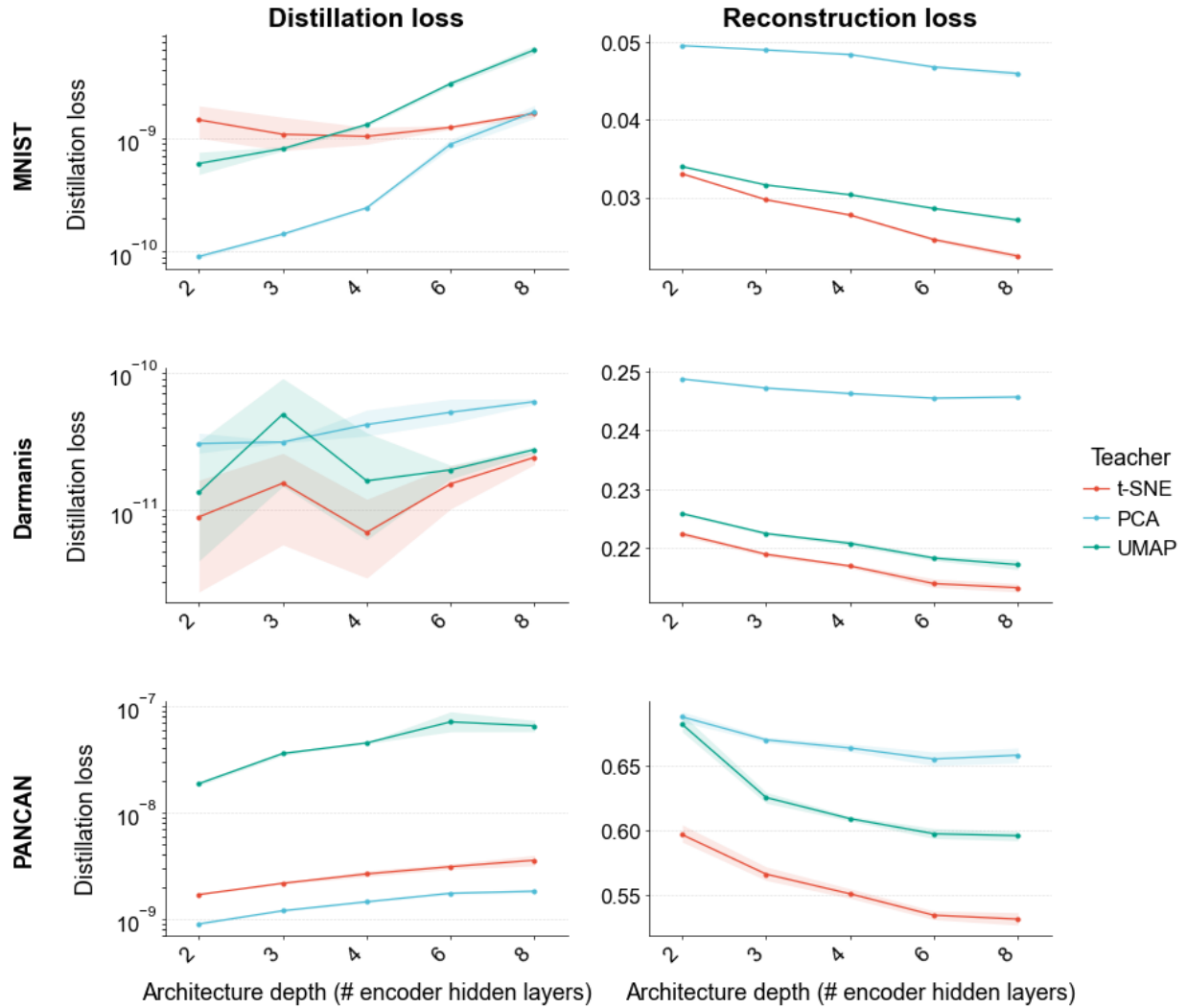


Figure S2: **Effect of architecture depth on distillation and reconstruction loss under a fixed parameter budget.** Each line shows the mean \pm 95% CI across 20 random seeds. (*Left*) Distillation loss on a log scale. (*Right*) Reconstruction loss. Rows correspond to three datasets; colors denote teacher type. Width at each depth is adjusted to preserve a fixed total parameter count (see [Supplementary Table S1](#)).

Per-layer width analysis. Complementing the depth study, we analyze the effect of model size by fixing the number of hidden layers L and varying the per-layer width w , shared across layers. This directly changes the total parameter count in [Equation 3](#) while holding all other factors fixed: data splits and preprocessing, teacher embedding, loss weights, initialization, optimizer, batch size, and optimization budget. Results are shown in [Supplementary Figure S3](#).

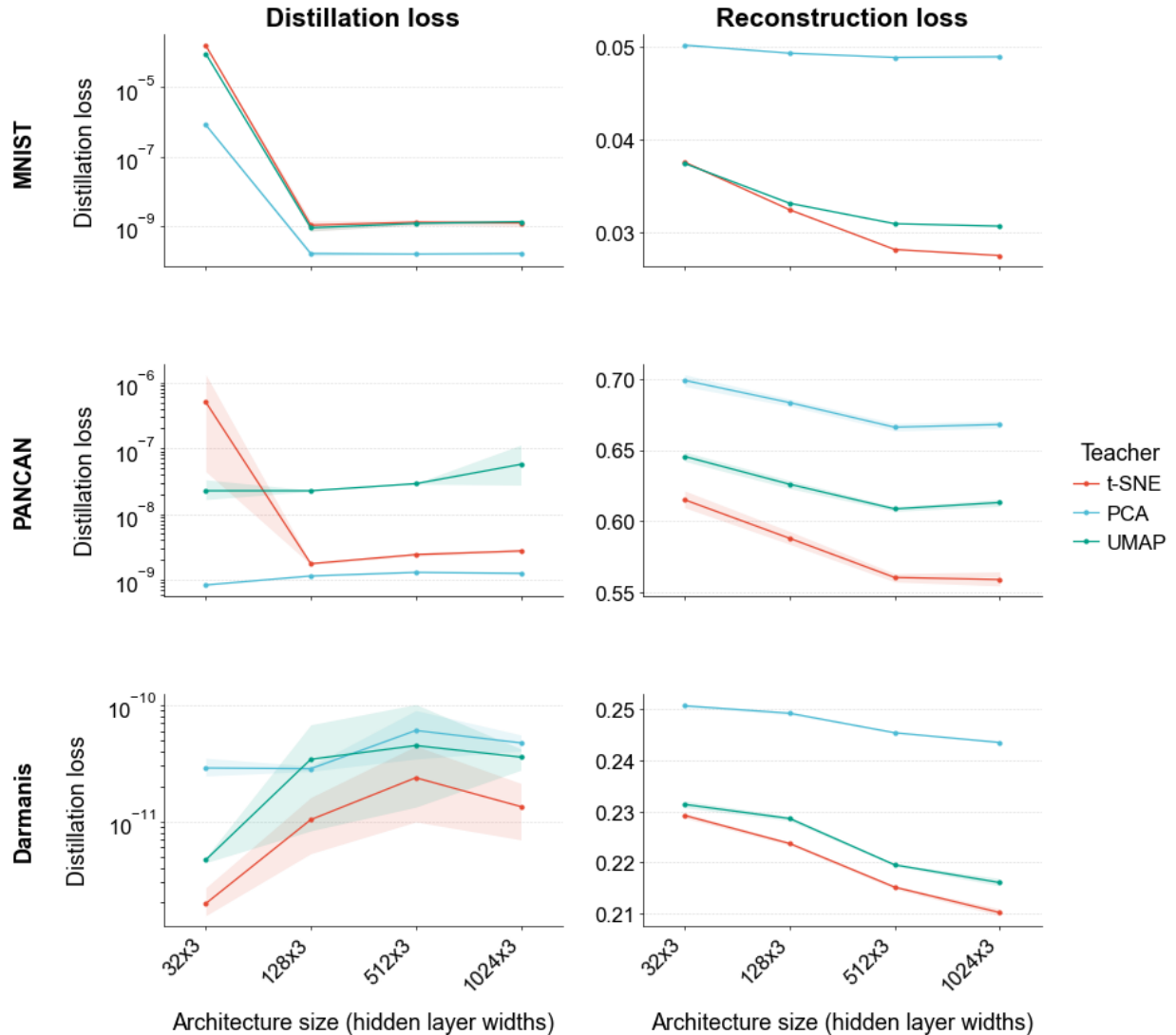


Figure S3: **Effect of per-layer width on distillation and reconstruction loss under a fixed depth.** Each line shows the mean \pm 95% CI across 20 random seeds. (*Left*) Distillation loss on a log scale. (*Right*) Reconstruction loss. Rows correspond to three datasets; colors denote teacher type.

Once the student is sufficiently expressive, near-zero empirical distillation becomes feasible. Increasing width improves approximation capacity and can reduce distillation loss, but only up to a point; beyond that, gains saturate while computational cost continues to increase. In practice, this suggests using architectures that are moderately overparameterized rather than extremely wide.

Activation analysis. This ablation examines how the encoder activation design affects distillation. Write the encoder output as

$$z_{\theta}(x) = \phi_{\text{bn}}(A h_{\theta}(x) + b),$$

where h_θ is the penultimate representation, A, b are the final affine parameters, and ϕ_{bn} is the bottleneck activation. We train autoencoders over the grid

$$\phi_{\text{bn}} \in \{\text{None, ReLU, SELU}\}, \quad \phi \in \{\text{None, ReLU, SELU}\},$$

holding all other training choices fixed, and report the median distillation loss over 20 random seeds. Results are shown in [Supplementary Figure S4](#), where the results for ReLU and SELU are aggregated as “Nonlinear.”

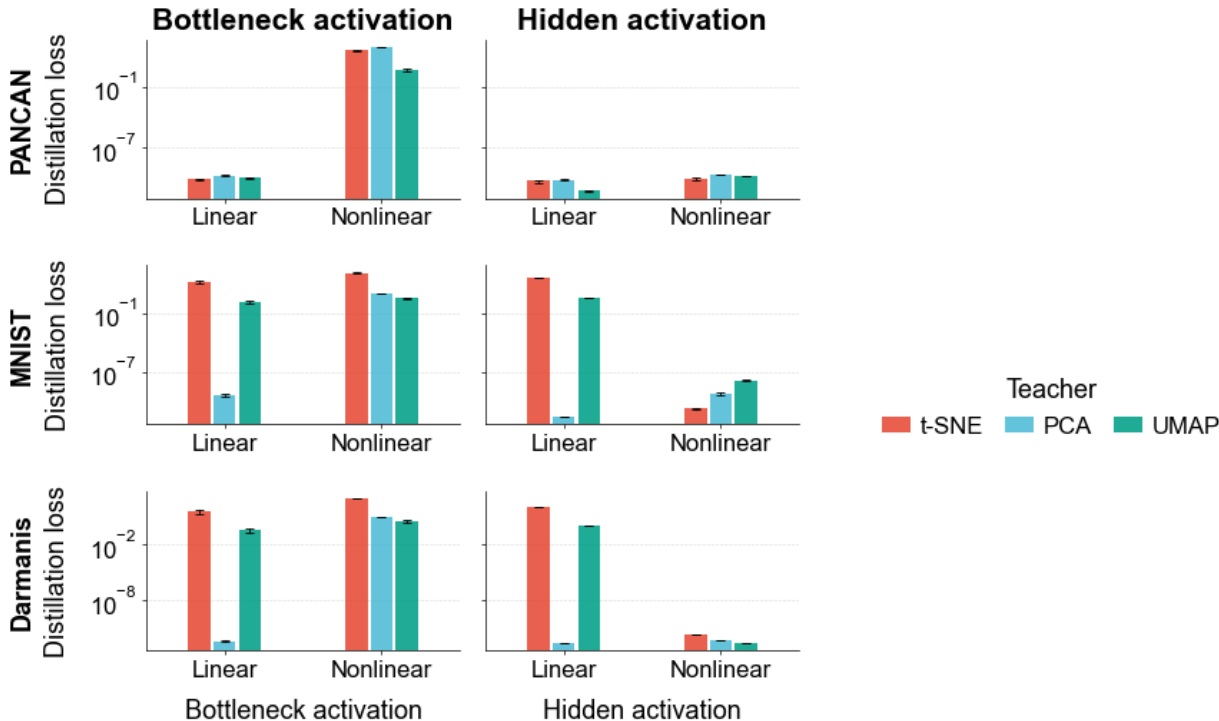


Figure S4: **Effect of bottleneck and hidden-layer activation on distillation loss.** Each bar shows the median distillation loss across 20 random seeds. (*Left*) Loss when the bottleneck activation is linear (identity) versus nonlinear (ReLU or SELU), marginalizing over all hidden-layer activations. (*Right*) Loss when the hidden-layer activation is linear versus nonlinear, conditioned on a linear bottleneck. Results are shown for three datasets (PANCAN, MNIST, Darmanis) and four teachers (t-SNE, PCA, UMAP, Spectral).

A linear bottleneck is required for near-zero distillation. Exact matching requires $z_\theta(x_i) = z_i$ for all training points. When ϕ_{bn} is the identity, the final affine head is unconstrained and can in principle reproduce any target coordinates. When ϕ_{bn} is nonlinear, the output is restricted to the image of that function: ReLU constrains each coordinate to $[0, \infty)$, and SELU to $(-\alpha\lambda, \infty)$ [54]. Teacher embeddings can contain values outside these ranges, producing an irreducible error floor regardless of how expressive h_θ is. The left panel of [Supplementary Figure S4](#) confirms this: a nonlinear bottleneck raises distillation loss by several orders of magnitude across datasets and teachers.

Hidden-layer nonlinearity is needed for nonlinear teachers. Conditioned on a linear bottleneck, a fully linear encoder can only represent affine functions of the input and therefore cannot

faithfully distill nonlinear teachers such as t-SNE or UMAP. The right panel of [Supplementary Figure S4](#) shows that switching the hidden layers from linear to nonlinear sharply reduces distillation loss for nonlinear teachers, whereas PCA, being a linear teacher, is already well matched by a linear encoder.

Together, these results give a simple design rule: near-zero distillation requires **(i)** a linear bottleneck activation and **(ii)** at least one hidden-layer nonlinearity when the teacher itself is nonlinear.

Adaptive optimization, stopping criteria, and teacher normalization. Different teacher embeddings exhibit markedly different optimization dynamics: some can be distilled to near-zero alignment rapidly, whereas others require substantially longer training. To handle this heterogeneity without teacher-specific tuning, we train all models with a common initial learning rate, a sufficiently large maximum budget, and PyTorch’s `ReduceLROnPlateau` scheduler. The scheduler monitors distillation loss and reduces the learning rate when progress plateaus, allowing easier distillation tasks to converge quickly while harder ones continue training with progressively smaller step sizes.

To monitor progress toward successful distillation, we define a target band corresponding to our near-zero distillation regime for the distillation loss and track when training enters this band. In practice, we treat runs with $\mathcal{L}_d \leq 9 \times 10^{-6}$ as successfully distilled. Empirically, this threshold provides a good balance across datasets, teachers, and teacher configurations: it yields embeddings that are visually indistinguishable from their teacher references while avoiding unnecessary compute once reconstruction has already stabilized.

Early stopping is based on both successful distillation and loss stabilization. Once the distillation loss enters the predefined near-zero regime and sufficient training history has accumulated, we estimate the local slope of both losses over a fixed stability window:

$$\frac{|\mathcal{L}_d^{(t)} - \mathcal{L}_d^{(t-w)}|}{w} < \epsilon_{\text{distill}}, \quad \frac{|\mathcal{L}_r^{(t)} - \mathcal{L}_r^{(t-w)}|}{w} < \epsilon_{\text{recon}},$$

where w is the stability window. If both conditions hold, the run is counted as stable for that checkpoint; otherwise the stability counter is reset. Training is terminated only after stability has been maintained for a predefined number of consecutive checkpoints (the patience parameter), and only when the run lies in the final target band. In our implementation, we typically use $\epsilon_{\text{distill}} = 10^{-7}$, $\epsilon_{\text{recon}} = 10^{-3}$, and `patience` = 50. If these criteria are not met, training continues until the maximum budget is reached. This adaptive schedule provides a single protocol that remains comparable across teachers while avoiding both over-training of easy cases and premature truncation of harder ones.

A further issue is that teacher reference embeddings can differ substantially in scale: the coordinate ranges of their x - and y -axes may vary across methods, hyperparameters, and datasets. Without adjustment, this would place the distillation objective and the induced reconstruction error on different numerical scales across teacher instances, making comparisons less fair. To address this, MEDAL normalizes each teacher embedding before distillation by first centering it at its empirical mean and then scaling by its root-mean-square radius,

$$\tilde{Z} = \frac{Z - \bar{Z}}{s}, \quad s = \sqrt{\frac{1}{n} \sum_{i=1}^n \|z_i - \bar{Z}\|^2},$$

where $\bar{Z} = n^{-1} \sum_{i=1}^n z_i$. This normalization puts teacher embeddings on a common scale, so that both distillation difficulty and reconstruction error are comparable across datasets, methods, and hyperparameter settings.

Recommendations for architecture and optimization setup

The preceding ablations suggest a practical training protocol rather than a single universally optimal architecture. In our experiments, effective MEDAL training is achieved by using enough capacity to reach the near-zero distillation regime, while avoiding architectures that are unnecessarily large relative to the dataset. We therefore recommend the following default setup.

- **Use a symmetric multilayer perceptron autoencoder with a linear bottleneck.** Hidden layers may use standard nonlinear activations such as RELU or SELU, but the encoder bottleneck should be left linear because the teacher coordinates are real-valued and should not be restricted by the range of a nonlinear activation. We also use a linear output layer for reconstruction.
- **Start with a moderate architecture and increase capacity only if distillation fails.** For many datasets, two to four hidden layers per side with widths in the range of 256–512 provide a useful starting point. For example, smaller or lower-dimensional datasets may be well served by architectures such as [256, 256], whereas higher-dimensional or more heterogeneous datasets may require [512, 512] or [512, 512, 512, 512]. The goal is not to maximize depth or width, but to use sufficient capacity so that the final distillation loss reaches the predefined near-zero regime.
- **Tune λ_d on a logarithmic scale and prioritize successful teacher matching.** In practice, we sweep λ_d over a small logarithmic grid, such as $\{10, 10^2, 10^3, 10^4\}$, or sample from the same range during random search. Values that are too small may give favorable reconstruction loss but fail to recover the teacher geometry, values that are excessively large for a given dataset can lead to inefficient optimization and, in finite training, potentially higher reconstruction error than necessary. We therefore choose λ_d large enough to reliably achieve near-zero distillation and then compare reconstruction only among successfully distilled runs.
- **Use adaptive optimization rather than a fixed training horizon.** We typically sweep the initial learning rate over $\{10^{-3}, 10^{-4}, 10^{-5}\}$, with 10^{-4} or 10^{-5} often providing stable behavior in larger experiments. A learning-rate scheduler such as `ReduceLRonPlateau` is useful because different teachers can have different optimization difficulty. Training is stopped only after the model enters the near-zero distillation band and both distillation and reconstruction losses have stabilized.
- **Keep the selected protocol fixed across teacher settings.** Once an architecture and training protocol are chosen for a dataset, the same setup should be reused across teacher hyperparameters and teacher methods. This prevents the held-out reconstruction comparison from being confounded by teacher-specific architecture tuning.

Overall, the recommended practice is to treat architecture and optimization as a feasibility step for achieving faithful teacher distillation. After this criterion is met, the primary comparison of interest is the reconstruction behavior induced by different teacher embeddings, rather than small differences in training configuration.

S2.2 Why near-zero distillation is feasible in principle

The practical results above show that near-zero empirical distillation is achievable with moderate architectures and careful optimization. This is also consistent with standard expressivity results for neural networks.

Classical universal approximation. Standard universal approximation theorems establish that multilayer perceptrons with non-polynomial activation functions are dense in spaces of continuous functions on compact domains [26, 46, 47, 61]. Later refinements show universality under bounded-width constructions [40, 69] and characterize approximation rates for deep ReLU networks [6, 38, 105]. These results justify the view that sufficiently expressive encoder networks can approximate a broad class of teacher maps.

Finite-sample interpolation. MEDAL, however, does not require approximation of a population-level map; it requires fitting teacher coordinates on a fixed finite training set. A complementary line of work shows that ReLU networks can interpolate arbitrary labels on a finite sample. In particular, Zhang et al. [107] showed that, for any set of n distinct inputs and scalar labels, a two-layer ReLU network can fit the labels exactly. For vector-valued targets, Yun et al. [106] give an explicit construction showing that a three-layer ReLU network with hidden widths d_1 and d_2 can memorize arbitrary r -dimensional outputs whenever $d_1 d_2 \geq 4nr$. Since the teacher coordinates in MEDAL are precisely vector-valued labels attached to the observed inputs, these results imply that exact fitting on the training set is feasible in principle.

Corollary 1 *Let $S = \{(x_i, z_i)\}_{i=1}^n$ with $x_i \in \mathbb{R}^k$ and $z_i \in \mathbb{R}^r$. Under the conditions of Theorem 3.1 of Yun et al. [106], there exists a three-layer ReLU network $g_\theta : \mathbb{R}^k \rightarrow \mathbb{R}^r$ with hidden widths d_1, d_2 satisfying $d_1 d_2 \geq 4nr$ such that*

$$g_\theta(x_i) = z_i, \quad i = 1, \dots, n.$$

Interpretation for MEDAL. These results are existence statements: they certify that weights achieving exact interpolation exist, but they do not guarantee that gradient-based training with reconstruction pressure will always find them at modest widths. For that reason, our main claim is empirical rather than purely theoretical. The theory explains why near-zero alignment should be possible in principle, while the ablations above show that it is achievable in practice with moderate architectures and reasonable computation.

S2.3 Reconstruction remains meaningful under distillation

A central question for MEDAL is whether reconstruction error remains meaningful once the bottleneck is constrained to match a prescribed teacher embedding. If the distillation constraint were too restrictive, reconstruction error might simply reflect optimization failure rather than information loss induced by the teacher manifold. To study this, we examine how reconstruction performance changes with bottleneck rank when the teacher is PCA. For each rank, we compare four models: an unconstrained vanilla autoencoder, PCA, a linear MEDAL model distilled from PCA, and a nonlinear MEDAL model distilled from the same PCA teacher. Reconstruction error is evaluated

on both training and held-out test data. This experiment is designed to answer a basic question: if we require the bottleneck to match a chosen manifold, how much reconstruction do we lose?

PCA provides a useful sanity check for this comparison. Classical results show that the global minima of the linear autoencoder objective recover the principal r -dimensional subspace of the data, up to a rotation within that subspace [5, 13, 82]. Accordingly, when the teacher is PCA and both encoder and decoder are linear, a distilled MEDAL model should reproduce the classical PCA reconstruction profile. At the same time, the vanilla autoencoder provides an important baseline: because it optimizes reconstruction alone, without any geometric constraint, it has an inherent advantage when reconstruction is the sole objective. Any competitive MEDAL curve should therefore be interpreted as evidence that reconstruction error remains informative even under a distillation constraint. All architectural choices, schedulers, early stopping criteria, and training protocols are kept identical across methods.

[Supplementary Figure S5](#) shows the resulting reconstruction curves on MNIST. The exact overlap between linear MEDAL + PCA and PCA across all ranks provides a clean sanity check: when both the teacher and the student are linear, MEDAL reproduces the classical PCA reconstruction behavior and does not introduce artificial distortion. This establishes that the distillation framework itself is compatible with a setting where the correct reconstruction profile is already known.

The nonlinear MEDAL + PCA model yields a second and more practically important observation. At very small bottleneck ranks, the vanilla autoencoder performs better, which is expected: when the latent dimension is extremely limited, an unconstrained model can devote the entire bottleneck to reconstruction. As the rank increases, however, nonlinear MEDAL + PCA quickly becomes competitive with the vanilla autoencoder and at moderate to large ranks can even outperform it on both training and test loss. One plausible interpretation is that reconstruction-only training leaves greater freedom in how the bottleneck is organized, whereas distillation to a strong teacher such as PCA anchors the latent representation to a meaningful low-dimensional geometry that can stabilize optimization and improve decoder use of those coordinates.

Taken together, these results support the validity of reconstruction error as a criterion after distillation. Distillation does not simply throw away reconstruction in exchange for geometry. Rather, it imposes structure on the bottleneck while retaining—and in this setting sometimes improving—reconstruction quality. Once teacher matching is essentially exact, the remaining reconstruction error can therefore be interpreted as a meaningful measure of how much input-space information is lost by compression through the teacher manifold. This is precisely the quantity later used in MEDAL for held-out model selection, method comparison, and pointwise distortion analysis.

S2.4 Held-out evaluation protocol

Once a suitable student architecture is identified for a given dataset, we reuse that architecture across the full grid of teacher hyperparameters to ensure fair comparison across teacher settings. For each setting, we repeat student training multiple times to account for optimization stochasticity and summarize performance across runs.

MEDAL enables a shared held-out evaluation protocol for nonlinear embeddings. For each teacher hyperparameter setting, we first fit the teacher embedding on a training split and then distill it into a student autoencoder. Because held-out evaluation is only meaningful when the student has faithfully recovered the teacher geometry, we first filter to runs that achieve our predefined near-zero distillation criterion. The learned encoder and decoder from these successfully distilled runs

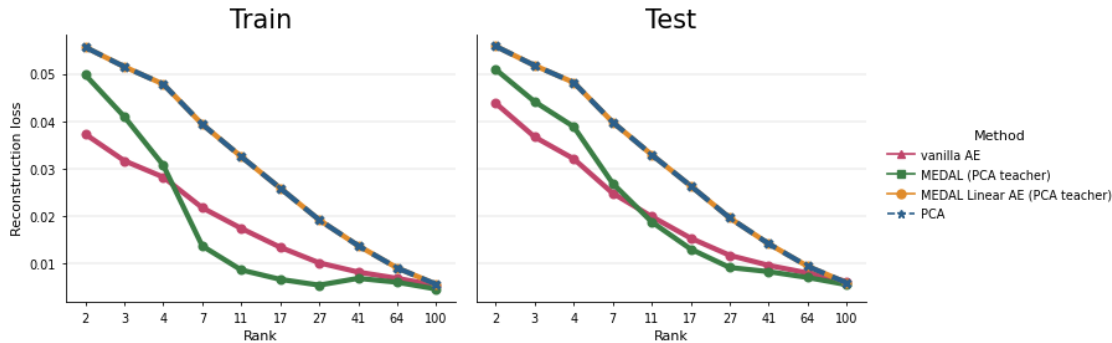


Figure S5: **Reconstruction error versus bottleneck rank on MNIST.** Train (left) and test (right) reconstruction loss are shown as a function of bottleneck rank for Vanilla AE, MEDAL + PCA, MEDAL Linear AE + PCA, and PCA. Linear MEDAL + PCA overlaps exactly with PCA across ranks, providing a sanity check in the linear setting. The nonlinear MEDAL + PCA model remains highly competitive with the unconstrained Vanilla AE and can outperform it at moderate and large ranks, showing that enforcing a geometrically meaningful bottleneck need not come at a substantial reconstruction cost.

are then applied to held-out validation observations: the encoder maps each point into the fixed teacher manifold learned from the training split, and the decoder maps that point back to the original feature space. Reconstruction loss on the held-out data, reported as mean \pm one standard error over the successfully distilled reruns, is then used as the evaluation criterion.

This protocol differs from conventional DR practice, where hyperparameters are often chosen visually from the training embedding alone. Because MEDAL equips the teacher with an explicit out-of-sample map and approximate inverse, teacher settings can instead be compared by how well they preserve information for unseen data. The same protocol also allows different DR methods to be evaluated on a more common basis, since each teacher is distilled into the same student class and assessed by the same held-out reconstruction criterion.

Compute and parallelization. To keep wall-clock time reasonable while sweeping teacher hyperparameters and seeds, we launch trials in parallel with *Ray Tune*. Each trial runs the same training loop and terminates as soon as it (i) enters the near-zero distillation band and (ii) satisfies the stabilization check for both distill and reconstruction losses, so compute is not spent past the point of diminishing returns (see [section S2.1](#)). Trials are independent (teacher \times hyperparameter \times seed) and scheduled concurrently with per-trial resource caps; exact allocations are adjusted per dataset and affect only wall-clock time, not the reported metrics. Ray Tune handles logging, checkpointing, and automatic retries, allowing many candidates to be swept quickly while keeping the student architecture and training budget fixed.

S3 Additional Case Study Results

Throughout the experiments, we tune the standard neighborhood-size parameters of each teacher method. For UMAP, `n_neighbors` controls the size of the local neighborhood used to construct the manifold graph: smaller values emphasize finer local structure, whereas larger values place more

weight on global organization. For t-SNE, perplexity plays an analogous role as an effective neighborhood size in the high-dimensional affinity construction, with smaller perplexities favoring more local separation and larger perplexities producing smoother, more global embeddings. For PHATE and spectral embedding, we similarly tune the neighborhood parameter used to construct the underlying graph. Unless otherwise stated, all hyperparameter comparisons are made after distilling each fitted teacher embedding into the same MEDAL student architecture within a dataset.

S3.1 MNIST

The same validation principle can also be used to choose the embedding dimension with MEDAL. For PCA, the retained rank is commonly selected from a scree plot and the elbow heuristic [19]. For nonlinear teachers such as UMAP, analogous dimension-selection criteria are ill-defined; the embedding dimension is instead a user-specified hyperparameter, despite such embedding often used as an intermediate representation for downstream clustering or scientific inference [31, 84]. In Supplementary Figure S6, we show that MEDAL provides a shared criterion for selecting the student bottleneck dimension across PCA and UMAP teachers by minimizing held-out reconstruction error on MNIST.

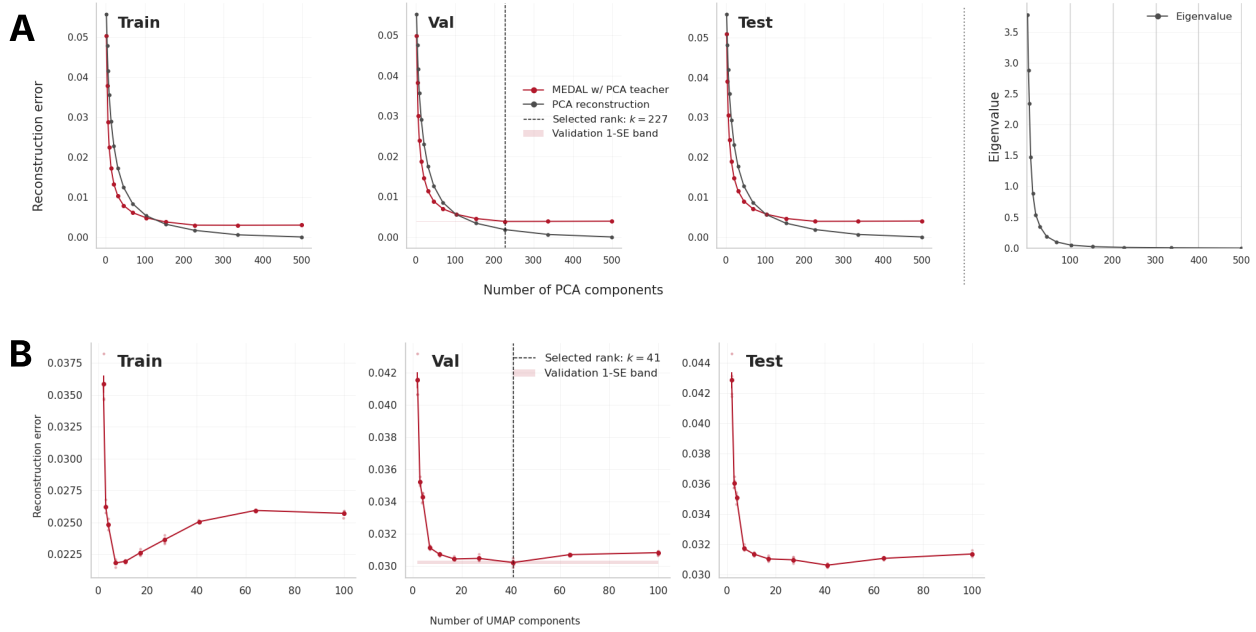


Figure S6: **Tuning the retained dimension of PCA and UMAP teachers.** (A) PCA provides a proof-of-concept setting in which the exact rank- k reconstruction error is available. Although MEDAL is not needed to tune the rank of a PCA teacher, the MEDAL reconstruction score closely tracks the exact PCA reconstruction error across train, validation, and test splits. The eigenvalue scree plot is shown for reference. In contrast to the classical scree-plot elbow criterion, validation reconstruction can favor a larger retained rank because it directly optimizes held-out input-space recovery: many low-variance components contribute little individually but collectively reduce reconstruction error. (B) For nonlinear teachers such as UMAP, there is no analogous eigenvalue scree plot. MEDAL extends the same validation-reconstruction principle to select the embedding dimension of a fitted nonlinear DR teacher. This provides a quantitative criterion for choosing the dimension of a UMAP representation before downstream analyses such as clustering, cell-state annotation, or other embedding-based tasks [7, 42]. Vertical dashed lines mark the selected dimension; shaded bands indicate the validation one-standard-error band.

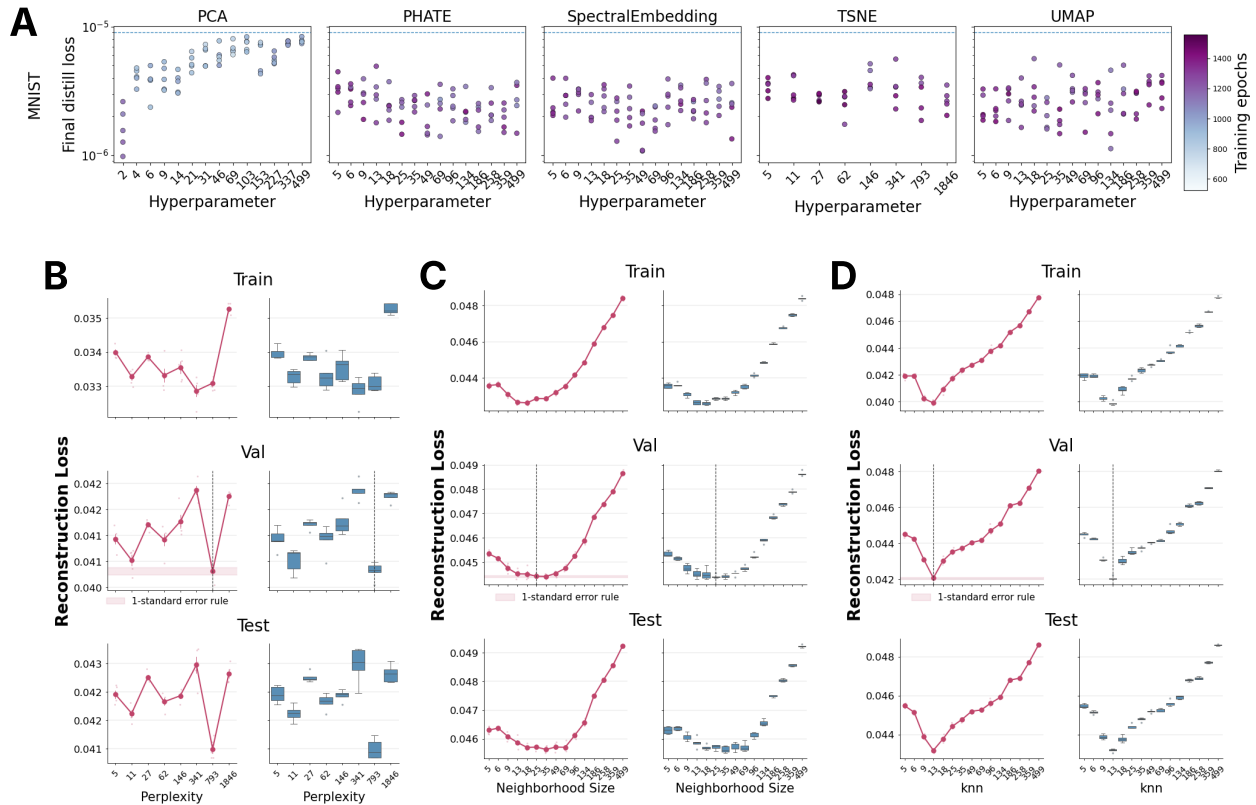


Figure S7: **MNIST Hyperparameter Tuning.** **A**, Distillation results for all MNIST runs. **B**, t-SNE teacher, tuning perplexity. **C**, SpectralEmbedding teacher, tuning `n_neighbors`. **D**, PHATE teacher, tuning `knn`.

We extended the MNIST hyperparameter-tuning analysis to additional teacher methods, including t-SNE, PHATE and spectral embedding (Supplementary [Supplementary Figure S7](#)). For each teacher, we distilled embeddings across a method-specific hyperparameter grid using the same student architecture and training protocol, and summarized reconstruction performance across five runs using both the mean and the median. We set up an encoder network of 4 512-neuron layers, successfully distilling teacher embeddings across all hyperparameters.

S3.2 Hydra

S3.3 Neocortex

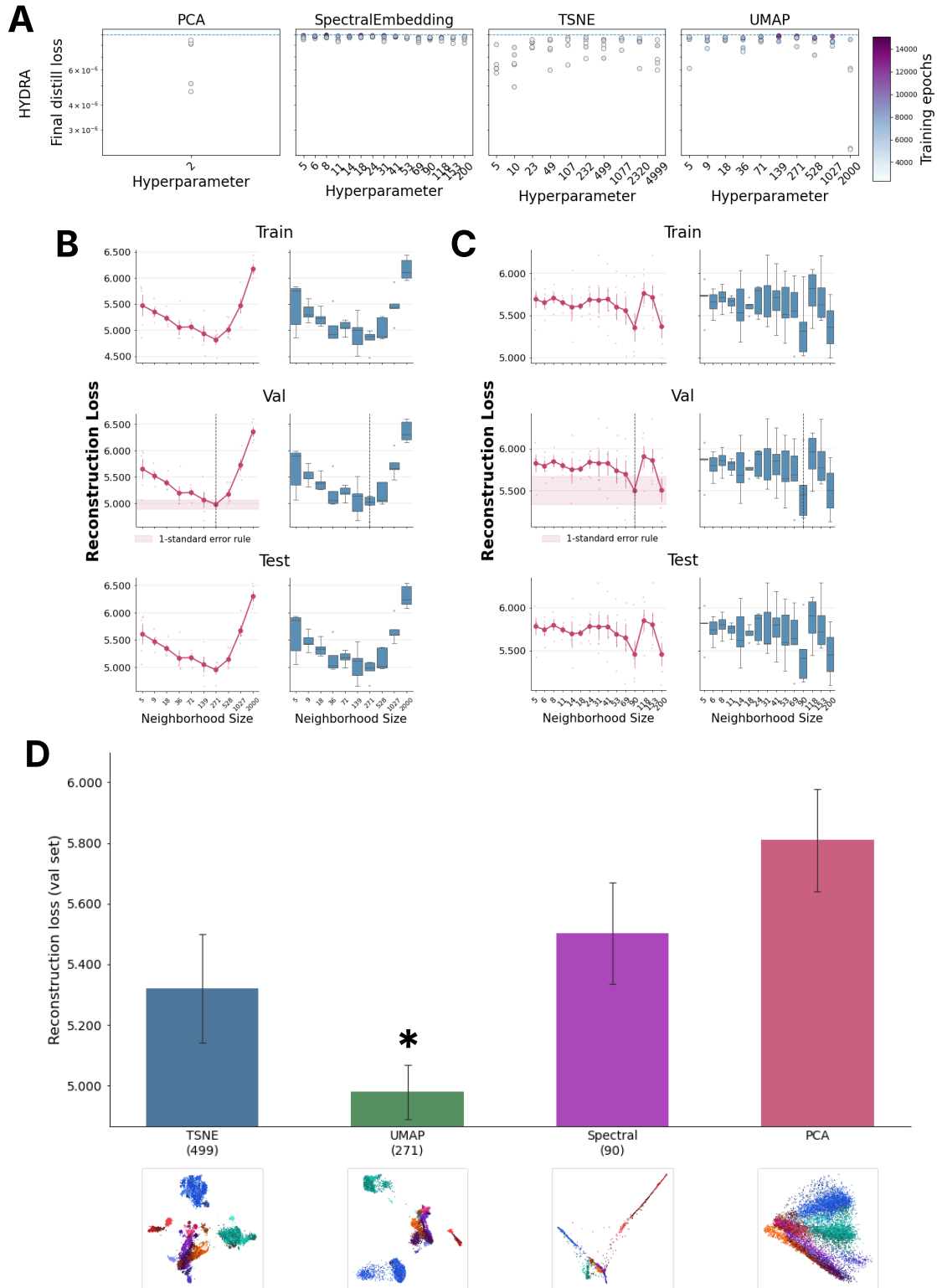


Figure S8: **Hydra Hyperparameter Tuning**. **A**, Distillation results for all Hydra runs. **B**, UMAP teacher, tuning `n_neighbors`. **C**, SpectralEmbedding teacher, tuning `n_neighbors`. **D**, Comparing different DR methods on Hydra using heldout reconstruction error.

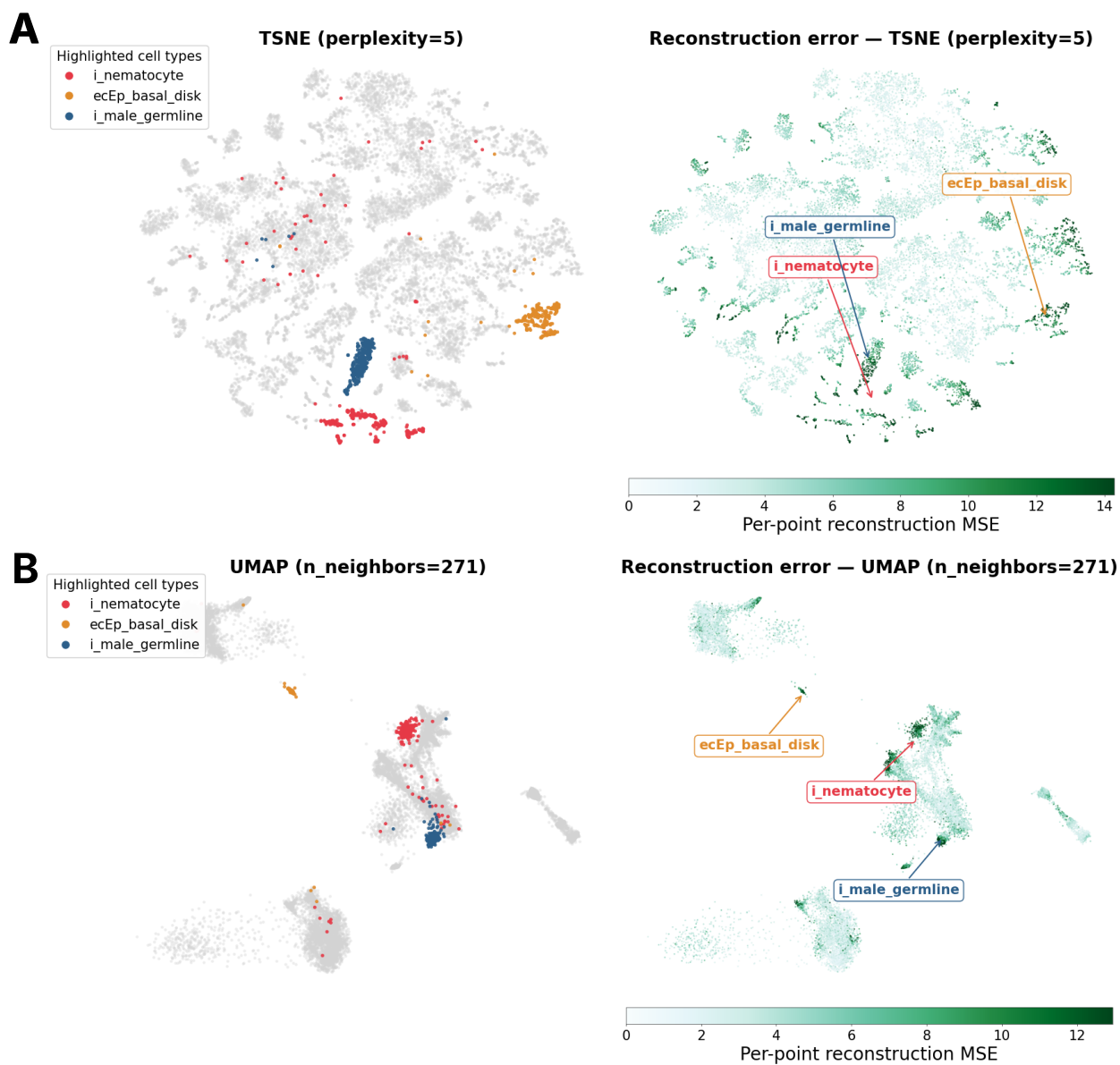


Figure S9: **MEDAL identifies consistent biologically structured distortion across Hydra teacher embeddings.** **A**, MEDAL distortion analysis for a t-SNE teacher with small perplexity (perplexity = 5). Left: Hydra embedding with three cell populations highlighted: interstitial nematocytes (`i_nematocyte`), ectodermal basal disk epithelial cells (`ecEp_basal_disk`), and male germline cells (`i_male_germline`). Right: the same embedding colored by per-point reconstruction mean squared error. **B**, MEDAL distortion analysis for a UMAP teacher (`n_neighbors` = 271), shown with the same highlighted cell populations and corresponding reconstruction-error map. Across both teacher settings, high reconstruction error repeatedly localizes near the same biologically distinct cell populations highlighted in the main Hydra analysis. This consistency suggests that the distortion signal is not an artifact of a single t-SNE hyperparameter choice, but reflects cell populations whose high-dimensional transcriptomic structure is difficult to preserve in a two-dimensional embedding. Color scales are shown separately for each teacher embedding.

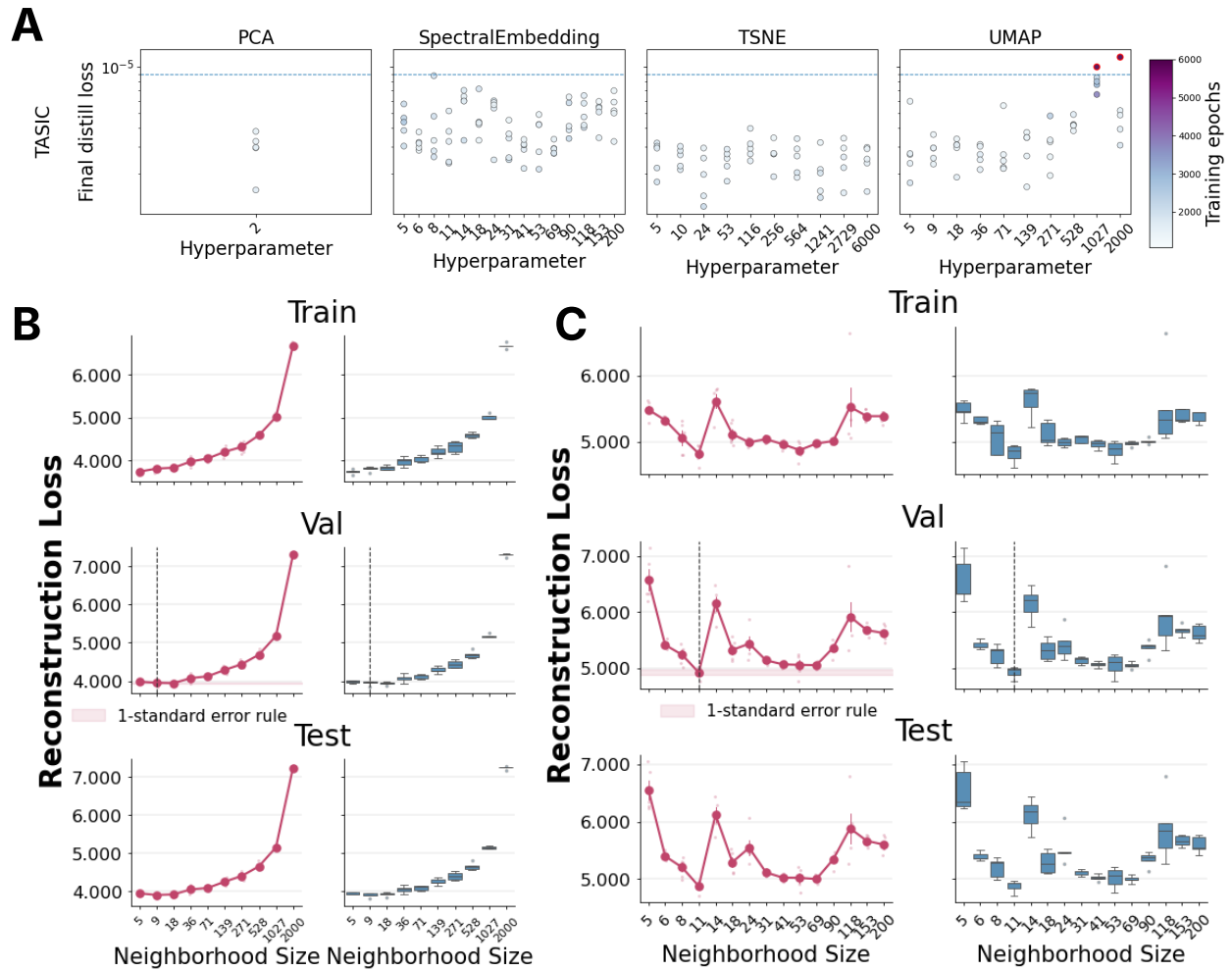


Figure S10: **Neocortex Hyperparameter Tuning.** **A**, Distillation results for all Neocortex runs. **B**, UMAP teacher, tuning `n_neighbors`. **C**, SpectralEmbedding teacher, tuning `n_neighbors`.

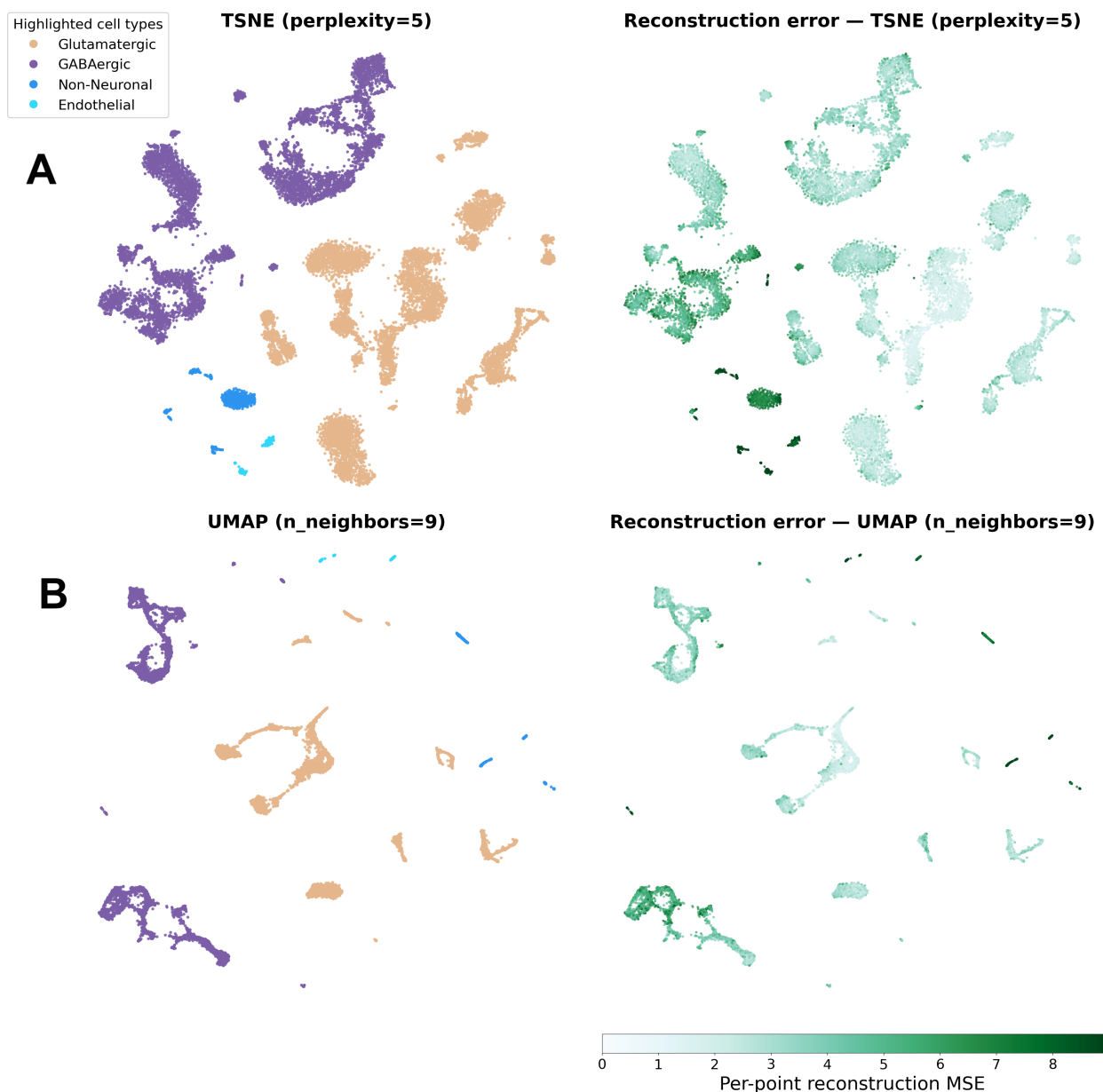


Figure S11: **MEDAL identifies consistent biologically structured distortion across Neocortex teacher embeddings.** **A**, Distortion analysis for a t-SNE teacher with small perplexity (perplexity = 5). Left: the Neocortex embedding with broad annotated cell classes highlighted, including glutamatergic neurons, GABAergic neurons, non-neuronal cells, and endothelial cells. Right: the same embedding colored by MEDAL per-point reconstruction mean squared error. **B**, Distortion analysis for a UMAP teacher (`n_neighbors = 9`), shown with the same highlighted cell classes and corresponding reconstruction-error map. Across both teacher settings, higher reconstruction error remains concentrated disproportionately in non-neuronal and endothelial regions relative to the major neuronal populations. This consistency supports the main-text observation that MEDAL identifies a stable, biologically coherent distortion signal in the Neocortex dataset, rather than an artifact of a single teacher or hyperparameter choice.

S3.4 APOGEE stellar spectra: additional physical-sciences benchmark

To assess whether MEDAL’s validation workflow extends beyond image and single-cell genomics datasets, we also applied MEDAL to APOGEE stellar spectra. This dataset consists of approximately 8,000 stellar spectra, each represented by flux measurements across 19 wavelength bands. The data and preprocessing pipeline follow Chang et al. [20]. Unlike MNIST or the single-cell atlases, APOGEE does not have externally validated class labels for the present analysis; cluster assignments from the prior unsupervised analysis are therefore used only for visualization, not as ground-truth labels.

Despite this limitation, APOGEE provides a useful domain-diversity check for MEDAL. We repeated the same validation workflow used in the main case studies: distilling t-SNE and UMAP teachers across hyperparameter grids, selecting hyperparameters by held-out reconstruction loss, comparing selected teacher methods under a shared reconstruction criterion, and visualizing point-wise reconstruction error. MEDAL selected a t-SNE teacher with perplexity 6 and a UMAP teacher with `n_neighbors = 359`. Under the shared validation criterion, t-SNE achieved the lowest held-out reconstruction loss among the teachers considered, followed by UMAP and PCA (Supplementary Figure S12). These results show that MEDAL can be applied as a general validation layer in a physical-sciences dataset, although the absence of ground-truth labels limits the strength of biological or physical interpretation relative to the main case studies.

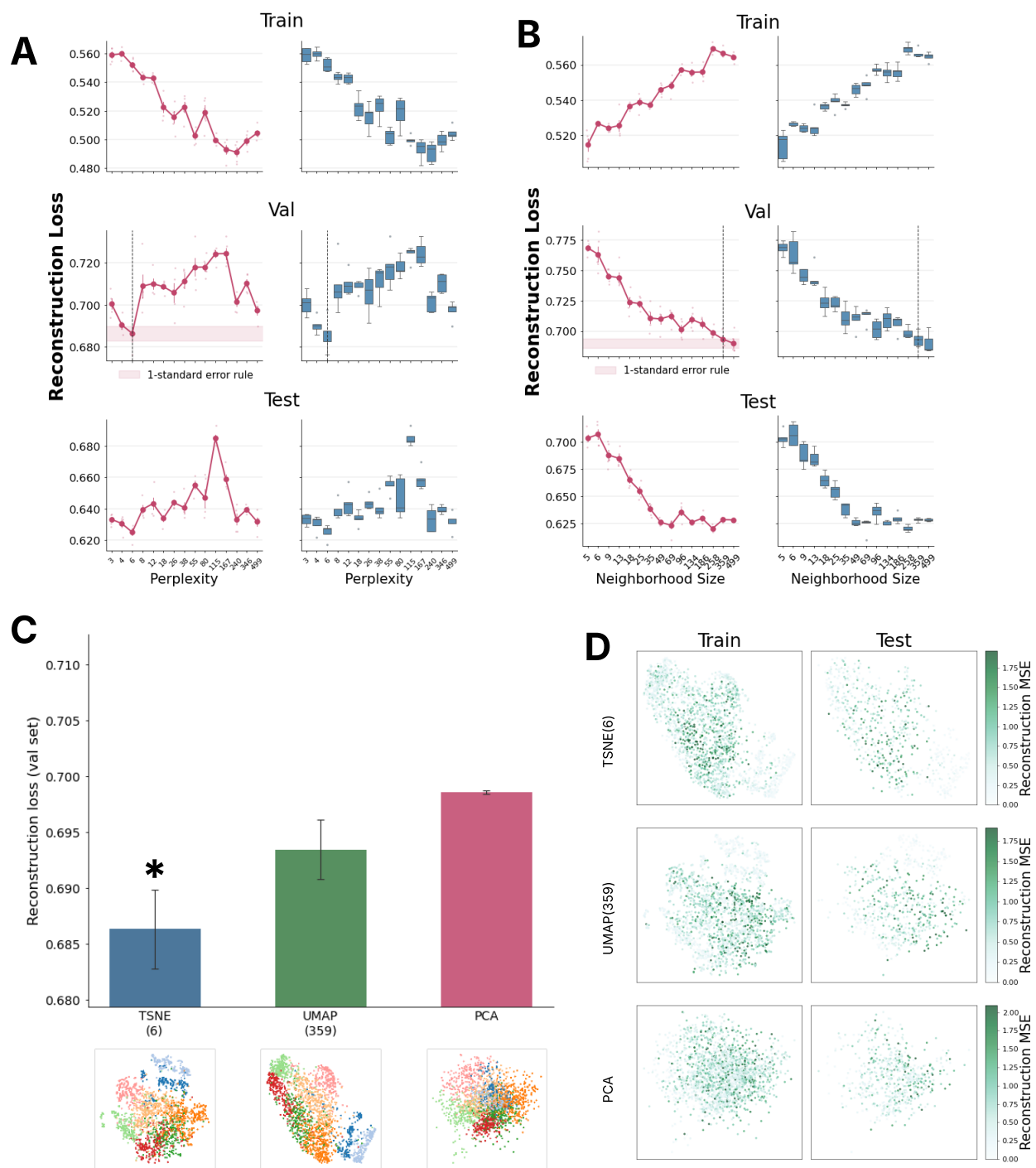


Figure S12

Figure S12: **MEDAL validation on APOGEE stellar spectra.** **A**, MEDAL hyperparameter tuning for t-SNE teachers across perplexity values. Reconstruction loss is shown on train, validation, and test splits, with the selected perplexity indicated by the dashed vertical line. **B**, MEDAL hyperparameter tuning for UMAP teachers across neighborhood sizes. Reconstruction loss is again evaluated on train, validation, and test splits, with the selected `n_neighbors` indicated by the dashed vertical line. **C**, Comparison across dimension-reduction teachers under the MEDAL validation protocol. t-SNE at perplexity 6 achieved the lowest validation reconstruction loss among the methods considered, followed by UMAP at `n_neighbors = 359` and PCA. **D**, Point-wise reconstruction-error maps for the selected t-SNE, UMAP, and PCA embeddings on train and test splits. Cluster colors are used only for visualization and are taken from the prior unsupervised analysis of this dataset, rather than from externally validated ground-truth labels.

S3.5 Macaque retina: additional mixed-subject batches and comparison with `umap.transform()`

We performed additional macaque retina analyses to test whether the out-of-distribution signal reported in the main text was specific to a single subject comparison or to a single choice of reference manifold. We considered three extensions. First, in addition to the M1-versus-M2 comparison shown in [Supplementary Figure 6](#), we projected M3 cells onto the M1 reference manifold. Second, we reversed the reference subject by training MEDAL on M2 cells and projecting M1 cells onto the M2 reference manifold. Third, we compared MEDAL with `umap.transform()`, a commonly used practical tool for embedding new data into an existing manifold. Throughout, M1, M2, and M3 denote cells from macaque subjects 1, 2, and 3, respectively.

Additional mixed-subject batches on the M1 reference manifold. We first trained MEDAL on M1 training cells and projected three held-out datasets onto the resulting M1 reference manifold: an in-distribution batch of M1 test cells, a mixed batch containing M1 test and M2 cells, and a mixed batch containing M1 test and M3 cells. For the in-distribution M1 test batch, embedded cells remained aligned with the reference geometry and reconstruction error was low. In contrast, both mixed-subject batches showed spatially coherent increases in reconstruction error concentrated primarily among the out-of-distribution cells ([Supplementary Figure S15](#)). Thus, the shift-detection behavior observed in the main text is not specific to the M1-versus-M2 comparison, but extends to a second held-out subject.

We further quantified the M1-versus-M3 comparison by examining reconstruction error within each retinal cell type ([Supplementary Figure S13](#)). Relative to the M1 in-distribution baseline, M3 cells showed elevated reconstruction error across most cell types, with the largest shifts observed in Müller glia and endothelial populations, followed by rods. This confirms that the subject-level mismatch detected by MEDAL is not only a global batch effect, but is concentrated in specific biological populations.

Reverse-reference experiment. We next reversed the reference subject by training MEDAL on M2 cells and embedding held-out M2 test cells together with a mixed batch containing M1 and M2 cells onto the M2 reference manifold ([Supplementary Figure S14](#)). The same broad pattern reappeared: out-of-distribution M1 cells showed elevated reconstruction error relative to the M2 in-distribution baseline, with prominent shifts in non-neuronal populations. This indicates that the subject-level mismatch detected by MEDAL is not tied to a single reference subject, but reflects a

more stable pattern of inter-subject distributional shift.

Comparison with `umap.transform()`. Finally, we compared MEDAL with `umap.transform()` applied to the same M1 reference embedding (Supplementary Figure S15). Both approaches can place new cells into an existing low-dimensional coordinate system. However, `umap.transform()` provides only coordinates: it does not report whether the new cells are well supported by the reference distribution. As a result, out-of-distribution M2 and M3 cells can appear visually integrated into the M1 manifold, even though the same cells exhibit clear subject-level mismatch under MEDAL’s reconstruction-error diagnostic.

This contrast highlights the practical value of MEDAL’s encoder–decoder construction. The encoder maps new cells into the reference manifold, while the decoder quantifies whether those embedded cells can be faithfully reconstructed from the reference geometry. Reconstruction error therefore acts as an unsupervised reliability signal for out-of-sample embedding: it detects subject-level mismatch, localizes the mismatch spatially on the manifold, and identifies the cell populations most affected by the shift.

S3.6 Comparison to other methods

We compared MEDAL with three existing embedding-diagnostic methods: EMBEDR, scDEED, and neMDBD. These methods differ in both their diagnostic target and their computational workflow. EMBEDR assigns pointwise p-values by comparing an embedding statistic against a permutation-based null distribution [51]. scDEED identifies trustworthy, intermediate, and dubious embedding structure using null embeddings and selects hyperparameters by minimizing dubious points [103]. neMDBD instead uses a local singularity score to measure geometric distortion [64]. In contrast, MEDAL distills each candidate embedding into an encoder–decoder model and selects hyperparameters by held-out reconstruction error.

Because these methods are designed as complete systems, we evaluated each method as it would be used in practice. Thus, the comparison is a whole-system comparison: each method uses its own embedding implementation, optimization pipeline, and recommended diagnostic criterion. As a result, two methods may produce different embeddings even when they select the same nominal hyperparameter. neMDBD was omitted from UMAP comparisons because the available package does not support UMAP. Following Xia et al. [103], we applied PCA preprocessing before running scDEED. We retained 6 principal components for MNIST, 5 principal components for APOGEE and 4 principal components for Hydra and Neocortex. Consequently, scDEED results are computed from PCA-reduced inputs rather than from the original feature space, and should be interpreted as evaluating scDEED under its recommended preprocessing workflow.

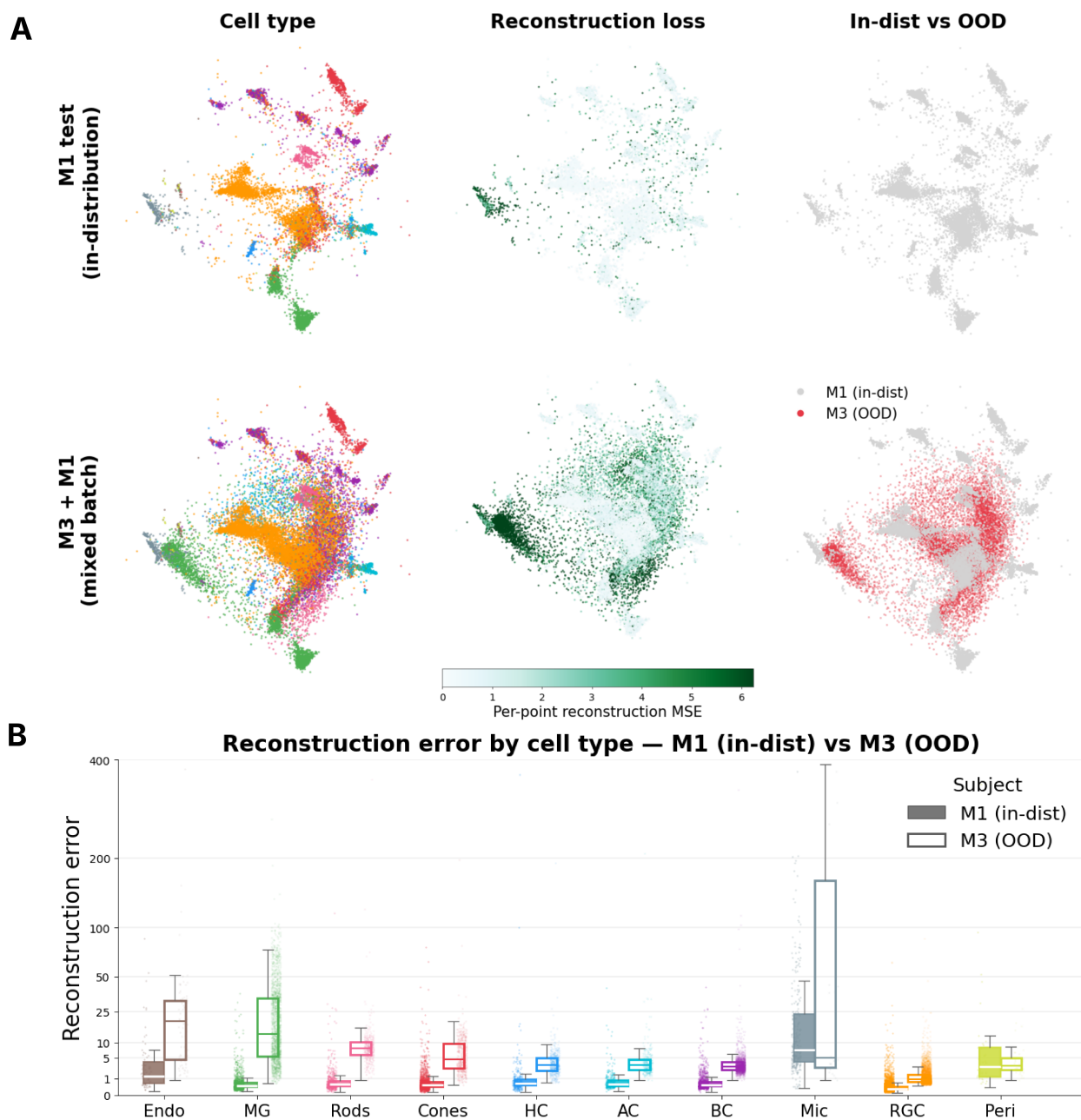


Figure S13: Cell-type-resolved reconstruction error for M1 versus M3 in macaque retina. MEDAL was trained on M1 training cells and used to project held-out M1 test cells and M3 cells onto the M1 reference manifold. Reconstruction error distributions are shown by retinal cell type for in-distribution M1 cells and out-of-distribution M3 cells. Errors are shown on a log scale. Relative to the M1 baseline, M3 cells show elevated reconstruction error across most cell types, with the largest shifts observed in Müller glia and endothelial populations, followed by rods. This indicates that the subject-level mismatch detected by MEDAL is concentrated in specific biological populations rather than being uniformly distributed across the atlas.

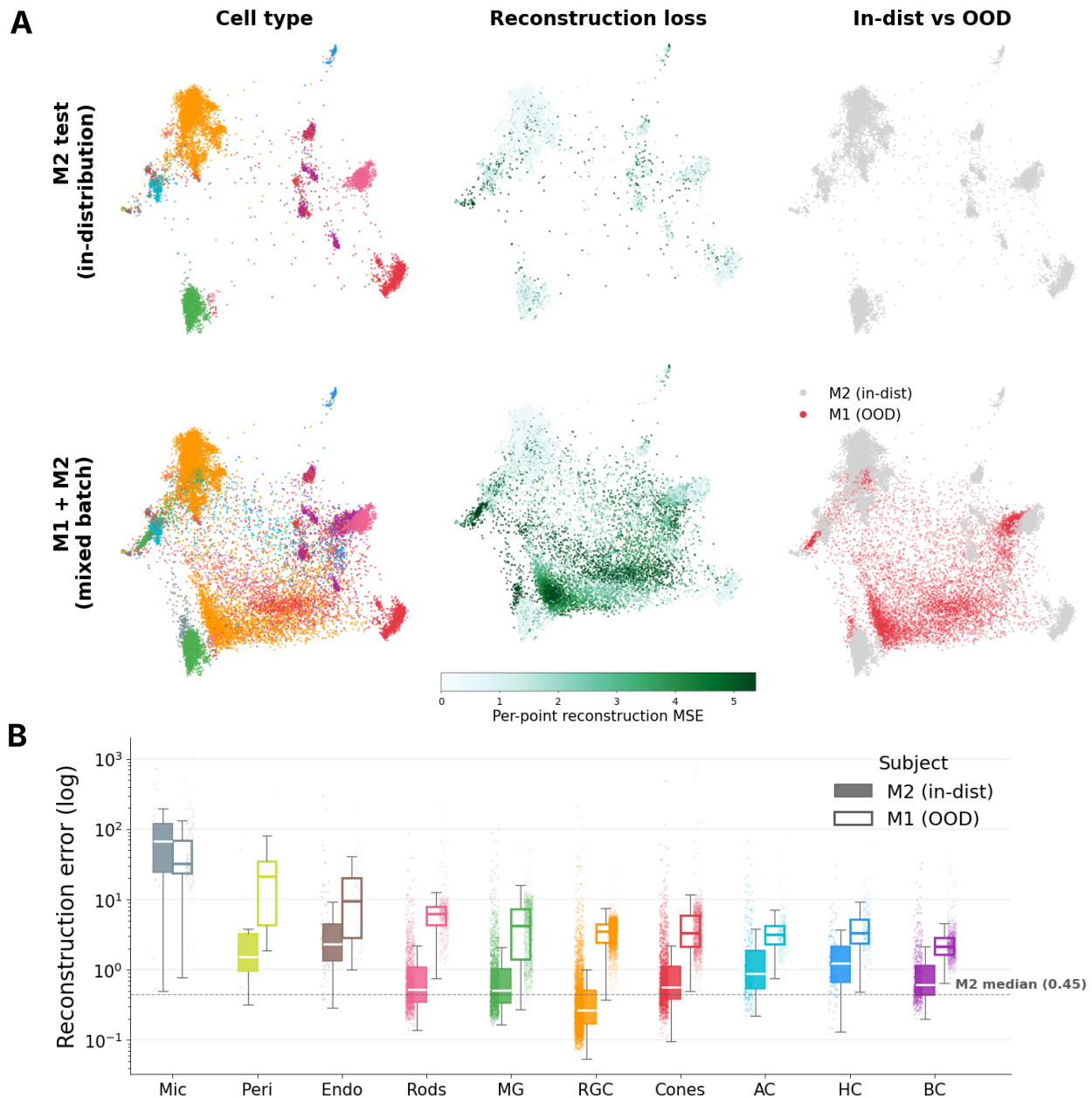


Figure S14: **Reverse-reference experiment with M2 as the reference manifold.** MEDAL was trained on M2 training cells and used to embed held-out M2 test cells and a mixed batch containing M1 and M2 cells onto the M2 reference manifold. In-distribution M2 cells remain aligned with the reference geometry and show lower reconstruction error, whereas out-of-distribution M1 cells exhibit elevated reconstruction error. The strongest shifts again occur in non-neuronal populations, indicating that the subject-level mismatch detected by MEDAL is not specific to using M1 as the reference subject. Reconstruction error is shown on a log scale.

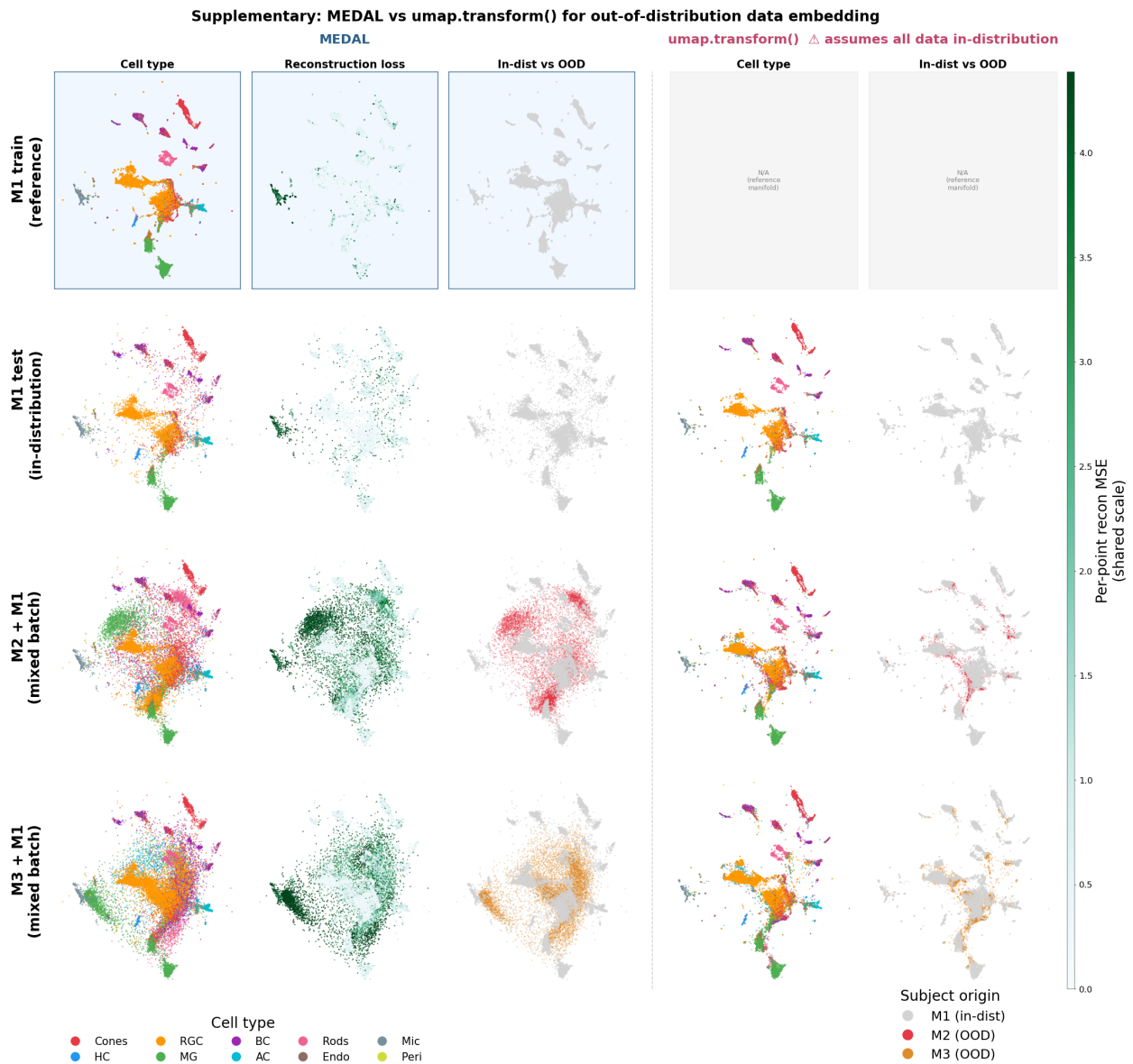


Figure S15: **MEDAL detects subject-level mismatch when embedding new macaque retina cells into a fixed reference manifold.** MEDAL was trained on M1 training cells and used to embed M1 test cells, M1 test + M2 mixed cells, and M1 test + M3 mixed cells onto the same M1 reference manifold. For in-distribution M1 test cells, reconstruction error remains low and the embedded cells align with the reference geometry. In mixed-subject batches, out-of-distribution M2 and M3 cells occupy shifted regions of the embedding and show spatially coherent increases in reconstruction error. The right panels show the corresponding `umap.transform()` embeddings. Although `umap.transform()` places new cells into the existing coordinate system, it does not provide an accompanying reconstruction-based diagnostic of whether those cells are supported by the reference distribution.

Hyperparameter tuning and distortion comparisons For each dataset and teacher method, we show the hyperparameter-selection curve for each diagnostic and the embedding selected by that method. The top row of each embedding panel is colored by the available class, cell-type, or cluster annotation, while the bottom row shows the method-specific pointwise diagnostic: MEDAL reconstruction error, neMDBD singularity score, scDEED trustworthy/intermediate/dubious labels, or EMBEDR p-values. These pointwise scores are not on a common numerical scale; the comparison is qualitative and aims to show whether the selected hyperparameter and diagnostic signal produce coherent regions of embedding distortion.

Across these comparisons, the existing diagnostics sometimes select hyperparameters at the boundaries of the candidate range, such as very small perplexities or very large neighborhood sizes. We do not interpret these boundary selections as inherently incorrect, since different diagnostics emphasize different aspects of embedding quality. However, they often correspond to visually distinct embedding regimes—for example, highly local embeddings with fragmented structure or highly global embeddings with smoother, more compressed geometry. As shown in the main case studies, such regimes can appear plausible on the fitted embedding while differing substantially in how well they support held-out observations. This is the central distinction of MEDAL: after distilling each candidate embedding into an encoder–decoder model, MEDAL evaluates reconstruction error on held-out data, providing an explicit out-of-sample criterion for hyperparameter selection.

The resulting pointwise signals also differ in interpretability. scDEED produces discrete trustworthy/intermediate/dubious labels, which are useful for flagging suspicious embedding structure but can be coarse for localizing graded distortion. neMDBD reports a singularity score, which captures local geometric irregularity but can be spatially noisy and less directly tied to information loss in the original feature space. EMBEDR provides pointwise p-values for neighborhood preservation, but these are less directly interpretable as a measure of how much high-dimensional signal is lost by the embedding. By contrast, MEDAL’s reconstruction error has a direct operational interpretation because it measures how well an observation can be recovered after being compressed through the fitted teacher manifold. In the examples below, this often yields spatially coherent distortion maps and selects embeddings that balance local separation with global organization, a pattern also reflected in the complementary LCMC and triplet-accuracy metrics reported next.

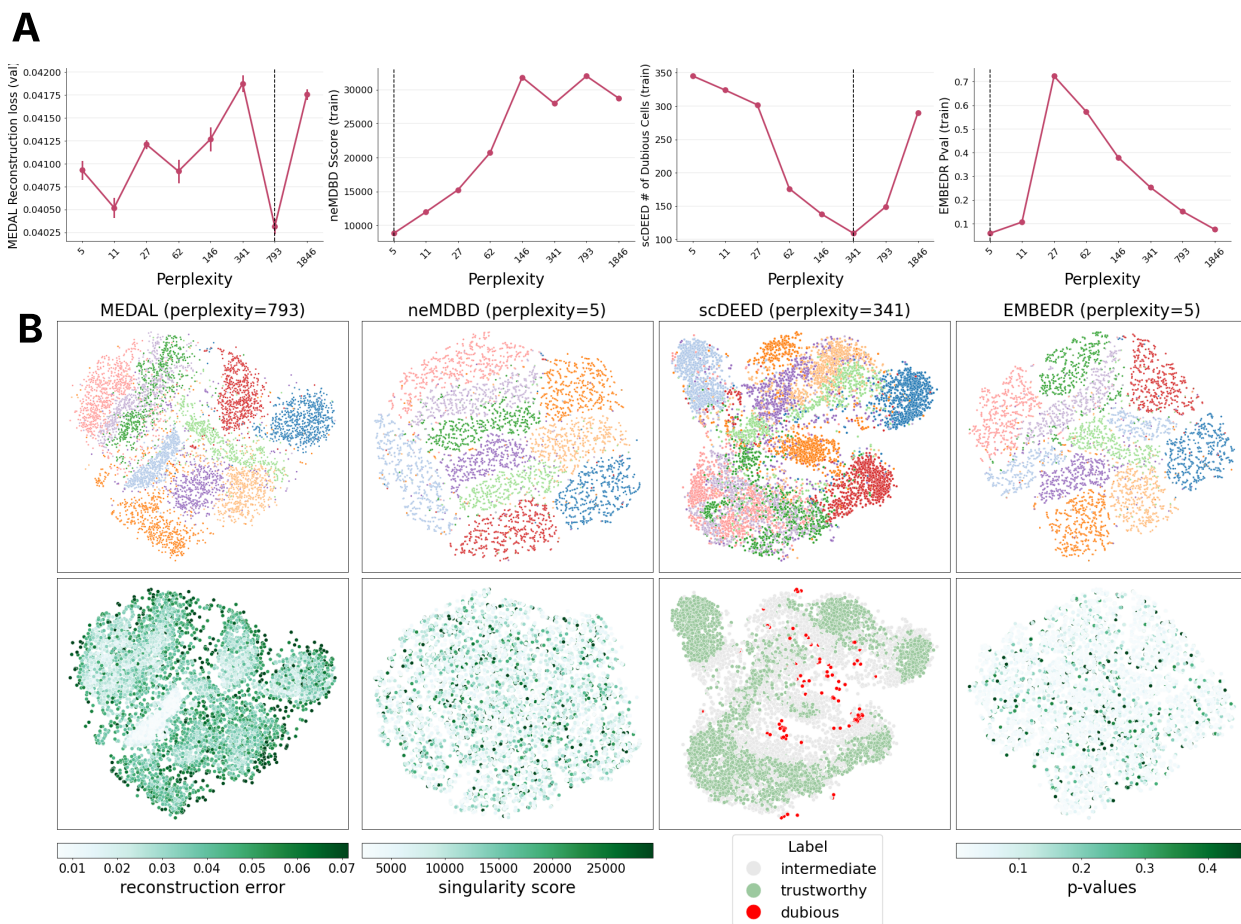


Figure S16: **Comparison of MEDAL with existing diagnostics on MNIST t-SNE embeddings.** **A**, Hyperparameter-selection curves across t-SNE perplexities for MEDAL, neMDBD, scDEED, and EMBEDR. Dashed vertical lines indicate the selected perplexity under each method’s criterion. **B**, Embeddings selected by each method. Top row: embeddings colored by digit label. Bottom row: method-specific pointwise diagnostics: MEDAL reconstruction error, neMDBD singularity score, scDEED trustworthy/intermediate/dubious labels, and EMBEDR p-values. MEDAL selects a larger perplexity embedding, whereas neMDBD and EMBEDR select the smallest perplexity in the grid.

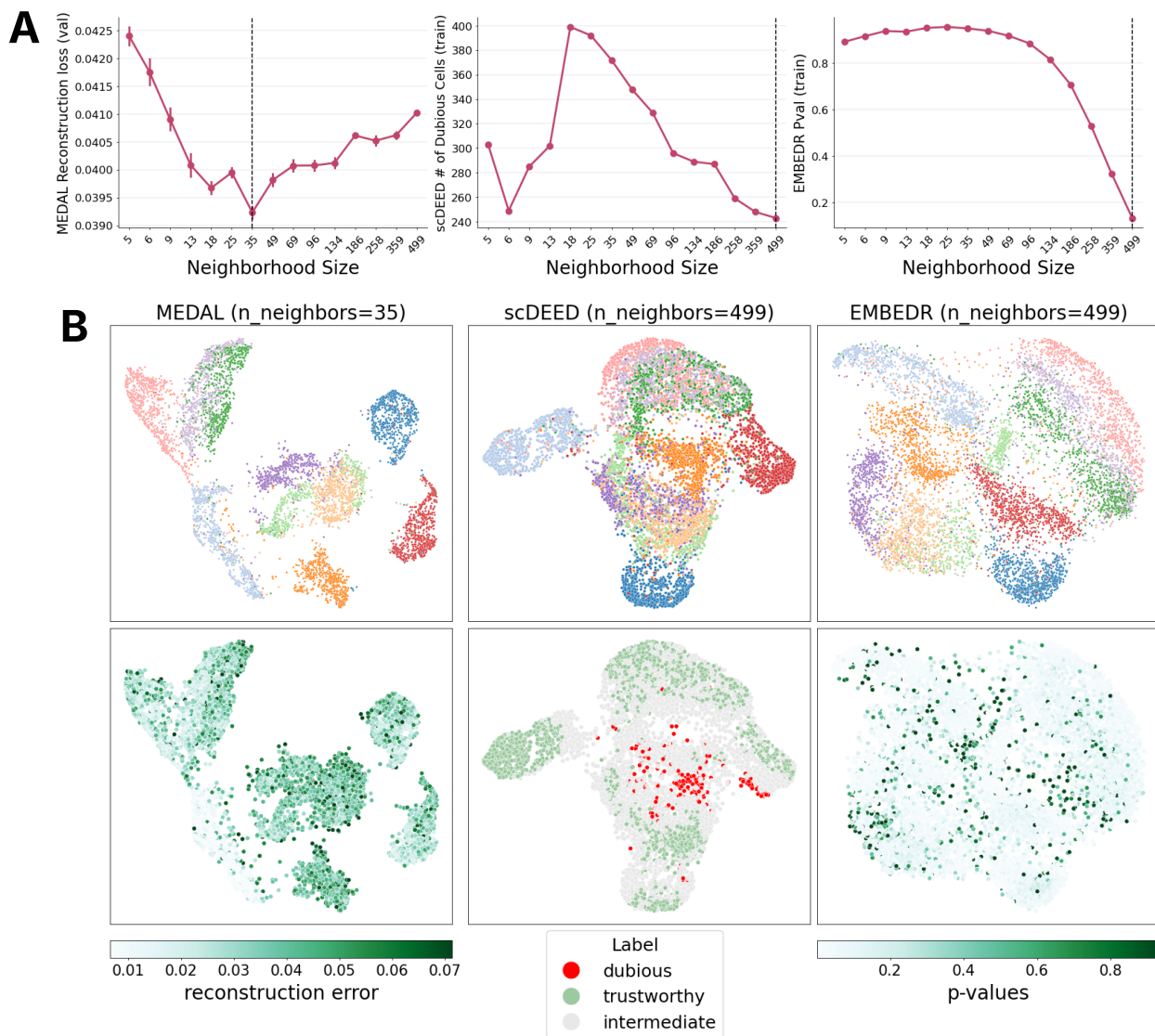


Figure S17: **Comparison of MEDAL with existing diagnostics on MNIST UMAP embeddings.** **A**, Hyperparameter-selection curves across UMAP neighborhood sizes for MEDAL, scDEED, and EMBEDR. neMDBD is omitted because the available package does not support UMAP. Dashed vertical lines indicate the selected neighborhood size. **B**, Embeddings selected by each method. Top row: embeddings colored by digit label. Bottom row: MEDAL reconstruction error, scDEED trustworthy/intermediate/dubious labels, and EMBEDR p-values. MEDAL selects an intermediate neighborhood size, whereas scDEED and EMBEDR select the largest neighborhood size in the grid. neMDBD is omitted because the available implementation supports t-SNE but not UMAP.

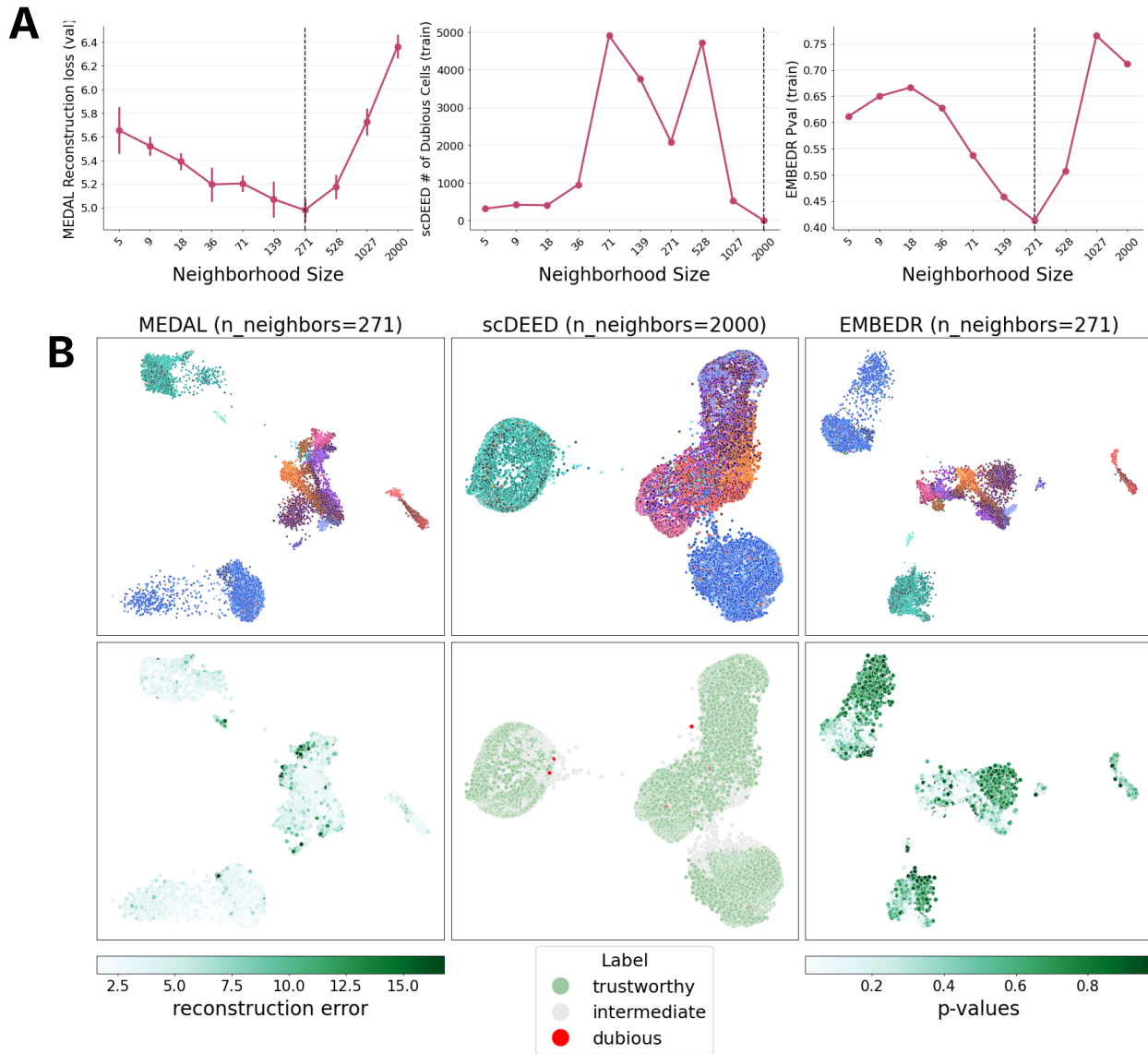


Figure S18: **Comparison of MEDAL with existing diagnostics on Hydra UMAP embeddings.** **A**, Hyperparameter-selection curves across UMAP neighborhood sizes for MEDAL, scDEED, and EMBEDR. neMDD is omitted because the available package does not support UMAP. Dashed vertical lines indicate the selected neighborhood size. **B**, Hydra embeddings selected by each method. Top row: embeddings colored by reported cell type. Bottom row: MEDAL reconstruction error, scDEED trustworthy/intermediate/dubious labels, and EMBEDR p-values. MEDAL and EMBEDR select $n = 271$, whereas scDEED selects the largest neighborhood size in the grid. Even when methods select the same nominal hyperparameter, embeddings and diagnostic signals may differ because each method uses its own implementation and optimization workflow. neMDD is omitted because the available implementation supports t-SNE but not UMAP.

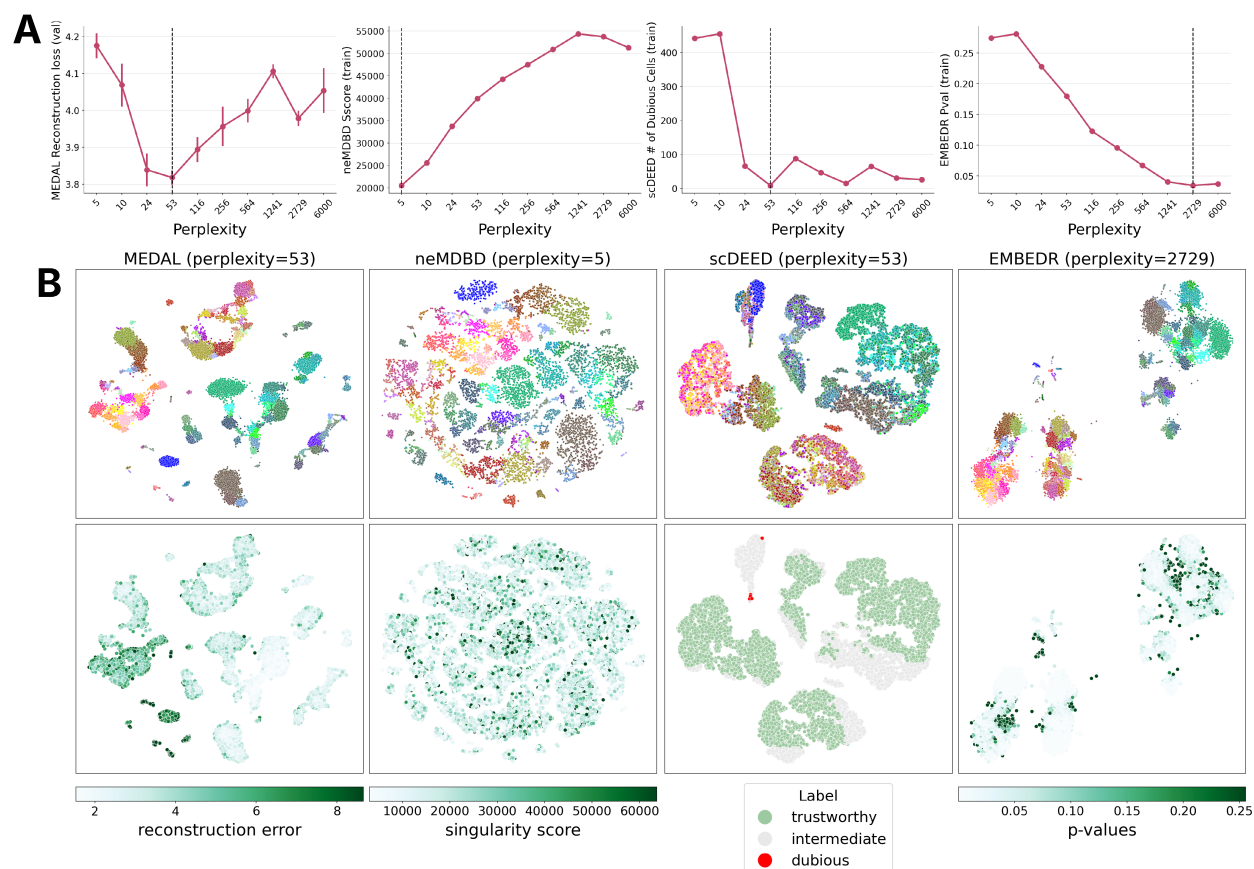


Figure S19: **Comparison of MEDAL with existing diagnostics on Neocortex t-SNE embeddings.** **A**, Hyperparameter-selection curves across t-SNE perplexities for MEDAL, neMDBD, scDEED, and EMBEDR. Dashed vertical lines indicate the selected perplexity under each method's criterion. **B**, Neocortex embeddings selected by each method. Top row: embeddings colored by annotated transcriptomic cell type. Bottom row: MEDAL reconstruction error, neMDBD singularity score, scDEED trustworthy/intermediate/dubious labels, and EMBEDR p-values. MEDAL and scDEED select an intermediate perplexity, whereas neMDBD selects the smallest perplexity and EMBEDR selects a large perplexity.

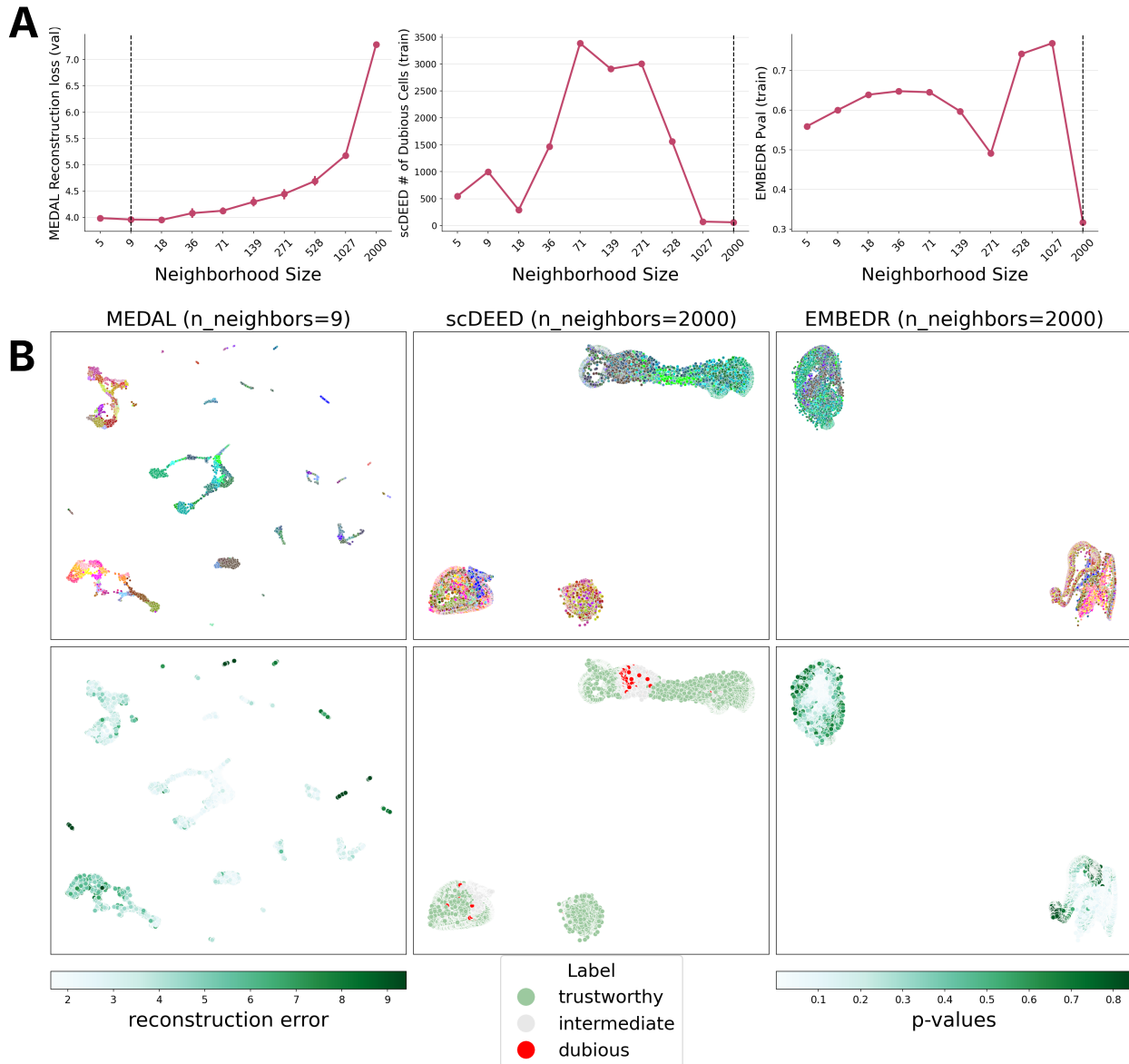


Figure S20: **Comparison of MEDAL with existing diagnostics on Neocortex UMAP embeddings.** **A**, Hyperparameter-selection curves across UMAP neighborhood sizes for MEDAL, scDEED, and EMBEDR. neMDBD is omitted because the available package does not support UMAP. Dashed vertical lines indicate the selected neighborhood size. **B**, Neocortex embeddings selected by each method. Top row: embeddings colored by annotated transcriptomic cell type. Bottom row: MEDAL reconstruction error, scDEED trustworthy/intermediate/dubious labels, and EMBEDR p-values. MEDAL selects a small neighborhood size, whereas scDEED and EMBEDR select the largest neighborhood size in the grid. neMDBD is omitted because the available implementation supports t-SNE but not UMAP.

Global and local metrics We also evaluated the embeddings selected by each method using two external structure-preservation metrics. For global structure preservation, we used random triplet accuracy, defined as the proportion of randomly sampled triplets whose relative pairwise-distance ordering is preserved between the original and embedded spaces [2]. For local structure preservation, we used the Local Continuity Meta-Criterion (LCMC), which measures overlap between nearest-neighbor sets in the original and embedded spaces [2]. These metrics are used only as complementary summaries since no single unsupervised metric fully characterizes embedding quality, and local and global criteria often favor different hyperparameter regimes.

[Supplementary Table S2](#) reports triplet accuracy and LCMC across all datasets, teacher methods, and diagnostics at each method’s selected hyperparameter. MEDAL is competitive across settings and often achieves the strongest local-structure preservation, particularly for UMAP comparisons, whereas other methods sometimes achieve higher triplet accuracy by selecting larger or edge-of-grid hyperparameters. scDEED results are marked separately because scDEED is evaluated relative to its post-PCA-preprocessed embedding rather than the embedding reduced from the original feature space.

LCMC k -range choices LCMC was computed over a dataset-specific range of neighborhood sizes: Neocortex $k \in [10, 300]$ with step size 20, Hydra $k \in [10, 200]$ with step size 20, MNIST $k \in [5, 50]$ with step size 5, and APOGEE $k \in [5, 20]$ with step size 1. These ranges were chosen to reflect differences in dataset size and annotation granularity. For the larger single-cell datasets, we evaluated LCMC over broader neighborhoods so that the metric captured local cell-state or cell-type structure without being dominated by only the nearest few neighbors. For the smaller or more discretely clustered datasets, we used smaller neighborhood ranges to focus the metric on local neighborhood preservation. Because the choice of k -range affects the numerical value of LCMC, these values should be interpreted primarily as within-dataset comparisons across methods, rather than as absolute measures that are comparable across datasets.

Runtime and scalability We measured wall-clock runtime for a full hyperparameter sweep for each method on each dataset and teacher setting where the method was available ([Supplementary Figure S21](#)). These runtimes reflect one complete workflow per seed, including embedding computation and diagnostic scoring. For MEDAL, this corresponds to one sweep of student distillations across the candidate teacher hyperparameters; repeated MEDAL runs can then be used to estimate averaged validation curves. EMBEDR and scDEED include their permutation- or null-based diagnostic calculations. neMDBD runtimes report the singularity score only, because the permutation score was computationally prohibitive at the dataset scales considered here.

Stability and implementation caveats Because scDEED relies on null embeddings, its selected hyperparameter can vary with random seed even when the embedding being scored is held fixed. In [Supplementary Figure S22](#), we show scDEED results across three random seeds, illustrating variation in both selected hyperparameter and downstream embedding quality metrics. This motivates our use of repeated MEDAL distillations and averaged validation curves for stable selection.

A limitation of this comparison is that the three systems use different t-SNE implementations internally — EMBEDR uses a Python/Cython Barnes-Hut implementation, neMDBD uses Rtsne (C++), and MEDAL uses openTSNE — which produce numerically distinct embeddings even

Dataset	Method	t-SNE			UMAP		
		perplexity	Triplet acc.	LCMC	n	Triplet acc.	LCMC
Neocortex	neMDBD	5	0.5872	0.454	—	—	—
	EMBEDR	2729	0.7964	0.486	2000	0.7214	0.056
	scDEED [†]	2729	0.7256	0.193	2000	0.7596	0.0802
	MEDAL	53	0.683	0.528	9	0.7106	0.4677
Hydra	neMDBD	5	0.6362	0.386	—	—	—
	EMBEDR	4999	0.7446	0.314	271	0.6236	0.244
	scDEED [†]	4999	0.6646	0.1646	2000	0.621	0.0741
	MEDAL	499	0.6628	0.4229	271	0.614	0.241
MNIST	neMDBD	5	0.6112	0.418	—	—	—
	EMBEDR	5	0.6544	0.425	499	0.6302	0.253
	scDEED [†]	341	0.6574	0.249	499	0.6362	0.2145
	MEDAL	793	0.6804	0.383	35	0.6396	0.342
APOGEE	neMDBD	3	0.6480	0.391	—	—	—
	EMBEDR	499	0.7418	0.264	499	0.5006	0.096
	scDEED [†]	499	0.6688	0.2145	134	0.5036	0.0961
	MEDAL	6	0.6426	0.348	9	0.5994	0.3375

Table S2: Triplet accuracy and LCMC at each method’s selected hyperparameter, evaluated on embeddings refit on pooled train and validation data. For t-SNE the selected hyperparameter is perplexity; for UMAP it is the number of nearest neighbors n . MEDAL results are mean \pm SE across 3 seeds. **Bold** indicates the best reported value within each dataset and teacher family. LCMC is averaged over neighborhood sizes sampled at equal intervals within the following ranges: Neocortex [10, 300] (step 20), Hydra [10, 200] (step 20), MNIST [5, 50] (step 5), APOGEE [5, 20] (step 1). Because this is a whole-system comparison, identical nominal hyperparameters do not imply identical embeddings; for example, MEDAL and EMBEDR both select $n = 271$ on Hydra UMAP but use different embedding implementations and therefore produce different metric values. [†]scDEED metrics are computed relative to a PCA-reduced input space rather than the original feature space and are therefore not directly comparable to the other methods; see [Stability and implementation caveats](#).

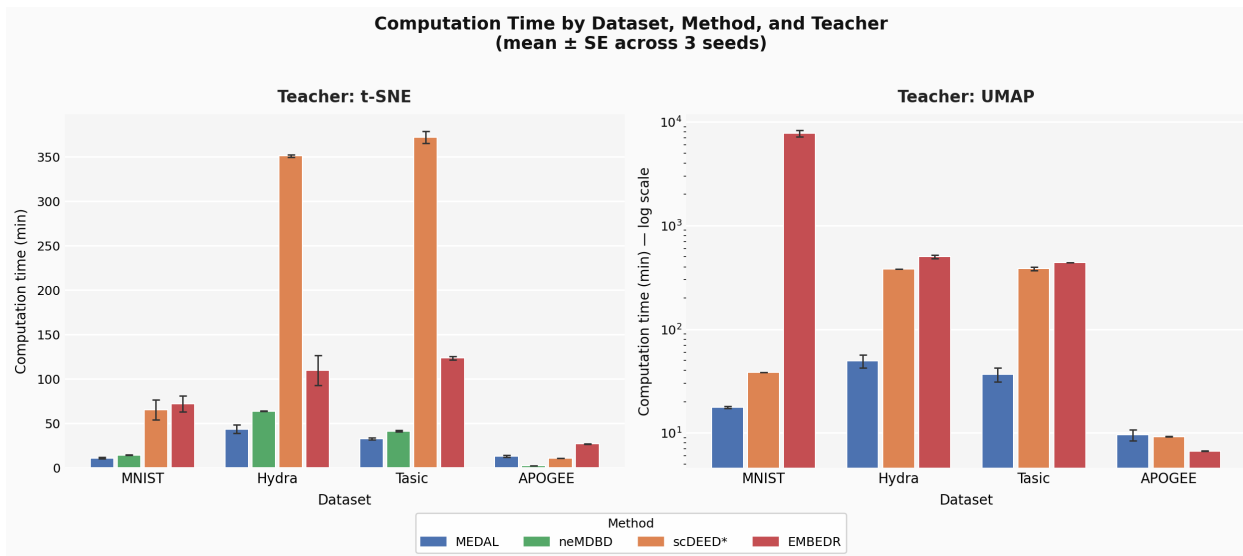


Figure S21: **Runtime comparison across embedding diagnostics.** Wall-clock runtime for one full hyperparameter sweep across datasets and teacher methods. Times reflect each method’s complete deployed workflow for a single seed, including its own embedding implementation and diagnostic computation. For MEDAL, this corresponds to one sweep of student distillations across the candidate teacher hyperparameters; repeated sweeps are used to average validation curves. scDEED and EMBEDR runtimes include their null- or permutation-based calculations. neMDBD runtimes report only the singularity score, because the permutation score was computationally prohibitive at these dataset scales.

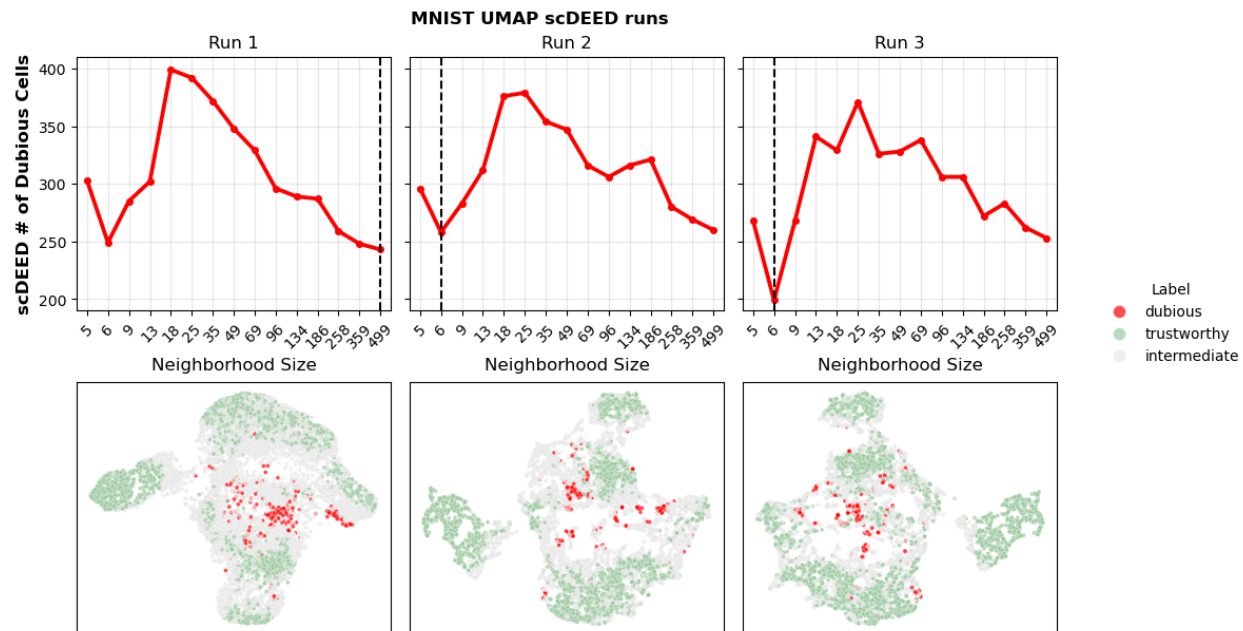


Figure S22: **Sensitivity of scDEED hyperparameter selection to random seed.** scDEED was run across three random seeds while holding the reference embeddings for each hyperparameter value fixed. The selected hyperparameter and resulting embedding-quality metrics vary across seeds, illustrating the stochasticity introduced by null-embedding construction.

at identical perplexity values. This arises from differences in kNN graph construction, affinity matrix bandwidth search tolerances, and gradient computation backends, all of which are internal to each implementation and not externally controllable without altering the methods themselves. As a result, observed metric differences reflect the performance of each method as a whole system, encompassing both hyperparameter selection and embedding computation, rather than isolating the contribution of hyperparameter selection alone. A fully controlled comparison would require fixing a canonical embedding implementation across all methods; however, this would require each method to re-select its hyperparameter on embeddings it was not designed to score, introducing a different form of bias. We therefore adopt the whole-system evaluation as the most faithful representation of how each method would be used in practice. For UMAP, all three methods use their own internal UMAP implementations, and the same argument applies.

Finally, neMDBD proposes both a singularity score and a permutation score for evaluating embeddings. We report only the singularity score in our comparison due to the prohibitive computational cost of the permutation score at the dataset scales considered here.

S4 Related Work

Nonparametric and parametric dimension reduction. A broad range of methods has been developed for dimension reduction. Linear methods such as PCA provide an explicit parametric map and an exact notion of reconstruction error, making them interpretable and easy to evaluate. Nonlinear methods such as Isomap [92], LLE [85], t-SNE [98], UMAP [72], PaCMAP [102], and PHATE [76] are designed to capture curved or neighborhood-based structure that linear projections miss. These methods have become central tools for exploratory analysis, especially in scientific applications where low-dimensional visualizations are used to discover clusters, trajectories, and other latent structure.

Despite their empirical success, many popular manifold-learning methods produce embeddings only for the observed training data rather than a reusable map from input space to embedding space. Existing out-of-sample and parametric extensions [9, 86, 97] partially address this limitation by learning an explicit forward map. However, these approaches are typically method-specific and usually optimize the original neighbor-preserving objective rather than faithfully reproducing a fixed, precomputed embedding. Moreover, most parametric neighbor-embedding methods provide an encoder but no decoder, making it difficult to evaluate how much high-dimensional information is retained by the learned low-dimensional representation.

Autoencoders and geometry-regularized representation learning. Autoencoder based methods provide a complementary approach to representation learning by optimizing a reconstruction objective through a low-dimensional bottleneck [96]. Unlike most nonparametric manifold learners, autoencoders naturally provide both a forward map into the latent space and a decoder back to the original feature space. This makes reconstruction loss a natural measure of compression fidelity for the autoencoder’s own latent representation. However, vanilla autoencoders do not generally enforce agreement with a specific manifold-learning embedding, and their latent spaces may not reproduce the neighborhood structure or visual geometry selected by methods such as t-SNE or UMAP. As a result, their reconstruction error cannot be interpreted as the information loss induced by a particular fitted manifold embedding.

Several methods therefore combine autoencoding with geometric regularization, for example by

encouraging the latent representation to preserve distances, neighborhoods, graphs, or other geometric relationships computed from the input data. Closest in spirit are Geometry Regularized Autoencoders (GRAE) [32], which augment the autoencoder objective with a geometric regularization term so that the latent representation follows a manifold-learning geometry while retaining out-of-sample extension and reconstruction. MEDAL differs in both objective and use case. Rather than proposing a new dimension-reduction method, MEDAL treats a fitted teacher embedding as the object of evaluation, explicitly enforces near-exact recovery of that teacher embedding, and then interprets reconstruction error conditional on successful distillation.

Automated hyperparameter selection. A related line of work aims to make dimension-reduction workflows less dependent on manual visual tuning. For t-SNE, Cao and Wang [17] propose model-selection objectives based on information criteria such as BIC or MDL to choose perplexity values automatically. Other work uses constraint-preserving scores, Bayesian optimization, or multi-objective surrogate models to tune hyperparameters for methods such as t-SNE, UMAP, and LargeVis [62, 101]. HyperNP further accelerates interactive exploration by training a neural network to approximate projections across hyperparameter values, enabling approximate t-SNE, UMAP, or Isomap embeddings to be generated in real time [3].

Domain-specific studies have also proposed automated tuning strategies. For example, Lin and Fukuyama [63] select t-SNE and UMAP hyperparameters by modeling data as signal plus noise and maximizing neighborhood-preservation with respect to an estimated signal. Other approaches optimize UMAP or manifold-learning hyperparameters using downstream objectives such as clustering quality, classification accuracy, or task-level performance [37, 52, 78]. Together, these methods mark an important shift from ad hoc visual inspection toward systematic hyperparameter search. However, their conclusions still depend on the chosen quality metric, task objective, or algorithm-specific criterion. They therefore do not by themselves define a method-agnostic measure of embedding information loss, nor do they provide a common scale for comparing different manifold learners.

Embedding quality metrics and local reliability diagnostics. Another line of work evaluates the quality or reliability of a completed embedding. Classical criteria such as trustworthiness, continuity, co-ranking summaries, stress, and neighborhood-overlap scores quantify how well local or global relationships in the high-dimensional data are preserved after projection. These metrics are useful for diagnosing rank or neighborhood distortions, but they typically operate directly on the completed embedding and do not provide a learned inverse map, held-out reconstruction protocol, or pointwise estimate of information loss in the original data space.

More recent diagnostic methods focus on local reliability and pointwise distortion. EMBEDR evaluates embedding reliability by comparing local structure in the observed embedding against a null or resampling-based reference [51]. scDEED computes pointwise reliability scores using permutations of nearest-neighbor distances and labels low-confidence points as “dubious” [103]. Related continuity- or singularity-based approaches diagnose where neighbor embeddings may behave unstably under local perturbations [64]. These methods provide valuable warnings about specific regions of an embedding, and some can be used to guide hyperparameter selection. However, their outputs are often expressed as p-values, reliability labels, singularity scores, or neighborhood-based diagnostics. Such quantities are informative, but they are not always directly comparable across datasets, methods, and hyperparameter settings, and they do not quantify reconstruction loss in the original feature space.

Positioning of MEDAL. MEDAL addresses a different problem from these prior lines of work. Rather than proposing another manifold learner, another parametric approximation to a neighbor-embedding objective, or another diagnostic computed directly on a finished visualization, MEDAL converts any fitted teacher embedding into a reusable encoder–decoder model. The encoder is trained to recover the fixed teacher coordinates, while the decoder maps those coordinates back to the original feature space. Conditional on near-zero teacher recovery, the remaining reconstruction error measures how much input-space information is lost when data are compressed through that teacher manifold.

This distinction gives MEDAL three practical advantages. First, because the teacher embedding is fixed, MEDAL evaluates the information content of the embedding actually used by the analyst rather than a newly optimized parametric variant. Second, because MEDAL learns a decoder, it provides a direct reconstruction-based measure of compression fidelity. Third, because the same student class and reconstruction criterion can be applied to embeddings produced by t-SNE, UMAP, Isomap, PCA, or other methods, MEDAL enables hyperparameter settings and dimension-reduction algorithms to be compared on a common, dataset-specific scale. In this way, MEDAL provides a bridge between classical nonparametric manifold learning and modern parametric representation learning, enabling quantitative validation, comparison, and selection of dimension-reduction methods in scientific applications.